

# **Assessment of the Biodistribution of Aluminum-Based Vaccine Adjuvants using $^{111/115}\text{In-AlO(OH)}$**

by

Tullio Vito Francesco Esposito  
B.Sc (Pharmacy), The University of British Columbia, 2013

A THESIS SUBMITTED IN PARTIAL FULFILLMENT OF  
THE REQUIREMENTS FOR THE DEGREE OF  
MASTER OF SCIENCE

In

The Faculty of Graduate and Postdoctoral Studies  
(Pharmaceutical Sciences)

THE UNIVERSITY OF BRITISH COLUMBIA  
(Vancouver)

August 2016

©Tullio Vito Francesco Esposito, 2016

## Abstract

Aluminum-based adjuvants are found in a wide range of non-living vaccines to enhance antibody-mediated immune responses. Alhydrogel is one of the most common aluminum-based adjuvants and consists of 1-12  $\mu\text{m}$  clusters of loosely aggregated aluminum oxyhydroxide (AlO(OH)) nanoparticles. Despite widespread use since the 1930s, the biodistribution of this adjuvant is poorly understood. The current assumption within the field is that AlO(OH) particles remain at the site of injection and slowly dissolve over time. However, rare neurological and muscle adverse effects, such as macrophagic myofasciitis, are thought to be due to the bio-persistence of the adjuvant at the site of injection and the distribution of AlO(OH) nanoparticles throughout the body. The objective of this thesis was to examine if component nanoparticles of Alhydrogel distribute following administration.

In order to test this hypothesis, traceable forms of AlO(OH) were synthesized by doping the adjuvant's crystal structure with different indium isotopes. Various physical, morphological and functional assessments showed that the doped adjuvant closely matched commercial Alhydrogel. Using a radioactive version of the tracer,  $^{111}\text{In}$ -AlO(OH), the biodistribution of the adjuvant was assessed using serial SPECT/CT imaging. Approximately 20% of the tracer was released from the site of injection over 15 days and could be found in organs like the draining lymph nodes and liver. A novel application of mass cytometry was used to examine the kinetics and cellular distribution of  $^{115}\text{In}$ -AlO(OH) particles within the draining lymph nodes; the adjuvant appeared at this site within 1 day and reached peak levels 15 days post-injection. The adjuvant was sequestered into antigen presenting cells and induced the up-regulation of maturation markers in adjuvant-positive dendritic cells within the draining lymph node. Finally, electron microscopy coupled with atomic mapping confirmed the presence of Alhydrogel component nanoparticles in the draining lymph node and liver.

This thesis presents the most detailed assessment to date of the biodistribution of aluminum-based adjuvants. Understanding Alhydrogel's biodistribution can help shed light on the adjuvant's immunostimulatory mechanisms and adverse events. Lessons learnt from one of the world's oldest adjuvants can be applied to the design of the next generation of immunopotentiators.

## Preface

### Chapter 2:

This material is from a manuscript in preparation. Rahel Schneider (UBC/ University of Basel) helped under my guidance to develop the methods to synthesize the doped adjuvant (Sections 2.2.1 and 2.2.2). Staff at the UBC Structural Chemistry Facility carried out the PXRD analysis (Figures 2-4 and 2-6). Xin Zhang at SFU 4D Labs provided assistance with STEM imaging and elemental mapping (Figures 2-10 to 2-12). Patrick Hopkins (UBC) provided assistance and guidance for the functional immune assays (Figures 2-15 to 2-16). All other experiments and the data analysis were performed by myself. I conceived the doping strategy for Alhydrogel and Urs Hafeli and myself developed the experimental plan. None of this text is taken from previously published articles.

### Chapter 3:

This material is from a manuscript in preparation. Cristina Rodriguez developed the reconstruction parameters for the dual-isotope  $^{67}\text{Ga}/^{111}\text{In}$  SPECT at the UBC *in vivo* Imaging Centre (Figure 3-2). Katayoun Saatchi (UBC) assisted with the animal dissection for the biodistribution study (Figure 3-8). All other experiments and the data analysis were performed by myself. Urs Hafeli and I conceived the experiments. None of this text is taken from previously published articles.

### Chapter 4:

This material is from a manuscript in preparation. Patrick Hopkins and Jacqueline Lai (UBC/ University of Gothenburg) helped with sample staining (Section 4.2.2.) and aspects of the data analysis (Figures 4-5 to 4-7). Andy Johnson from the UBC Flow Cytometry Centre provided technical assistance and instruction in the operation of the CyTOF instrument (Section 4.4.4). All other experiments and the data analysis were performed by myself. I devised the concept of using mass cytometry for *in vivo* nanoparticle tracking. Urs Hafeli, Jan Dutz, Jacqueline Lai, Patrick Hopkins and myself developed the experimental plan. None of this text is taken from previously published articles.

### Chapter 5:

This material is from a manuscript in preparation. Derrick Horne at the UBC Bioimaging Facility processed the fixed tissue samples for electron microscopy (Section 5.2.2). Matthew Bilton at SFU 4D Labs assisted with STEM imaging and elemental mapping (Section 5.2.3.). All other experiments and the data analysis were performed by myself. Urs Hafeli and I developed the experimental plan. None of this text is taken from previously published articles.

### Appendix:

Staff at the UBC Structural Chemistry Facility carried out the PXRD analysis (Figure A-1). Andrew Yung and Barry Bohnet at the UBC MRI Research Centre carrying out the phantom scans (Figures A-2 and A-3). All other experimental work was carried out by myself. Urs Hafeli and I developed the experimental plan. None of this text is taken from previously published articles.

# Table of Contents

Abstract .....	ii
Preface .....	iii
Table of Contents .....	iv
List of Tables.....	vii
List of Figures.....	viii
List of Abbreviations .....	x
Acknowledgements .....	xiii
Chapter 1: Introduction.....	1
1.1. History and Clinical Use of Aluminum-Based Adjuvants.....	1
1.2. Structure and Adsorptive Mechanisms of Aluminum-Based Adjuvants:.....	1
1.3. Immunostimulatory Mechanisms of Aluminum-Based Adjuvants: .....	2
1.4. Safety of Aluminum-Based Adjuvants.....	4
1.5. Current State of Knowledge for the Biodistribution of Aluminum-Based Adjuvants.....	5
1.6. Hypothesis and Research Objectives.....	6
Chapter 2: Preparation and Characterization of Indium-Doped AlO(OH).....	7
2.1. Introduction .....	7
2.2. Materials and Methods .....	8
2.2.1. Synthesis of AlO(OH) .....	8
2.2.2. Synthesis of <sup>115</sup> In-Doped AlO(OH) .....	9
2.2.3. Synthesis of <sup>111</sup> In-Doped AlO(OH) .....	9
2.2.4. Encapsulation Efficiency of <sup>111</sup> In within the AlO(OH) Matrix .....	9
2.2.5. Concentration and Specific Activity.....	9
2.2.6. Powder X-Ray Diffraction (PXRD) .....	9
2.2.7. Dynamic Scanning Calorimetry (DSC).....	10
2.2.8. Fourier Transform Infrared Spectroscopy (FTIR) .....	10
2.2.9. Dynamic Light Scattering (DLS) .....	10
2.2.10. Scanning Transmission Electron Microscopy (STEM).....	10
2.2.11. Stability of <sup>111</sup> In-AlO(OH) in Different Media over Time .....	10
2.2.12. Protein Adsorptivity .....	11
2.2.13. Protein De-Adsorption in Biological Fluids .....	11
2.2.14. Cellular Toxicity Assays .....	11
2.2.15. Humoral Immune Response Assessment.....	12
2.2.16. Cellular Immune Response Assessment.....	13
2.2.17. Data Analysis.....	13

2.2.18.	Ethics Statement .....	13
2.3.	Results .....	14
2.3.1.	Encapsulation Efficiency, Concentration and Specific Activity of $^{111/115}\text{In-AIO(OH)}$ .....	14
2.3.2.	Stability of $^{111}\text{In-AIO(OH)}$ in Different Media.....	14
2.3.3.	Physical Characterization of Alhydrogel.....	15
2.3.4.	Physical Characterization of $^{111/115}\text{In-AIO(OH)}$ .....	16
2.3.5.	Hydrodynamic Size and Zeta Potential of $^{111/115}\text{In-AIO(OH)}$ and Alhydrogel.....	17
2.3.6.	Particle Morphology and Spatial Location of $^{115}\text{In}$ Dopant within AIO(OH) Nanoparticles .....	18
2.3.7.	Protein Adsorptivity and De-Adsorptivity Assays to $^{111/115}\text{In-AIO(OH)}$ and Alhydrogel.....	21
2.3.8.	Cellular Toxicity of $^{111/115}\text{In-AIO(OH)}$ and Alhydrogel.....	22
2.3.9.	Humoral and Cellular Immune Responses to $^{111/115}\text{In-AIO(OH)}$ and Alhydrogel .....	23
2.4.	Discussion.....	25
Chapter 3:	Biodistribution of $^{111}\text{In-AIO(OH)}$ .....	27
1.1.	Introduction .....	27
3.2.	Materials and Methods .....	28
3.2.1.	Synthesis and Radiolabeling of $^{67}\text{Ga-NOTA-OVA}$ .....	28
3.2.2.	Labeling Efficiency and Radiopurity Assessment of $^{67}\text{Ga-NOTA-OVA}$ .....	28
3.2.3.	SDS and Native PAGE Analysis of $^{67}\text{Ga-NOTA-OVA}$ .....	28
3.2.4.	SPECT/CT Assessment of $^{67}\text{Ga-NOTA-OVA}$ Adsorbed to $^{111}\text{In-AIO(OH)}$ or Alhydrogel .....	29
3.2.5.	Sacrifice-Based Biodistribution of $^{111}\text{In-AIO(OH)}$ .....	30
3.2.6.	Data Analysis.....	30
3.2.7.	Ethics Statement .....	30
3.3.	Results .....	31
3.3.1.	Preparation and Characterisation of $^{67}\text{Ga-NOTA-OVA}$ .....	31
3.3.2.	Serial SPECT/CT Assessment of $^{111}\text{In-AIO(OH)}$ and $^{67}\text{Ga-NOTA-OVA}$ at the Injection Site ....	32
3.3.3.	Sacrificed-Based Biodistribution of $^{111}\text{In-AIO(OH)}$ .....	34
3.4.	Discussion.....	35
Chapter 4:	Distribution of $^{115}\text{In-AIO(OH)}$ Particles in the Lymph Node .....	37
4.1.	Introduction .....	37
4.2.	Materials and Methods .....	38
4.2.1.	Animal Immunizations and Tissue Preparation.....	38
4.2.2.	CyTOF Staining and Analysis .....	38
4.2.3.	Establishing a Gating Strategy for 2.5% $^{115}\text{In-AIO(OH)}$ .....	39
4.2.4.	Statistical Analysis .....	39
4.2.5.	Ethics Statement .....	39
4.3.	Results .....	40

4.3.1.	Gating Strategy for 2.5% <sup>115</sup> In-AIO(OH) Particles.....	40
4.3.2.	Cells Treated with Free <sup>115</sup> In or 2.5% <sup>115</sup> In-AIO(OH) can be Distinguished.....	40
4.3.3.	Levels of <sup>115</sup> In within the Inguinal Lymph Node of Naïve Mice.....	41
4.3.4.	Kinetics of <sup>115</sup> In-AIO(OH) within the Draining Lymph Node .....	41
4.3.5.	Cellular Distribution of <sup>115</sup> In-AIO(OH) within the Draining Lymph Node.....	42
4.4	Discussion.....	46
Chapter 5: STEM-Based Assessment of Alhydrogel’s Biodistribution .....		48
5.1.	Introduction .....	48
5.2.	Materials and Methods .....	49
5.2.1.	Animal Immunizations and Tissue Fixation.....	49
5.2.2.	Tissue Embedding and Preparation for STEM Imaging.....	49
5.2.3.	STEM Imaging and Data Analysis.....	49
5.2.4.	Ethics Statement .....	49
5.3.	Results .....	50
5.3.1.	Persistence, Morphology and Cellular Infiltration of Alhydrogel and 2.5% <sup>115</sup> In-AIO(OH) at the Site of Injection .....	50
5.3.2.	Alhydrogel Particles within the Draining Lymph Node 70 Days Post-Injection .....	52
5.3.3.	Alhydrogel Particles within the Liver After 70 Days Post-Injection.....	52
5.4.	Discussion.....	54
Chapter 6: Conclusion and Future Work.....		55
6.1.	Conclusion.....	55
6.2.	Future Work.....	56
References .....		58
Appendix 1: Development of a MR-Traceable Form of AIO(OH) .....		68

## List of Tables

### **Chapter 2:**

Table 2-1: Secondary antibodies used to detect anti-OVA antibodies.....	13
Table 2-2: Panel for OVA-tetramer staining.....	13

### **Chapter 3:**

Table 3-1: SPECT scan times and durations.....	29
--	----

### **Chapter 4:**

Table 4-1: Panel for CyTOF staining.....	38
Table 4-2: Definition of cell populations for the CyTOF analysis.....	42

### **Appendix:**

Table A-1: Relaxivity values for Gd-AlO(OH) in a 7T MRI.....	58
--	----

## List of Figures

### Chapter 1:

Figure 1-1: Adsorptive mechanisms of Alhydrogel.....	2
--	---

### Chapter 2:

Figure 2-1: Overview of the doping strategy for Alhydrogel using indium.....	8
Figure 2-2: Encapsulation efficiency of $^{111}\text{In-AIO(OH)}$ .....	14
Figure 2-3: Stability of $^{111}\text{In-AIO(OH)}$ over time in different diluents.....	15
Figure 2-4: PXRD analysis of Alhydrogel.....	15
Figure 2-5: DSC and FTIR analysis of Alhydrogel.....	16
Figure 2-6: PXRD analysis of 2.5-10% $^{115}\text{In-AIO(OH)}$ .....	16
Figure 2-7: DSC and FTIR analysis of 2.5% $^{115}\text{In-AIO(OH)}$ .....	17
Figure 2-8: Hydrodynamic size and zeta potential of $^{111/115}\text{In-AIO(OH)}$ versus Alhydrogel.....	17
Figure 2-9: Alhydrogel and 2.5% $^{115}\text{In-AIO(OH)}$ before and after sonication for STEM imaging.....	18
Figure 2-10: STEM images of Alhydrogel and 2.5% $^{115}\text{In-AIO(OH)}$ .....	19
Figure 2-11: Elemental mapping of Alhydrogel.....	20
Figure 2-12: Elemental mapping of 2.5% $^{115}\text{In-AIO(OH)}$ .....	21
Figure 2-13: Protein adsorptivity and de-adsorptivity to Alhydrogel and $^{111/115}\text{In-AIO(OH)}$ .....	21
Figure 2-14: YOYO-1 and MTT cell toxicity assays of Alhydrogel versus 2.5% $^{115}\text{In-AIO(OH)}$ .....	22
Figure 2-15: Humoral immune response to OVA adsorbed to Alhydrogel versus $^{111/115}\text{In-AIO(OH)}$ .....	23
Figure 2-16: Gating strategy for OVA-tetramer positive $\text{CD8}^+$ T-cells.....	24
Figure 2-17: Cell-mediated immune response to OVA adsorbed to Alhydrogel versus $^{111/115}\text{In-AIO(OH)}$ .....	24

### Chapter 3:

Figure 3-1: Gamma spectra of $^{67}\text{Ga}$ , $^{111}\text{In}$ and mixed isotopes.....	27
Figure 3-2: Reconstruction and triple energy windows for $^{67}\text{Ga}/^{111}\text{In}$ dual-isotope SPECT scans.....	29
Figure 3-3: Labeling efficiency and radiopurity of $^{67}\text{Ga-NOTA-OVA}$ .....	31
Figure 3-4: SDS and native PAGE analysis of $^{67}\text{Ga-NOTA-OVA}$ .....	31
Figure 3-5: Separation of $^{111}\text{In-AIO(OH)}$ and $^{67}\text{Ga-NOTA-OVA}$ signals within a mouse.....	32

Figure 3-6: VOI placement and draining of <sup>67</sup>Ga-NOTA-OVA from the sites of injection over time.....33

Figure 3-7: VOI analysis of <sup>111</sup>In-AIO(OH) from the site of injection over time.....33

Figure 3-8: Sacrifice-based biodistribution results for <sup>111</sup>In-AIO(OH) .....34

**Chapter 4:**

Figure 4-1: Gating strategy for cell unassociated 2.5% <sup>115</sup>In-AIO(OH) nanoparticles.....40

Figure 4-2: Differentiation of cells stained with <sup>115</sup>In-AIO(OH) and <sup>115</sup>In-citrate.....41

Figure 4-3: Kinetics of total <sup>115</sup>In-positive events and cell unassociated <sup>115</sup>In-AIO(OH) nanoparticles within the draining lymph node.....42

Figure 4-4: Gating strategy to assess the phenotype of <sup>115</sup>In-positive cellular events in the draining lymph node.....43

Figure 4-5: Changes in the cell numbers with the draining lymph node over time in mice treated with <sup>111</sup>In-AIO(OH).....44

Figure 4-6: Changes in the proportion of the cell population that are <sup>115</sup>In-positive in the draining lymph node over time.....44

Figure 4-7: Expression of maturation markers in <sup>115</sup>In-positive dendritic cells in the lymph node over time .....45

**Chapter 5:**

Figure 5-1: Injection site nodule 70 days post-administration.....50

Figure 5-2: Morphology of Alhydrogel at the site of injection 70 days post-administration.....50

Figure 5-3: Morphology and elemental mapping of 2.5% <sup>115</sup>In-AIO(OH) at the site of injection 70days post-administration.....51

Figure 5-4: Cellular infiltrate within the Alhydrogel injection site at 70 days post-administration .....51

Figure 5-5: Alhydrogel particle within the draining lymph node 70 days post-administration.....52

Figure 5-6: Unequivocal proof of Alhydrogel nanoparticles within the liver 70 days post-administration.....53

**Appendix:**

Figure A-1: FTIR and PXRD of 0.5-10% Gd-AIO(OH) .....57

Figure A-2: Phantom scan of Alhydrogel, Gadovist and 0.5-2.5% Gd-AIO(OH) in a 7T MRI.....58

Figure A-3: Phantom scan of a 1/10 serial dilution of 1% Gd-AIO(OH) in a 7T MRI.....59

## List of Abbreviations

7AAD	7-amino-actinomycin
ACK	Ammonium-Chloride-Potassium
AF555	AlexaFluor-555
ANOVA	Analysis of Variance
APC	Antigen Presenter Cell
APS	Ammonium Persulfate
AS04	Adjuvant System 4 (GlaxoSmithKline)
ASIA	Autoimmune/Inflammatory Syndrome Induced by Adjuvants
AUC	Area Under the Curve
BSA	Bovine Serum Albumin
CCL	Chemokine (C-C motif) Ligand
CD	Cluster of Differentiation
cpm	Counts Per Minute
CT	X-Ray Computed Tomography
CTL	Cytotoxic T-Lymphocyte
CXCL	Chemokine (C-X-C motif) Ligand
CyTOF	Mass Cytometry by Time of Flight
CyFACS	CyTOF Staining Buffer
DAMPs	Damage Associated Molecular Patterns
DC	Dendritic Cell
DLS	Dynamic Light Scattering
DSC	Dynamic Scanning Calorimetry
DNA	Deoxyribose Nucleic Acid
DNase1	Deoxyribonuclease 1
DMEM	Dulbecco's Modified Eagle Medium
DMSO	Dimethyl Sulfoxide
ELISA	Enzyme-Linked Immunosorbent Assay
EDTA	Ethylenediaminetetraacetic Acid

EDX	Energy-Dispersive X-Ray Spectroscopy
FACS	Fluorescence-Activated Cell Sorting
FBS	Fetal Bovine Serum
Fc	Fragment Crystallizable
FDA	Food and Drug Administration
FTIR	Fourier Transform Infrared Spectroscopy
HAADF	High-Angle Annular Dark-Field
HBeAg	Hepatitis B e Antigen
HRP	Horseradish Peroxidase
ICP-MS	Inductively Couple Plasma Mass Spectrometry
ID	Injected Dose
IL	Interleukin
Ig	Immunoglobulin
ITLC	Instant thin layer chromatography
JCPDS	Joint Committee on Powder Diffraction Standards
kDa	Kilodalton
MHC	Major Histocompatibility Protein
MMF	Macrophagic Myofasciitis
MTT	3-(4,5-dimethylthiazol-2-yl)-2,5-diphenyltetrazolium
MR	Magnetic Resonance
MWCO	Molecular Weight Cut-Off
NK	Natural Killer Cell
NLRP3	Nucleotide-Binding Domain, Leucine-Rich-Containing Family, Pyrin Domain-Containing-3
NOTA	1,4,7-triazacyclononane-1,4,7-trisacetic acid
OVA	Ovalbumin
PAGE	Polyacrylamide Gel Electrophoresis
PBS	Phosphate Buffered Saline
PBS-T	Phosphate Buffered Saline with Tween-20
PE	Phycoerythrin
PET	Positron Emission Tomography
PI3	Phosphoinositide 3 Kinase
PXRD	Powder X-Ray Diffraction

SDS	Sodium Dodecyl Sulfate
SPECT	Single-Photon Emission Computed Tomography
STEM	Scanning Transmission Electron Microscopy
Syk	Spleen Tyrosine kinase
TEM	Transmission Electron Microscopy
TEMED	Tetramethylethylenediamine
TLC	Thin-Layer Chromatography
TLR	Toll-like Receptor
Th	CD4 <sup>+</sup> T-helper Cell
TMB	3,3',5,5'-Tetramethylbenzidine
VOI	Volume of Interest

## Acknowledgements

I would like to thank Dr. Urs O. Häfeli, my supervisor and scientific mentor. Dr. Häfeli is the one who sparked my interest in the fields of nanomedicine and drug delivery science. I would also like to thank Drs. Katayoun Saatchi and Cristina Rodriguez for teaching me how to work with radioisotopes and perform SPECT/CT studies, respectively. I'm grateful to Rahel Schneider for her assistance in the lab at the early stages of the project. I would like to thank Dr. Jan Dutz as well as past and previous members of his lab (Dr. Jacqueline Lai and Patrick Hopkins) for their assistance and guidance on the many immunological aspects of this project.

A special thanks are owed to my mother (Sheila Esposito), sister (Demitria Esposito) and uncle (Paul Esposito) for all their support during my studies. This thesis is dedicated to my father (Tullio F. Esposito), who passed away in November 2013.

# Chapter 1: Introduction

## 1.1. History and Clinical Use of Aluminum-Based Adjuvants

Adjuvants have been used in vaccines for almost a century. In 1925, Gaston Ramon administered diphtheria toxoid to horses in combination with a variety of substances, such as plant extracts, starch and fish oil (1-3). He observed that their addition increased the antibody response to the toxoid significantly (1-3). Ramon coined the term adjuvant from the latin *adjuvare*, 'to help' (1-3).

A year later, in 1926, Alexander T. Glennie and colleagues dissolved diphtheria toxoid in a solution of alum ( $KAl(SO_4)_2 \cdot 12H_2O$ ) that when neutralized entrapped the antigen within an aluminum-precipitate (3, 4). This precipitate resulted in a significantly enhanced immune response compared to the soluble toxoid in guinea pigs (3, 4). Minor variations however in the anions present at the time of precipitation, largely from the buffers and growth media used to prepare the antigen component, lead to significant heterogeneity amongst aluminum-precipitated vaccines (5, 6). This problem was solved by Maschmann *et al.* in 1931 by adsorbing antigens onto the surface of preformed, standardized aluminum precipitates (7). Such preparations are known as aluminum-adsorbed vaccines (7).

Preformed aluminum precipitates have become the most common type of adjuvant in non-living vaccines (3, 8, 9). They are found, for example, in inoculations against tetanus, diphtheria, hepatitis A and B, pertussis, anthrax and the human papilloma virus (3, 8, 9). Since the 1930s, it has been estimated that hundreds of millions of people have been administered nearly a billion doses of aluminum-adsorbed vaccines (8, 9). Preformed aluminum precipitates were the only adjuvants approved for clinical use by the American FDA until 2009 with the approval of AS04 (10, 11).

## 1.2. Structure and Adsorptive Mechanisms of Aluminum-Based Adjuvants:

Currently, there are four different types of preformed aluminum precipitates used in vaccines: amorphous aluminum hydroxyphosphate, amorphous aluminum hydroxysulfate, amorphous aluminum hydroxyphosphate sulfate and poorly crystalline aluminum oxyhydroxide (12). The focus of this thesis will be aluminum oxyhydroxide,  $AlO(OH)$ .

Alhydrogel, manufactured by Brenntag Biosector A/S, was designated in the late 1980s as the international standard of  $AlO(OH)$  for use in vaccines (13). Alhydrogel is a viscous white suspension of 1-12  $\mu m$  clusters of weakly aggregated  $AlO(OH)$  nanoparticles in water (12). The component nanoparticles have average dimensions of 4.5 x 2.2 x 10 nm and provide a surface area of approximately 500  $m^2/g$  for the adsorption of antigens (12, 14).

Antigens are adsorbed to AlO(OH) particles via hydrophobic interactions, hydrogen bonding, van der Waals forces, electrostatic attraction or ligand exchange; the latter two are the most predominant mechanisms (12). Negatively charged antigens are electrostatically attracted to AlO(OH) given that the adjuvant has an isoelectric point of 11.4 and is positively charged at physiological pH (Figure 1-1A) (12). Ligand exchange is a process by which the hydroxyls coordinated to aluminum atoms on the surface of AlO(OH) are substituted by phosphate groups on the antigen (Figure 1-1B) (12). Ligand exchange is the strongest of the adsorptive mechanisms, as it can even overcome electrostatic repulsion to adsorb positively charged antigens to Alhydrogel (12).

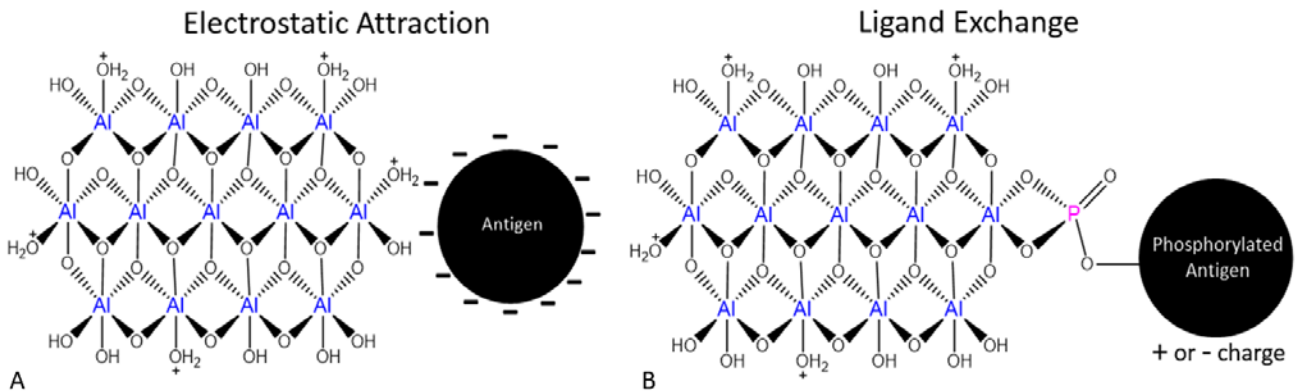


Figure 1- 1: Electrostatic (A) and ligand exchange (B) mechanisms by which Alhydrogel adsorbs antigens to its surface.

### 1.3. Immunostimulatory Mechanisms of Aluminum-Based Adjuvants:

Preformed aluminum precipitates promote antibody-mediated immunity against adsorbed antigens, but are poor at stimulating cell-mediated responses. The mechanisms by which this adjuvant class works are complex and the details have only recently begun to be elucidated. The following theories exist in the literature:

- *Recruitment of innate immune cells to the site of injection:* preformed aluminum precipitates induce the secretion of pro-inflammatory mediators, such as IL-1 $\beta$ , IL-5, CCL2, CCL4, CCL11, CCL24, CXCL1 and CXCL2 upon administration (15, 16). These factors recruit neutrophils, eosinophils, macrophages, inflammatory monocytes and dendritic cells to the site of injection (15, 16). The degree of inflammation is significantly higher when antigens are adsorbed to aluminum precipitates compared to the soluble state (15). The recruitment of the innate immune cells helps to support the sequence of events required to develop antigen-specific adaptive responses, like antibodies.
- *Increased antigen internalization and duration of presentation:* antigen presenter cells (APCs), such as dendritic cells, more efficiently internalize antigen in particulate form (17-19). Ghimire *et al.* found that antigen accumulation in cultured dendritic cells was 100-fold higher when bound to Alhydrogel compared to the soluble protein (17). The magnitude and duration of antigen presentation by dendritic cells *in vitro* was also enhanced when the antigen was adsorbed (17).

- Formation of an antigen depot at the site of injection:* the rate of antigen draining from the site of injection is slowed when adsorbed to aluminum precipitates to allow enough time for APCs to arrive, internalize and process the antigen. Glennly was the first to observe the formation of an antigen depot at the site of injection with aluminum-based adjuvants (20). Harrison *et al.* further demonstrated antigen persistence by using inflammatory nodules that form at the site of injection to immunize naïve animals (21-23). More recently, Noe *et al.* used a radiolabeled protein, <sup>111</sup>In- $\alpha$ -casein, to confirm that adsorbed antigens are retained at the injection site longer than free antigen (24). Excision of the injection site 4 days post-administration was found to interfere with the development of humoral immunity, demonstrating the importance of the antigen depot (6). However, a similarly designed study found that removal of the depot only 2 hours post-injection had no immunological consequences (25). There is still considerable controversy in the field whether or not an antigen depot at the site of injection is required to potentiate an immune response with this adjuvant class.
- Release of endogenous DAMPs:* aluminum-based adjuvants induce local necrosis at the site of injection, which leads to the release of endogenous damage associated molecular patterns (DAMPs) (15, 26, 27). These molecules, such as uric acid and genomic DNA, bind to pattern recognition receptors (PRRs) that activate APCs to potentiate adaptive immunity (15, 26, 27). Mice pre-treated at the site of injection with DNase1, an enzyme that degrades genomic DNA, had a reduced humoral response to an aluminum-adsorbed vaccine (26).
- Activation of the NLRP3 inflammasome:* following internalization by APCs, aluminum precipitates destabilize the phagolysosome leading to the assembly and activation of the NLRP3 inflammasome (28). Activation of this inflammasome results in caspase-1 processing IL-1 $\beta$  and IL-18 into their biologically mature forms (28). As mentioned above, IL-1 $\beta$  helps to recruit cells of the innate immune system to the site of injection (15, 16, 29). IL-1 $\beta$  and IL-18 together have been shown to polarize naïve CD4<sup>+</sup> T-helper cells toward a Th2 phenotype, which in turn promotes humoral immunity (IgG1 and IgE isotypes in mice) (28, 30). There is significant controversy surrounding this theory since NLRP3 knockout mice administered an aluminum-adsorbed vaccine have shown a marked suppression of antigen-specific IgE and IgG1 production (31, 32), suppression of IgE but not IgG1 (29) or no effect on antibody production at all (33, 34).
- Promotion of PI3-Syk kinase signalling:* the interaction of extracellular aluminum precipitates with lipid rafts in the cell membrane of APCs can activate the PI3 and Syk kinases (35, 36). Activation of the PI3 kinase inhibits the production of IL-12p70, a key cytokine in the polarization of naïve CD4<sup>+</sup> cells toward a cellular immunity promoting Th1 phenotype (35, 37). Downstream effects of Syk kinase activation include the release of prostaglandin E2 by APCs, a molecule that promotes Th2 polarization (36).

The above theories all assume that Alhydrogel nanoparticles remain and slowly dissolve from the site of injection. Prominent figures within the field have proposed that the distribution of AlO(OH) nanoparticles to distant sites may help to explain controversial aspects of the adjuvant's mechanism (38). For example, the movement of antigen-coated nanoparticles to the draining lymph nodes may explain why the injection site can be removed after 2 hours without immunological consequences (25, 38). The distribution of AlO(OH) nanoparticles is not inconceivable, given that fact that APCs are known to internalize Alhydrogel *in vitro* and that fluorescently-tagged antigens adsorbed to aluminum precipitates can be found within inflammatory dendritic cells migrating from the site of injection (15, 39).

#### **1.4. Safety of Aluminum-Based Adjuvants.**

At the population level, Alhydrogel has an excellent safety profile and is associated with only mild local reactions, such as transient erythema (40, 41). The general safety of aluminum precipitates helps to explain the widespread and continued use of this adjuvant class (40, 41). However, a small subset of patients treated with Alhydrogel develop a range of serious local and systemic adverse events that are collectively described as *autoimmune/inflammatory syndrome induced by adjuvants* (ASIA) (42). One condition within this syndrome, macrophagic myofasciitis (MMF), is characterized by prolonged inflammation and pain at the site of injection along with arthralgia, muscle weakness, chronic fatigue and cognitive dysfunction (42, 43).

MMF is strongly associated with the persistence of Alhydrogel nanoparticles at the site of injection; electron micrographs of injection site biopsies from this population have found adjuvant particles sequestered within macrophages over 12-years from the time of administration (43). The persistence of Alhydrogel can be explained by the poor solubility of the adjuvant in biological fluids. For example, Seeber *et al.* found that 55% of amorphous aluminum hydroxyphosphate dissolved over 12 hours in a simulated interstitial fluid whereas no AlO(OH) dissolved over the same timeframe (44). Under supra-physiological conditions to promote dissolution (100 times the concentration of citric acid found *in vivo*), only ~8% of the AlO(OH) dissolved over a 5-day period compared to 100% for the amorphous aluminum adjuvant (44). These findings help to explain why the only aluminum-based adjuvant associated with MMF, and ASIA in general, is poorly crystalline Alhydrogel (42, 43).

The systemic adverse effects of ASIA are hypothesized to be due in part to the distribution of Alhydrogel nanoparticles from the injection site, which in turn facilitates an unwanted inflammatory response and damage in the distant tissue (42, 45, 46). Although the biodistribution of aluminum-based adjuvants is sparsely studied, there is emerging evidence to support this hypothesis.

### 1.5. Current State of Knowledge for the Biodistribution of Aluminum-Based Adjuvants.

As mentioned above, Alhydrogel consists of 1-12  $\mu\text{m}$  clusters of aggregated nanoparticles (12, 14). The forces holding the AlO(OH) nanoparticles together are rather weak, as exemplified by the fact that the clusters de-aggregate and re-aggregate during the process of antigen adsorption (47). De-aggregation of the adjuvant upon injection and exposure to interstitial fluid may release particles that can drain from the site of injection (47, 48). Particles  $<200$  nm, such as the component nanoparticles of Alhydrogel, efficiently enter the afferent lymphatics and drain to the lymph nodes within hours of injection (25, 48). When coated with antigen, these small particles are particularly effective at stimulating humoral immune responses since the unprocessed antigen can be recognized and efficiently phagocytosed by antigen-specific B cells in the lymph nodes (48). Particles  $>500$  nm, like Alhydrogel nanoparticle aggregates, largely remain at the site of injection and tend to also potentiate humoral immunity (19, 49). On the other hand, particles between 200-500 nm are efficiently phagocytosed, processed and transported over a period of days to the draining lymph node by dendritic cells; adjuvants within this size range tend to stimulate cell-mediated immune responses (48).

Flarend *et al.* used AlO(OH) containing a small amount of the positron emitter  $^{26}\text{Al}$  to elucidate details about the distribution and elimination of Alhydrogel following intramuscular administration into 2 rabbits (50). The distribution of  $^{26}\text{Al}$  was highest in the kidney followed by the spleen, liver, heart, non-draining lymph nodes and brain at 28-days post injection (50). From the blood AUC profile, it was estimated that 17% of the injected dose had been absorbed from the site of injection and 6% of the adjuvant had been excreted in the urine after 4 weeks (50). Although AlO(OH) is poorly soluble *in vivo*, the authors observed a large spike of  $^{26}\text{Al}$  in the blood within the first 48 hours followed by a low, steady level of the radiotracer over the next 26 days (50). Experts in the field simply assumed that AlO(OH) somehow dissolved more rapidly *in vivo* than observed *in vitro* by Seeber *et al.* (44, 50, 51). Although not assessed by Flarend *et al.*, the distribution of  $^{26}\text{Al}$ -AlO(OH) nanoparticles is an alternative explanation for the above pharmacokinetic results.

Only a handful of studies have directly assessed the biodistribution of the nanoparticles within aluminum-based adjuvants. In 1955, White *et al.* observed granular masses in the sinuses and macrophages of the draining lymph node 24 hours post-administration of an aluminum-precipitated vaccine in guinea pigs and rabbits (52). The authors assumed the granular substance was the adjuvant since it could not be found in the lymph node of control animals (52). Nearly 60 years later, researchers used both fluorescent latex beads and gadolinium oxide cores coated with aluminum oxide and rhodamine as surrogates of Alhydrogel to explore the adjuvant's biodistribution (45). The authors found that the surrogate materials translocated over time to distant organs, such as the spleen and brain, in a CCL2-dependent manner within predominantly macrophages (45). Ablation of the draining lymph nodes was found to significantly reduced the migration of the surrogate nanomaterials (45). Next, Eidi *et al.* functionalized the surface of Alhydrogel with hyperbranched polyglycerol (HPG) dendrimers conjugated to nanodiamonds as a way to trace the actual adjuvant *in vivo* (53). Like with the Alhydrogel analogues, fluorescent signals from the nanodiamonds could be found within sites like the draining

lymph node and spleen in a time-dependent manner (53). In 2015, Giusti *et al.* reported structures that resemble the component nanoparticles of an aluminum-based adjuvant in the draining lymph node 16-18 hours post-injection using electron microscopy (54).

There are indications in the literature that aluminum precipitates distribute from the site of injection and rather quickly appear within the blood and draining lymph node. However, the topic has been sparsely studied and remains rather controversial despite the widespread use of this adjuvant class. Novel tracers and techniques are required to better understand the behavior of Alhydrogel nanoparticles *in vivo*.

### **1.6. Hypothesis and Research Objectives**

The central hypothesis of this thesis is that the component nanoparticles of Alhydrogel are released from the site of injection and distribute to other regions of the body. The overall objective of this work is to improve the understanding of the biodistribution of aluminum-based adjuvants, particularly Alhydrogel. The specific research objectives are as follows:

1. To synthesize and characterize stable, traceable forms of Alhydrogel by doping the adjuvant's AlO(OH) crystal structure with different isotopes of indium
2. To assess the biodistribution of  $^{111}\text{In}$ -AlO(OH) using nuclear imaging techniques
3. To assess the kinetics and cellular distribution of  $^{115}\text{In}$ -AlO(OH) particles within the draining lymph nodes using a novel application of mass cytometry
4. To assess the persistence of Alhydrogel at the site of injection along with the distribution of adjuvant particles to the draining lymph node and liver using electron microscopy.

Knowing the biodistribution and cellular distribution of Alhydrogel can help better understand how the adjuvant potentiate immune responses and its side effect profile. Fundamental knowledge about Alhydrogel is also important as this adjuvant will continue to be widely used given its safety profile, ease of preparation, stability, immunostimulatory effects and incorporation into next-generation mixed-adjuvant systems like AS04 (55, 56).

## Chapter 2: Preparation and Characterization of Indium-Doped AlO(OH)

### 2.1. Introduction

Assessing the biodistribution of Alhydrogel is challenging since the adjuvant lacks any optical, magnetic or other properties that make it detectable (12). Flarend *et al.* developed the first traceable form of Alhydrogel, which consisted of AlO(OH) doped with the positron emitter  $^{26}\text{Al}$  (50). Although this radiotracer shed some light on the adjuvant's clearance, it could not differentiate between  $^{26}\text{Al}$  within an AlO(OH) nanoparticle or  $^{26}\text{Al}$  atoms released if the adjuvant dissolved (50). The first attempt to assess the biodistribution of the component nanoparticles in Alhydrogel used surrogate materials, such as fluorescent 500 nm latex nanoparticles, together with confocal microscopy and flow cytometry (45). Making conclusions from surrogate materials is difficult however since their composition, size, zeta potential, geometry and so forth differs substantially from Alhydrogel (45). The next approach to assess the pharmacokinetics of AlO(OH) nanoparticles electrostatically adsorbed nanodiamonds coated with hyperbranched polyglycerols onto the surface of Alhydrogel; epifluorescent microscopy was used to detect the location of the nanodiamonds within tissue sections (53). The problem with this strategy is that substances adsorbed to AlO(OH) purely via electrostatic interactions rapidly dissociate from the adjuvant upon exposure to biological fluids (57). For example, Morefield *et al.* found that dephosphorylated ovalbumin, which can only be adsorbed electrostatically, completely elutes from Alhydrogel within 30 minutes in lymph (57). It is unclear if the nanodiamonds remained bound to Alhydrogel *in vivo*, especially over the 21 day timeframe of this particular study (57). The traceable forms of Alhydrogel used so far have been less than ideal.

Reports have suggested that the biodistribution and cellular location of AlO(OH) nanoparticles can be assessed by staining tissues sections and cell isolates with morin or lumogallion, compounds that fluoresce in the presence of aluminum (39, 53, 58). Morin forms fluorescent complexes with various other cations, such as calcium and magnesium, resulting in a high false positive rate (53, 59). Although lumogallion is more specific for aluminum, its wide emission spectrum makes it difficult to combine with other fluorophores for immunophenotyping techniques like flow cytometry (53, 58). Using lumogallion pre-stained Alhydrogel *in vivo* is also problematic since the fluorophore decreases the zeta potential and increases the hydrodynamic size of the adjuvant (58).

Giusti *et al.* have recently used electron microscopy to directly observe preformed aluminum precipitates in the draining lymph node (54). X-ray spectroscopy coupled with electron microscopy can provide details about the composition and structure of the nanomaterials within tissue (60). However, this technique is low-throughput and presents a challenge when the phenotype of the adjuvant-positive cells has to be determined (60). Other techniques, such as ICP-MS, are required to determine the concentration of the aluminum-based adjuvant within a particular tissue/ organ system (60). However, dissolution of the samples in acid to conduct such an analysis results in the loss of critical information, such as whether the aluminum atoms were in a nanoparticle form (60).

Novel tracers and techniques are required to better study the biodistribution of Alhydrogel. The objective of this chapter was to synthesize a stable and traceable form of Alhydrogel by doping its AlO(OH) crystal structure with indium (Figure 2-1).

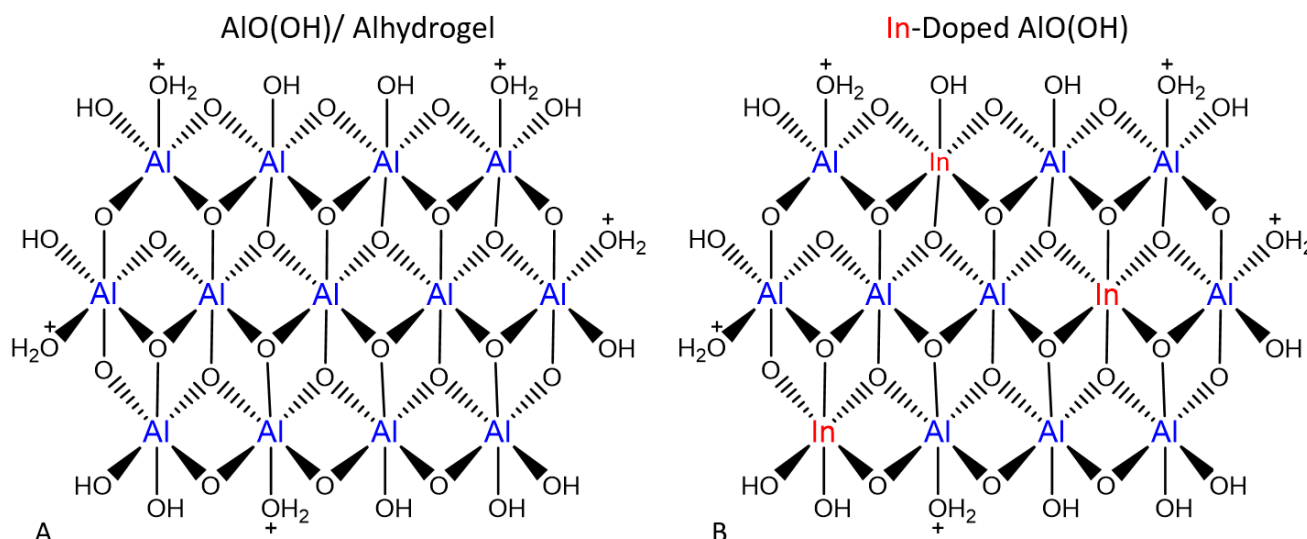


Figure 2- 1: Crystal structure of AlO(OH)/Alhydrogel (A) and the traceable indium-doped version of the adjuvant (B). Either <sup>111</sup>In or <sup>115</sup>In can be incorporated into the AlO(OH) matrix.

Two different isotopes of indium, gamma emitting <sup>111</sup>In and non-radioactive <sup>115</sup>In, were incorporated into the AlO(OH) matrix in order to trace of the adjuvant *in vivo* using novel techniques such as SPECT/CT (chapter 3) and mass cytometry (chapter 4), respectively. A number of physical, morphological and functional assessments were carried out in this chapter to first ensure that the indium-doped adjuvant closely matched Alhydrogel before proceeding with more tracking studies.

## 2.2. Materials and Methods

### 2.2.1. Synthesis of AlO(OH)

A protocol was derived from papers by Xu *et al.* and Yau *et al.* to synthesis AlO(OH) nanoparticle aggregates that closely resemble commercial Alhydrogel (61, 62). Briefly, 50  $\mu$ L of 0.1 N HCl (Sigma 258148) was added to 1 mL of 0.32 M AlCl<sub>3</sub>·6H<sub>2</sub>O (Alfa Aesar 10622) in 18 M $\Omega$  water (pH 1.5). After heating the solution to 50°C in an oil bath, 175  $\mu$ L of NH<sub>4</sub>OH (Fisher A669-212) was added rapidly to precipitate the metal salts (pH 10). After 2 hours of curing (50°C, 200 rpm), the AlO(OH) was washed thrice with 2 mL of 18 M $\Omega$  water; centrifugation at 1800 g was used to pellet the adjuvant between washes and light vortexing was used to re-suspend the aggregates. The AlO(OH) was re-suspended to a final volume of 1.2 mL with 18 M $\Omega$  water and autoclaved using liquid settings (121°C, 15 psi, 30 minute hold, slow vent). The sterile adjuvant was stored at room temperature until used.

### 2.2.2. Synthesis of <sup>115</sup>In-Doped AlO(OH)

<sup>115</sup>InCl<sub>3</sub>·4H<sub>2</sub>O (Strem Chemicals 93-4931) in 50 μL 0.1N HCl, was added to 1 mL of 0.32 M AlCl<sub>3</sub>·6H<sub>2</sub>O in 18 MΩ water (pH 1.5); up to 10% of the aluminum atoms were substituted for indium. The mixture of metal salts was co-precipitated with base and processed as described in section 2.2.1.

### 2.2.3. Synthesis of <sup>111</sup>In-Doped AlO(OH)

Up to 340 MBq of carrier free <sup>111</sup>InCl<sub>3</sub> in 0.05 N HCl (Nordion IPG-In-111) was diluted to a volume of 50 μL with 0.1 N HCl and added to 1mL of 0.32 M AlCl<sub>3</sub>·6H<sub>2</sub>O in 18 MΩ water (pH 1.5). The mixture of metal salts was co-precipitated with base and processed as described in section 2.2.1.

### 2.2.4. Encapsulation Efficiency of <sup>111</sup>In within the AlO(OH) Matrix

Before washing the adjuvant thrice with 18 MΩ water, 1 μL was spotted onto an instant thin layer chromatography (ITLC) strip (BioDex 150-771) and developed with 0.1 M EDTA at pH 4 (Sigma E4884). In this system, <sup>111</sup>In-AlO(OH) remains at R<sub>f</sub>=0 while unincorporated <sup>111</sup>In forms a complex with EDTA and migrates to R<sub>f</sub>=1 (63). The location of the radioactivity on the ITLCs was visualized using a Cyclone Phosphor Imager with a photostimulable phosphor screen (Perkin Elmer) and analyzed with OptiQuant software (Perkin Elmer). Encapsulation efficiency was also assessed by measuring the amount of <sup>111</sup>In in the supernatant as the adjuvant was washed using a CRC-55tR dose calibrator (Capintec). Encapsulation efficiency was calculated using the following equation:

$$\text{Encapsulation Efficiency (\%)} = \left[ \frac{\text{Total } ^{111}\text{In} - \text{Unincorporated } ^{111}\text{In}}{\text{Total } ^{111}\text{In}} \right] \times 100$$

### 2.2.5. Concentration and Specific Activity

The concentration of <sup>111/115</sup>In-AlO(OH) was determined by lyophilizing a known volume overnight in a FreeZone 2.5 Freeze Dry System (Labconco) and measuring the weight of the solid fraction. The specific activity of the <sup>111</sup>In-AlO(OH) was determined by measuring the amount of radioactivity in a known weight of lyophilized adjuvant with a dose calibrator. Concentration was reported as % w/v while specific activity was reported as μCi/μg.

### 2.2.6. Powder X-Ray Diffraction (PXRD)

After centrifuging the adjuvant at 10,000 g for 5 minutes and aspirating the supernatant, the pellet was dried at 80°C for 2.5 hours. Each sample was ground into a fine powder and loaded into a D8-Advance Diffractometer (Bruker) in Bragg-Brentano configuration; a copper source was used with a nickel filter leaving CuK<sub>α</sub> radiation (λ = 1.54 Å). The generator was set at 40 kV and 40 mA and the slit sizes were 1.0 mm (divergence), 8.0 mm (anti-scatter) and 2.5° (soller). PXRD data was collected from 5° to 90° 2θ and analyzed with TOPAS software (Bruker).

### 2.2.7. *Dynamic Scanning Calorimetry (DSC)*

Samples were dried as described for PXRD, loaded into aluminum pans (DSC Consumables 84006) and placed into a DSC Q100 (TA Instruments). DSC measurements were taken from 40-500°C at a ramp rate of 20°C/minute. The data was analyzed using Universal Analysis software (TA Instruments) and reported as heat flow (mW/g) versus temperature (°C).

### 2.2.8. *Fourier Transform Infrared Spectroscopy (FTIR)*

Samples for FTIR analysis were dried as described for PXRD and loaded into a Frontier spectrometer outfitted with a UATR sampling system (Perkin Elmer). Data was recorded from 550 to 4000 cm<sup>-1</sup> and analyzed with Spectrum software (Perkin Elmer).

### 2.2.9. *Dynamic Light Scattering (DLS)*

Particle size and zeta potential analysis were conducted using a Zetasizer Nano ZS (Malvern) and folded capillary zeta cell (Malvern DTS1070). <sup>111/115</sup>In-AIO(OH) or commercial Alhydrogel were diluted 10-fold in 18 MΩ water (viscosity: 0.8872 cP, refractive index: 1.330, dielectric constant: 78.5) and allowed to equilibrate to 25°C before being analyzed. The refractive index for the adjuvant was set at 1.650 with no absorptivity at λ=632 nm (k=0.00). The angle of detection was 173° backscatter with automatic attenuation. Micro-electrophoretic measurements used a Smoluchowski model (F(ka)=1.5). The average (number %) of 10 measurements of 30 seconds was reported for the hydrodynamic size of each sample, unless otherwise specified. The average of at least 15 measurements was reported for the zeta potential of each sample.

### 2.2.10. *Scanning Transmission Electron Microscopy (STEM)*

To better visualize the morphology of the nanoparticles within the adjuvant's aggregates, samples were first diluted 100-fold with 18 MΩ water and sonicated at 60 W for 5 minutes on ice with a Ultrasonic 3000 equipped with a stepped micro-tip (BioLogics) (14). Between 0.5-1 μL of sample was placed onto formvar and carbon backed 200 mesh copper grids (Ted Pella 01810) and allowed to dry for at least 24 hours in a laminar hood. The samples were examined in a Technai Osiris STEM with a Schottky field emission electron source operating at 200 kV (FEI). An Ultrascan 1000XP-P CCD camera (Gatan) along with high-angle annular dark field (HAADF) and bright field STEM detectors (FEI) were used to perform a high-resolution assessment of the adjuvant's morphology on the Osiris platform. This microscope was also equipped with a Super-X windowless energy-dispersive X-ray (EDX) detection spectrometer (FEI) for elemental mapping. Esprit 1.9 software (Bruker) was used to correct for Bremsstrahlung radiation and analyze the EDX data.

### 2.2.11. *Stability of <sup>111</sup>In-AIO(OH) in Different Media over Time*

Twenty microliters of autoclaved <sup>111</sup>In-AIO(OH) was incubated under sterile conditions with 480 μL of saline, 0.1 M EDTA at pH 7 or fetal bovine serum (Life Technologies 12483020) at 37°C with end-over-end

mixing for 10 days. At set times during the incubation (0, 2 and 10 days), the adjuvant was pelleted at 10,000 g for 5 minutes and 200  $\mu\text{L}$  of the supernatant was removed to measure the amount of free  $^{111}\text{In}$  using a Wizard<sup>2</sup> 2470 gamma counter (Perkin Elmer). Fresh diluent was added to replace the removed 200  $\mu\text{L}$  before continuing the incubation. Stability was reported as the cumulative amount of  $^{111}\text{In}$  released over time.

#### 2.2.12. Protein Adsorptivity

Alhydrogel or  $^{111/115}\text{In-AIO(OH)}$  were mixed with an equal volume of 0-20 mg/mL ovalbumin (OVA; Sigma A5503) in normal saline and allowed to adsorb for 30 minutes at room temperature (57). The adjuvant was pelleted at 10,000 g for 5 minutes and 10  $\mu\text{L}$  of the supernatant was removed to detect unbound OVA using a fluorescamine assay. Briefly, the supernatant was diluted in 80  $\mu\text{L}$  of 18 M $\Omega$  water before the addition of 10  $\mu\text{L}$  of 3 mg/mL fluorescamine (Sigma F9015) in acetone (57, 64). Data was acquired using a Synergy MX plate reader (BioTek) measuring fluorescence at 380/464 nm (64).

#### 2.2.13. Protein De-Adsorption in Biological Fluids

The model antigen OVA was dissolved in 0.1 M sodium bicarbonate buffer pH 8.5 (Fisher S233-10) and fluorescently tagged by the addition of 10 molar-excess of AlexaFluor-555 succinimidyl ester (AF555; Life Technologies A20009) (65). After 2 hours at room temperature, unreacted dye was removed and the protein was buffer exchanged into saline using a 30 kDa MWCO micro-concentrator (Merck UFC503096). Alhydrogel or  $^{111/115}\text{In-AIO(OH)}$  was mixed with an equal volume of 2 mg/mL AF555-OVA and allowed to adsorb for 30 minutes at room temperature (57). Twenty microliters of the protein adsorbed adjuvant was incubated with 230  $\mu\text{L}$  of saline or FBS for 30 minutes. The adjuvant was pelleted down at 10,000 g for 5 minutes and 100  $\mu\text{L}$  of supernatant was removed to measure fluorescence at 555/572 nm using a Synergy MX plate reader (BioTek) (57, 65). The quantity of protein in the supernatant was determined using a standard curves of AF555-OVA in saline or FBS.

#### 2.2.14. Cellular Toxicity Assays

HEK293 is a cell line commonly used to assess cellular toxicity (66). HEK293 cells were cultured in high-glucose DMEM supplemented with L-glutamine and sodium pyruvate (Life Technologies 11995065) along with 10% FBS and 1% penicillin/ streptomycin (Life Technologies 15140122) (67). The cells were maintained in an incubator at 37°C with 5% CO<sub>2</sub> and split using a solution of 0.25% trypsin/EDTA (Life Technologies 25200056) when they reached ~70% confluence (67). To perform the toxicity assays, HEK293 cells were seeded at 5000 cells/well in 96-well plates (Corning 353072) and allowed to adhere overnight before the addition of 0-500  $\mu\text{g/mL}$  adjuvant. Two different assays were used to assess toxicity:

1. *MTT Assay for Cellular Respiration*: two days post-addition of the adjuvant, 20  $\mu\text{L}$  of 5 mg/mL thiazolyl blue tetrazolium bromide (MTT reagent; Sigma M5655) in 1x PBS was added to each well and placed back into the cell incubator for 2 hours (68, 69). The MTT reagent is converted into insoluble formazan crystals within the mitochondria of living cells (68, 69). After aspirating the supernatant, the formazan and adjuvant particles were dissolved with the addition of 150  $\mu\text{L}$  of DMSO (Fisher D128) (68, 69). Data was acquired using a Synergy MX plate reader (BioTek) measuring absorbance at 540 nm (68, 69). A correction factor was applied to account for a red-shift in the absorption spectrum of formazan due to the complexation of the molecule with aluminum and indium ions (70). Data was reported as percent respiration of untreated HEK293 cells.
2. *YOYO-1 Assay for Cell Death*: each well was supplemented with 0.75  $\mu\text{M}$  of YOYO-1 dye (Life Technologies Y3601) at the same time as the addition of the adjuvant. YOYO-1 is membrane impermeable DNA-binding dye that fluorescently labels the nucleus of dead cells with a compromised membrane (71, 72). The plate was serially scanned every 2 hours for 2 days in an IncuCyte Zoom (Essen Bioscience) recording both green fluorescence and phase contrast data (72). Cell death was reported as green channel fluorescence confluence versus time (72).

#### 2.2.15. Humoral Immune Response Assessment

C57BL/6 mice (6-8 weeks old) were injected in the posterior half of the dorsal surface with 100  $\mu\text{g}$  of OVA adsorbed to 0.7 mg of either  $^{111/115}\text{In-AIO(OH)}$  or Alhydrogel in a total volume of 100  $\mu\text{L}$ . Two weeks post immunization, blood was collected via heart puncture and allowed to clot on ice. After centrifuging the blood at 5000 g for 10 minutes, the serum was removed and stored at  $-20^{\circ}\text{C}$  until analyzed via ELISA for anti-OVA antibodies.

To perform the ELISA, Nunc-Immuno MaxiSorp 96-well plates (Fisher 439454) were first coated with antigen by incubating 100  $\mu\text{L}$  of 20  $\mu\text{g}/\text{mL}$  OVA overnight at  $4^{\circ}\text{C}$  in 50 mM sodium bicarbonate buffer at pH 9.6 per well (73). After removing the coating solution, the plate was blocked with 150  $\mu\text{L}$  of 2% bovine serum albumin (BSA; Sigma A7030) in 1xPBS for 1 hour at  $37^{\circ}\text{C}$ . The plate was washed twice with 200  $\mu\text{L}$  of 0.05% Tween-20 (Sigma P9416) in 1xPBS (PBS-T) before the addition of 100  $\mu\text{L}$  of diluted serum in 0.1% BSA in 1xPBS per well; the serum was diluted 1/4000-1/32000 to assess total IgG and IgG1 and 1/400-1/3200 for IgG2c (73). After 2 hours at room temperature, the plate was washed twice with PBS-T and once with 1xPBS before adding 100  $\mu\text{L}$  of the HRP-conjugated secondary antibodies listed in Table 2-1 (73).

Target	Dilution	Vendor	Catalogue Number
Total IgG (goat anti-mouse)	1/50,000	Jackson ImmunoResearch	115-035-003
IgG1 (rabbit anti-mouse)	1/32,000	Zymed	61-0120
IgG2c (goat anti-mouse)	1/10,000	Jackson ImmunoResearch	115-035-208

Table 2- 1: Secondary antibodies used to detect anti-OVA antibodies.

After 1 hour incubation with the secondary antibody, each well was washed twice with 200  $\mu$ L of PBS-T and twice with 200  $\mu$ L of 1xPBS (73). One hundred microliters of TMB substrate (eBioscience 00420156) was added to each well and developed for 1 hour at room temperature before stopping the reaction with 50  $\mu$ L of 2 N H<sub>2</sub>SO<sub>4</sub> (Fisher 351293) (73). Data was read using a Synergy MX plate reader (BioTek) measuring absorbance at 450 nm (73). Data was always compared to a naïve/non-immunized age-matched mouse.

#### 2.2.16. Cellular Immune Response Assessment

C57BL/6 mice were immunized as previously described in section 2.2.15. One week post-administration, peripheral blood was collected from the saphenous vein and treated with ACK buffer (0.15 M NH<sub>4</sub>Cl, 10 mM KHCO<sub>3</sub>, 0.1 mM EDTA at pH 7.2) to osmotically lyse the red blood cells (74). The cells were washed with FACS buffer (4% v/v FBS, 2 mM EDTA in 1xPBS) and incubated with 2.4G2 tissue culture supernatant for 15 minutes to block the Fc receptors (74). The cells were then stained with the markers listed in Table 2-2 for 45 minutes on ice (74):

Antibody/Probe	Fluorochrome	Clone	Dilution	Vendor	Catalogue Number
CD3	AF405	KT31.1	1/25	AbLab (UBC)	45-0034-05
Ovalbumin Tetramer	PE	Residues 257-164 of ovalbumin on H2-Kb tetramer	1/50	Tan Laboratory (UBC CFRI)	
CD8	PE-Cy7	53-6.7	1/3000	eBioscience	25-0081-81

Table 2- 2: Panel for OVA-tetramer staining.

The cells were then incubated with 1  $\mu$ g/mL of 7-amino-actinomycin (7AAD; Sigma A9400) for 5 minutes as the live/dead discriminator (74). The cells were washed twice with FACS buffer and analyzed using a CytoFlex 13-color flow cytometer (Beckman). A minimum of 100,000 events/sample was collected and the data was analyzed using FlowJo V10 software (TreeStar). Data was always compared to a naïve age-matched mouse.

#### 2.2.17. Data Analysis

Data are presented as mean  $\pm$  standard deviation unless otherwise specified. GraphPad Prism 7 was used for statistical analysis using Student's t-test or ANOVA followed by multiple comparisons testing (Dunnet's test). P<0.05 was considered statistically significant and was indicated by an asterisks (\*). Data was graphed using either GraphPad Prism 7 or OriginPro 9.

#### 2.2.18. Ethics Statement

All animal experiments were carried out in accordance with the guidelines of the University of British Columbia's Animal Care Committee under the approved protocol A14-0159.

## 2.3. Results

### 2.3.1. Encapsulation Efficiency, Concentration and Specific Activity of $^{111/115}\text{In-AIO(OH)}$

ITLC analysis (Figure 2-1) showed that the  $^{111}\text{InCl}_3$  did not precipitate when added to the  $\text{AlCl}_3$  solution, since the radionuclide migrated to  $R_f=1$ . After the addition of base, the vast majority of  $^{111}\text{In}$  remained at  $R_f=0$  since it was entrapped within the  $\text{AlO(OH)}$  matrix. Integration of the ITLC data found the encapsulation efficiency of  $^{111}\text{In}$  to be  $99.6 \pm 0.1\%$ .

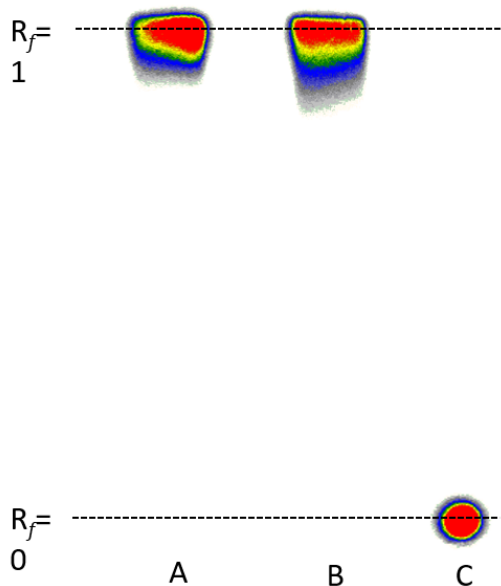


Figure 2- 2: Encapsulation efficiency of  $^{111}\text{In}$  within  $\text{AlO(OH)}$ .  $^{111}\text{InCl}_3$  in 0.05N HCl from Nordion (A) and when mixed with 0.32M  $\text{AlCl}_3$  before (B) and after (C) the addition of base to co-precipitate the metal salts.

Although the encapsulation efficiency was high,  $\sim 15\%$  of the  $^{111/115}\text{In-AIO(OH)}$  nanoparticles adsorbed to the wall of the polypropylene vessel used to autoclave the adjuvant and could not be recovered. The final concentration of the  $^{111/115}\text{In-AIO(OH)}$  was determined to be  $1.39 \pm 0.04\%$  w/v; each batch of adjuvant was diluted with a specific amount of 18 M $\Omega$  water to match the concentration of Alhydrogel at 1.3% w/v. The specific activity of the  $^{111}\text{In-AIO(OH)}$  was 12.58 MBq/mg, a sufficiently high value to preform the SPECT/CT study described in chapter 3.

### 2.3.2. Stability of $^{111}\text{In-AIO(OH)}$ in Different Media

$^{111}\text{In-AIO(OH)}$  was incubated in different diluents at  $37^\circ\text{C}$  to assess its stability over time (Figure 2-2). Only  $1.60 \pm 0.04\%$  of the tracer dissolved after 10 days in FBS, a diluent used to simulate the interstitial fluid in contact with the adjuvant upon injection. Only  $7.77 \pm 0.22\%$  of the adjuvant dissolved after 10 days in 0.1M

EDTA, a strong chelator for aluminum and indium atoms that promotes that dissolution of  $^{111}\text{In}-\text{AlO}(\text{OH})$  (44, 75, 76). The adjuvant was stable in saline.

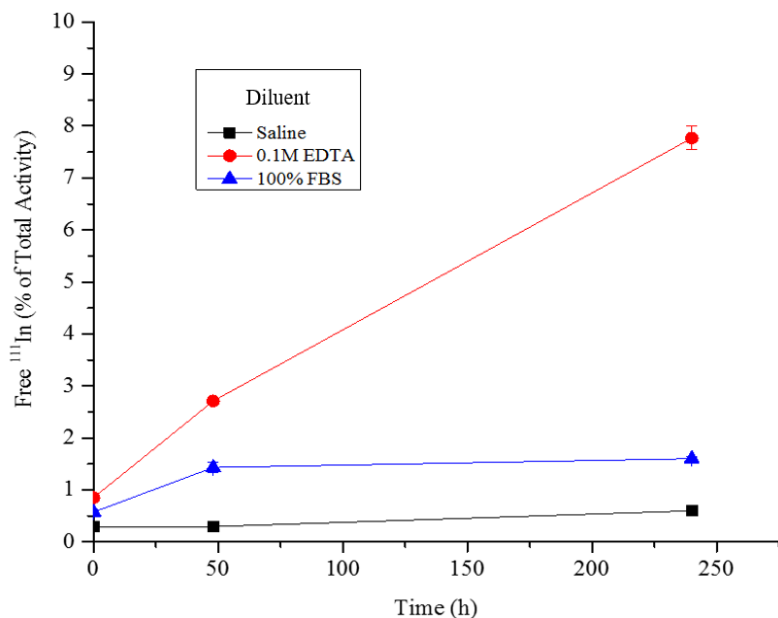


Figure 2- 3: Stability of  $^{111}\text{In}-\text{AlO}(\text{OH})$  in different diluents over time.

### 2.3.3. Physical Characterization of Alhydrogel

PXRD analysis of Alhydrogel (Figure 2-3) confirmed previous reports that the adjuvant has a structure consistent with  $\text{AlO}(\text{OH})$  (12). The broad diffraction peaks highlight that the adjuvant is poorly crystalline in nature (12). Signals at  $18.774$  and  $20.224^\circ 2\theta$  suggest that the batch of Alhydrogel tested (Batch 5012) contained a small amount of more crystalline  $\text{Al}(\text{OH})_3$  (5).

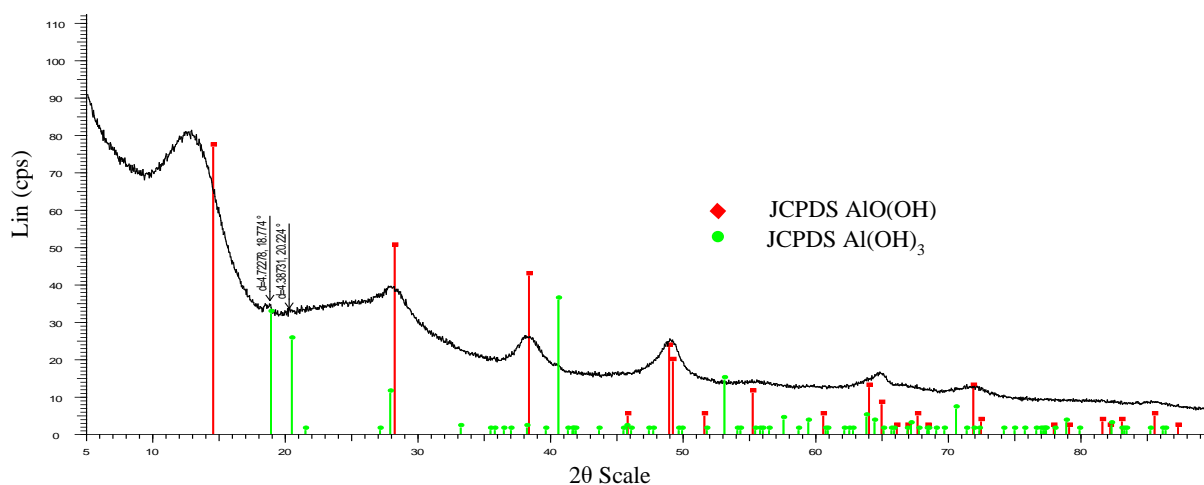


Figure 2- 4: PXRD of Alhydrogel.

DSC analysis of Alhydrogel (Figure 2-4A) showed characteristic endothermic peaks at 110°C and 420°C for AlO(OH) (77). The endothermic peak at ~290°C was characteristic for Al(OH)<sub>3</sub> and confirms the above PXRD results (78). The FTIR analysis of Alhydrogel (Figure 2-4B) matched the spectrum for AlO(OH) with a broad peak at 3100-3700 cm<sup>-1</sup>, representative of the hydroxylated surface, and additional peaks at 750, 883, 1072 and 1639 cm<sup>-1</sup> (61).

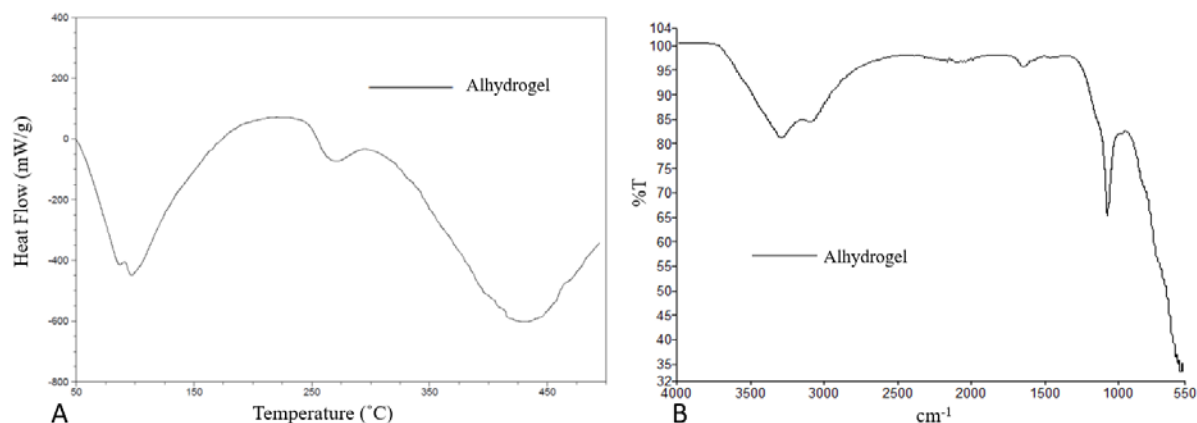


Figure 2- 5: DSC (A) and FTIR(B) analysis of Alhydrogel.

#### 2.3.4. Physical Characterization of <sup>111/115</sup>In-AlO(OH)

Batches of <sup>115</sup>In-AlO(OH) with increasing amounts of dopant were characterized with PXRD (Figure 2-5). Up to 5% of the aluminum atoms could be replaced by <sup>115</sup>In without affecting the adjuvant's crystal structure. Above that level of doping, a combination of <sup>115</sup>In(OH)<sub>3</sub> and <sup>115</sup>In-AlO(OH) were produced. None of the <sup>115</sup>In-AlO(OH) adjuvants assessed using PXRD contained any Al(OH)<sub>3</sub>. 2.5% <sup>115</sup>In-AlO(OH) was selected for downstream assessments as this formulation contained a sufficient amount of dopant for detection with a mass cytometer (See section 4.3.1). <sup>111</sup>In-AlO(OH) was not analysed by PXRD.

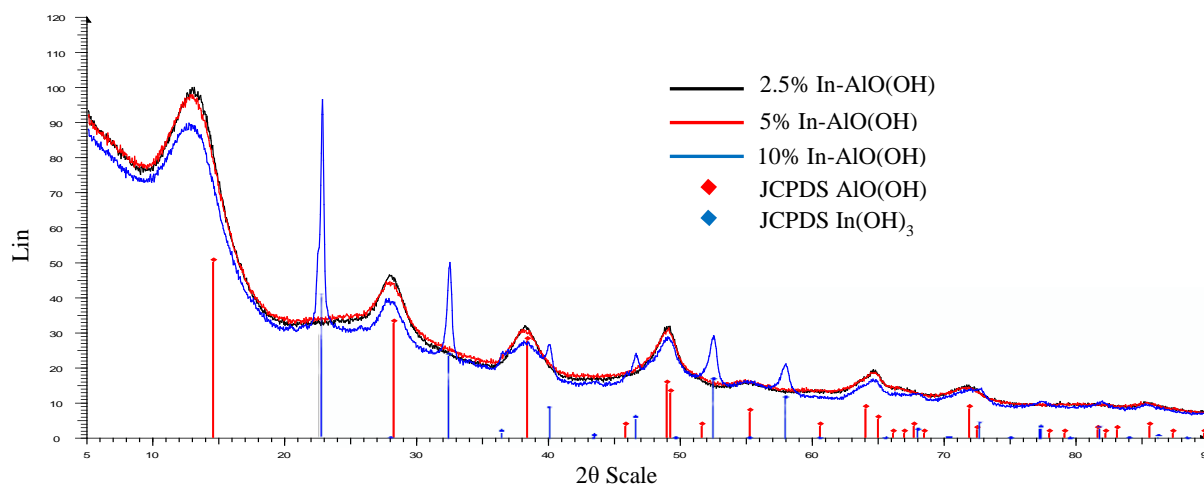


Figure 2- 6: PXRD of 2.5-10% <sup>115</sup>In-AlO(OH).

DSC and FTIR analysis of  $^{111}\text{In-AIOOH}$  and 2.5%  $^{115}\text{In-AIO(OH)}$  confirmed that both adjuvants were  $\text{AlO(OH)}$  (Figure 2-6) (61, 77). These assays further confirmed the absence of  $\text{Al(OH)}_3$  in the doped-adjuvants.

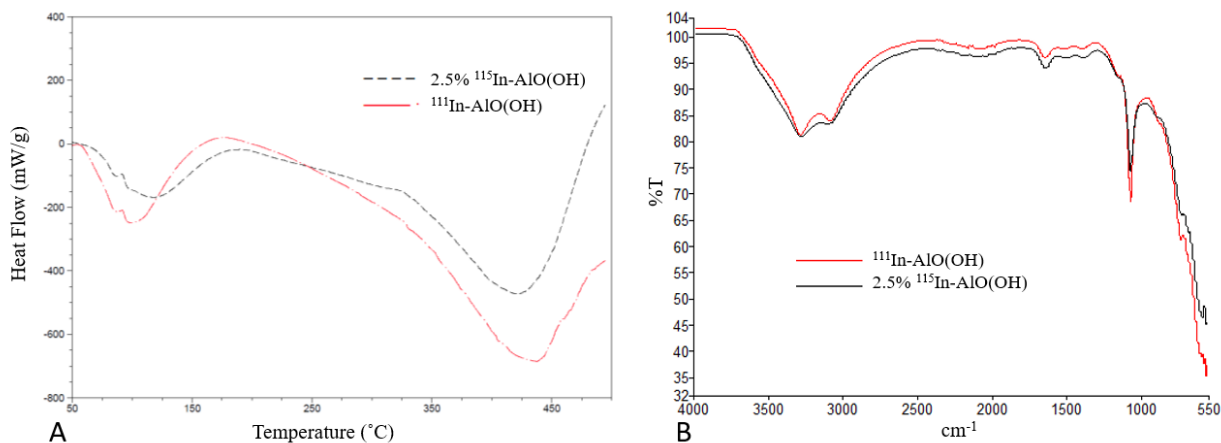


Figure 2- 7: DSC (A) and FTIR (B) analysis of 2.5%  $^{115}\text{In-AIO(OH)}$ .

### 2.3.5. Hydrodynamic Size and Zeta Potential of $^{111/115}\text{In-AIO(OH)}$ and Alhydrogel

Dynamic light scattering analysis (Figure 2-7) showed that the hydrodynamic size and zeta potential of  $^{111}\text{In-AIO(OH)}$  and 2.5%  $^{115}\text{In-AIO(OH)}$  were not statistically different from Alhydrogel. The adjuvants consisted of  $\sim 1500$  nm aggregates with a slight positive charge. These observations are consistent with previous reports in the literature for Alhydrogel from Stanley Hem's group (12).

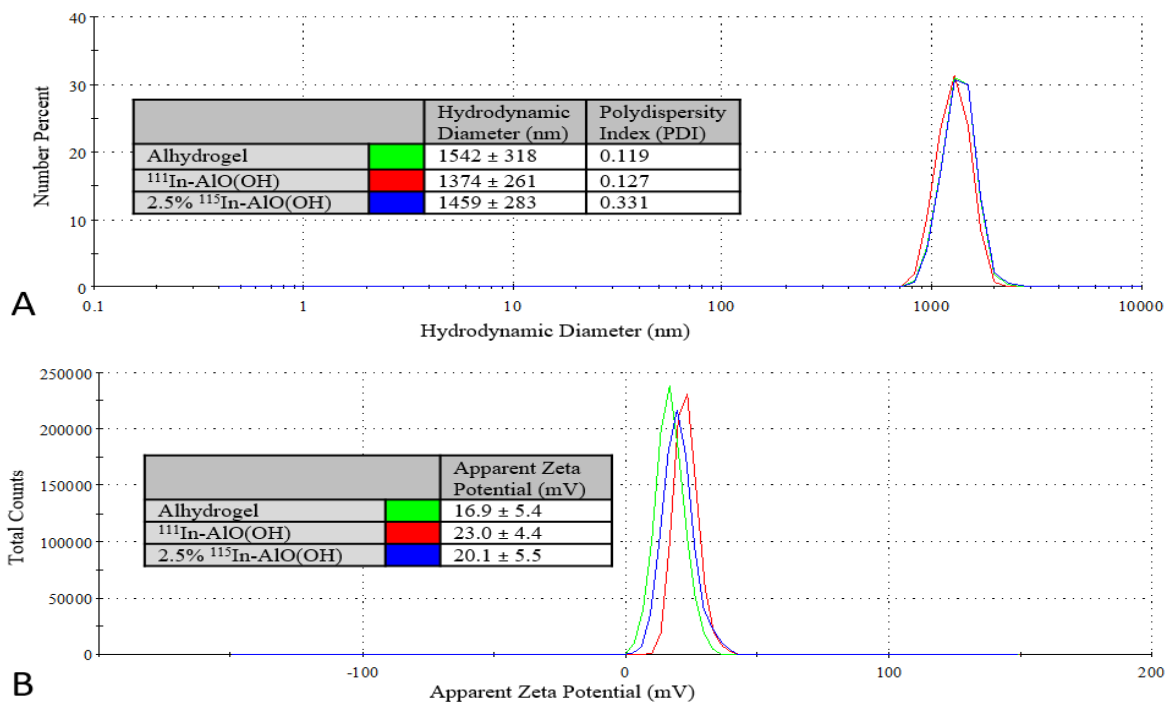


Figure 2- 8: Hydrodynamic size (A) and zeta potential (B) of  $^{111/115}\text{In-AIO(OH)}$  and Alhydrogel.

### 2.3.6. Particle Morphology and Spatial Location of $^{115}\text{In}$ Dopant within $\text{AlO}(\text{OH})$ Nanoparticles

The aggregate nature of Alhydrogel makes it challenging to assess the morphology of the adjuvant (14). Alhydrogel and 2.5%  $^{115}\text{In}$ - $\text{AlO}(\text{OH})$  were sonicated to disrupt the aggregates to better visualize the nanoparticles under STEM imaging (14). Figure 2.8 shows that the hydrodynamic size of the adjuvants were reduced from  $\sim 1500$  nm to between 10-100 nm upon sonication.

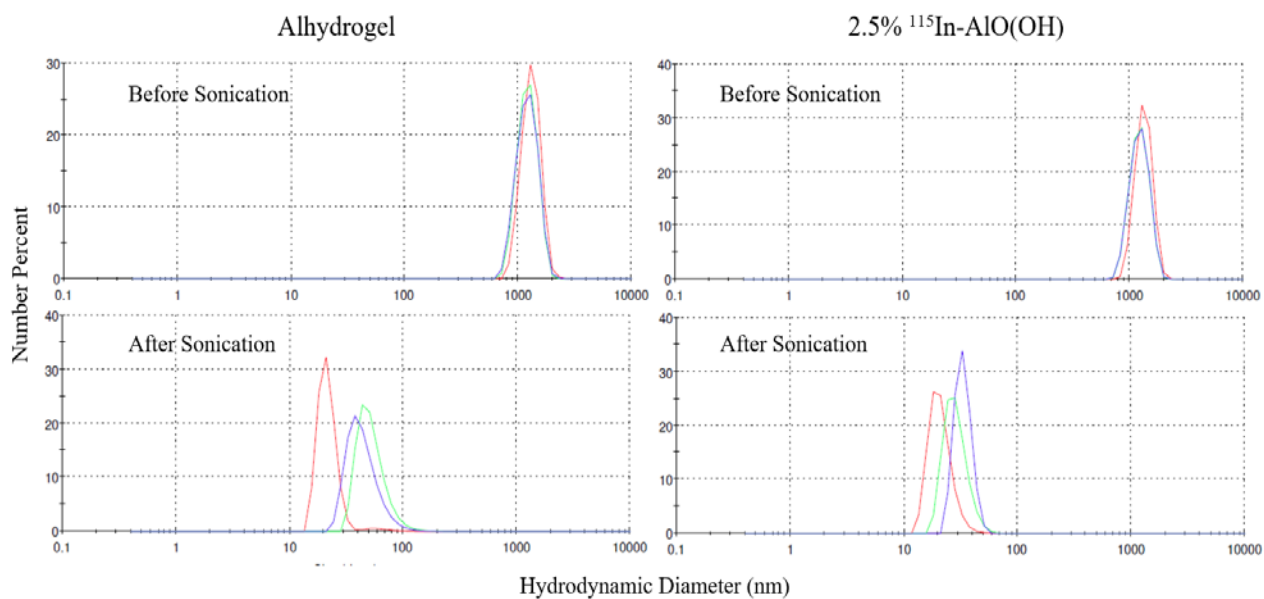


Figure 2- 9: Alhydrogel and 2.5%  $^{115}\text{In}$ - $\text{AlO}(\text{OH})$  before and after sonication in preparation for STEM imaging. Each line represents a triplicate measurement of 30 seconds.

STEM imaging (Figure 2-9) showed that 2.5%  $^{115}\text{In}$ - $\text{AlO}(\text{OH})$  was composed of aggregated nanoparticles with a similar high-aspect ratio morphology to the commercial adjuvant. The average size of the nanoparticles within the doped adjuvant was  $10.02 \pm 2.11$  nm by  $5.41 \pm 1.29$  nm, comparable to the dimensions of the Alhydrogel nanoparticles (12).

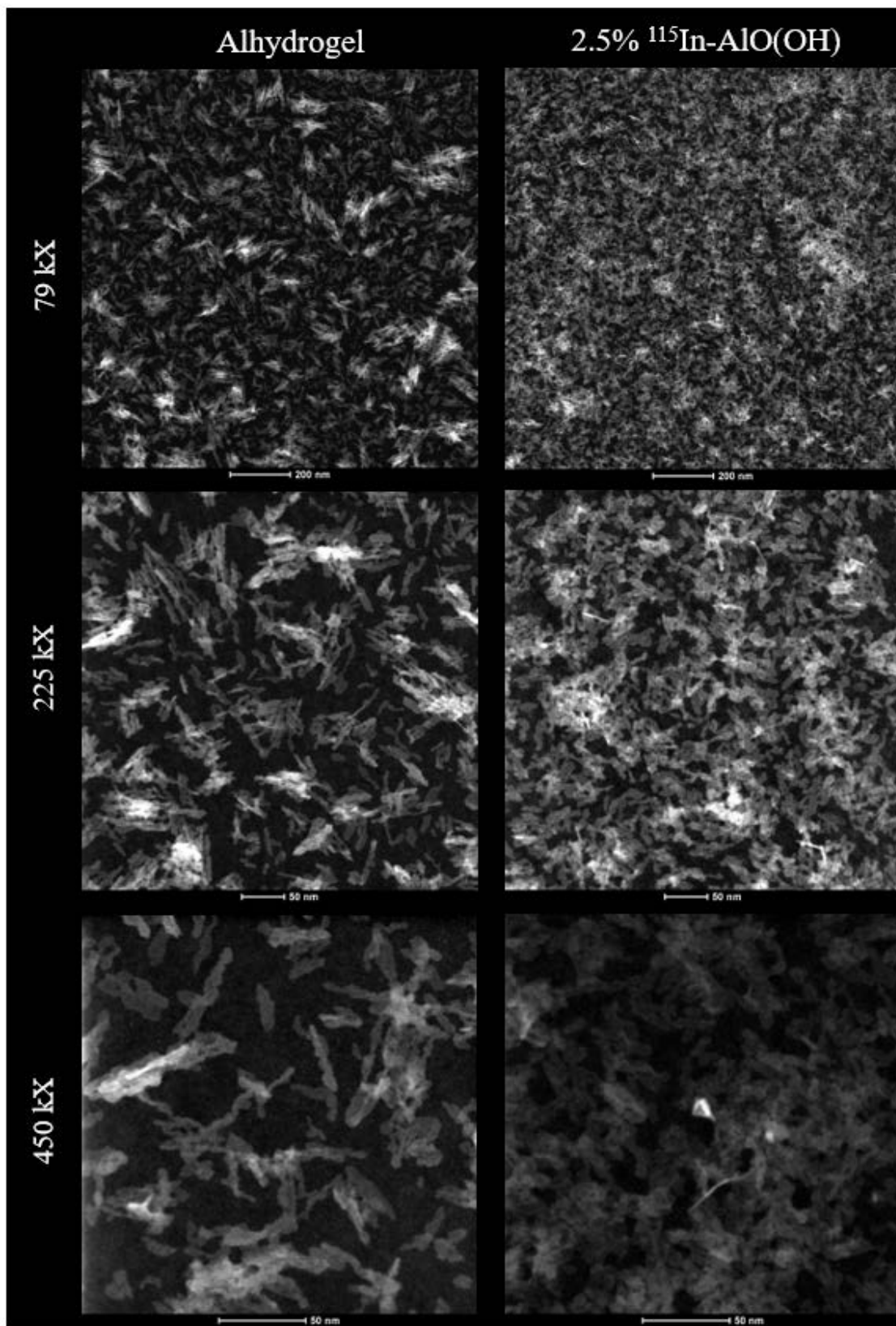


Figure 2- 10: STEM images comparing the morphology of Alhydrogel (left) to 2.5% <sup>115</sup>In-AlO(OH) (right) at increasing levels of magnification from the top to bottom panels. Note that the concentration of the 2.5% <sup>115</sup>In-AlO(OH) loaded onto the TEM grids was ~1.5x more concentrated than Alhydrogel.

Elemental mapping of Alhydrogel (Figure 2-10) confirmed that the adjuvant is composed of aluminum and oxygen atoms; hydrogen cannot be atomically mapped with STEM (12). Elemental mapping also confirmed that the commercial adjuvant does not contain any indium.

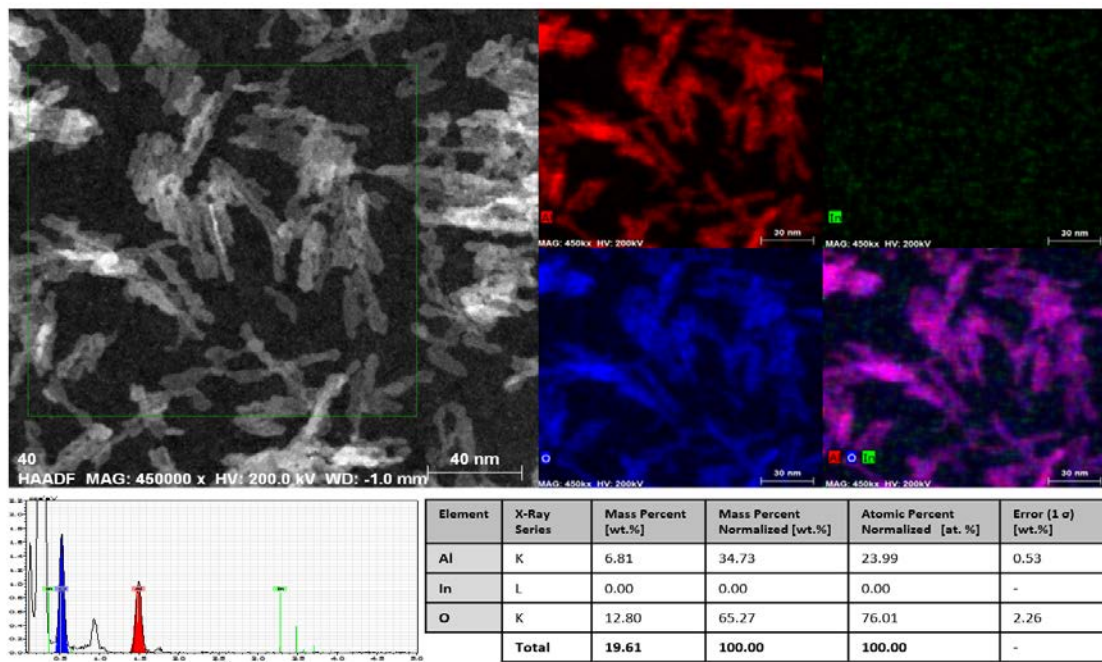


Figure 2- 11: Elemental mapping of Alhydrogel. The top panel shows a reference HAADF image and the distribution of aluminum (red), indium (green) and oxygen (blue) within the adjuvant. The bottom panel shows the EDX spectrum (left) and results from the quantification of the EDX data (right).

Elemental mapping of 2.5%  $^{115}\text{In}$ -AIO(OH) (Figure 2-11) showed that the dopant was evenly dispersed through the AIO(OH) nanoparticles. Quantification of the EDX spectrum from 3 different regions found that the amount of indium was equivalent to  $2.55 \pm 0.21\%$  of the aluminum atoms. This finding shows that most, if not all, of the  $^{115}\text{In}$  was incorporated into the AIO(OH) matrix and corroborates the results from section 2.3.1 with  $^{111}\text{In}$ -AIO(OH). Radioactive  $^{111}\text{In}$ -AIO(OH) was not assessed with STEM.

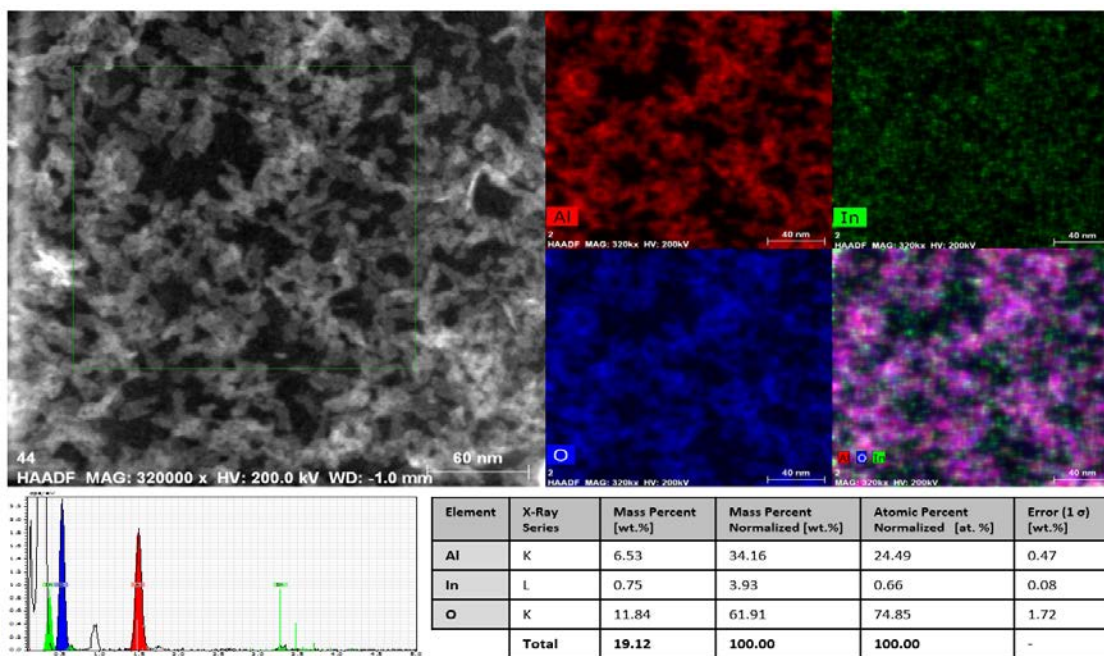


Figure 2- 12: Elemental mapping of 2.5%  $^{115}\text{In-AIO(OH)}$ . The top panel shows a reference HAADF image and the distribution of aluminum (red), indium (green) and oxygen (blue) within the adjuvant. The bottom panel shows the EDX spectrum (left) and results from the quantification of the EDX data (right).

### 2.3.7. Protein Adsorptivity and De-Adsorptivity Assays to $^{111/115}\text{In-AIO(OH)}$ and Alhydrogel

Alhydrogel,  $^{111}\text{In-AIO(OH)}$  and 2.5%  $^{115}\text{In-AIO(OH)}$  adsorbed the model antigen OVA to a similar extent, as illustrated in Figure 2-12A. The adsorptive ability of the adjuvants, between 10-20 mg/mL, was similar to the manufacturer's specifications for 1.3% w/v Alhydrogel using human serum albumin (12-20 mg/mL) (79).

Upon exposure to FBS (Figure 2-12B), which was used as a surrogate for interstitial fluid at the injection site, ~65% of the adsorbed AF555-OVA was released from the AIO(OH) particles. The degree of antigen de-adsorption was not statistically different between  $^{111/115}\text{In-AIO(OH)}$  and commercial Alhydrogel. A similar degree of de-adsorption was reported for OVA coated to Alhydrogel in the presence of lymph by Morefield *et al.* (57). The antigen was not eluted upon dilution in saline for all adjuvants tested.

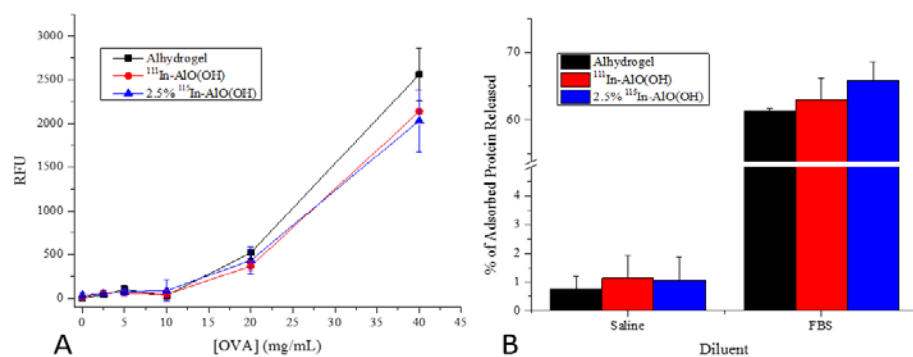


Figure 2- 13: OVA adsorptivity (A) and de-adsorptivity (B) to Alhydrogel and  $^{111/115}\text{In-AIO(OH)}$ .

### 2.3.8. Cellular Toxicity of $^{115}\text{In-AIO(OH)}$ and Alhydrogel

Figure 2-13A shows representative micrographs from the YOYO-1 assay for cells treated with up to 500  $\mu\text{g/mL}$  over time. Dead cells with disrupted membranes become fluorescent due to the presence of the YOYO-1 indicator dye (72). Due to the presence of the adjuvant particles on the bottom of the microplate wells, the IncuCyte Zoom could track cell confluence. However, visual inspection of the micrographs suggests that the rate of cell proliferation was largely undisturbed, even in the presence of a large quantity of adjuvant. Alhydrogel and  $^{115}\text{In-AIO(OH)}$  at  $>125 \mu\text{g/mL}$  induced a level of cell death above untreated cell controls (Figure 2-13B).  $^{115}\text{In-AIO(OH)}$  at 500  $\mu\text{g/mL}$  resulted in more cell death compared to Alhydrogel after 6-10 hours of exposure, suggesting that the doped adjuvant may be more acutely toxic.

The MTT assay for cellular respiration showed a similar toxicity pattern between Alhydrogel and 2.5%  $^{115}\text{In-AIO(OH)}$  (Figure 2-13C).  $^{115}\text{In-AIO(OH)}$  was statistically more toxic than untreated cells above 15.6  $\mu\text{g/mL}$  while Alhydrogel showed reduced respiration only above 62.5  $\mu\text{g/mL}$ .

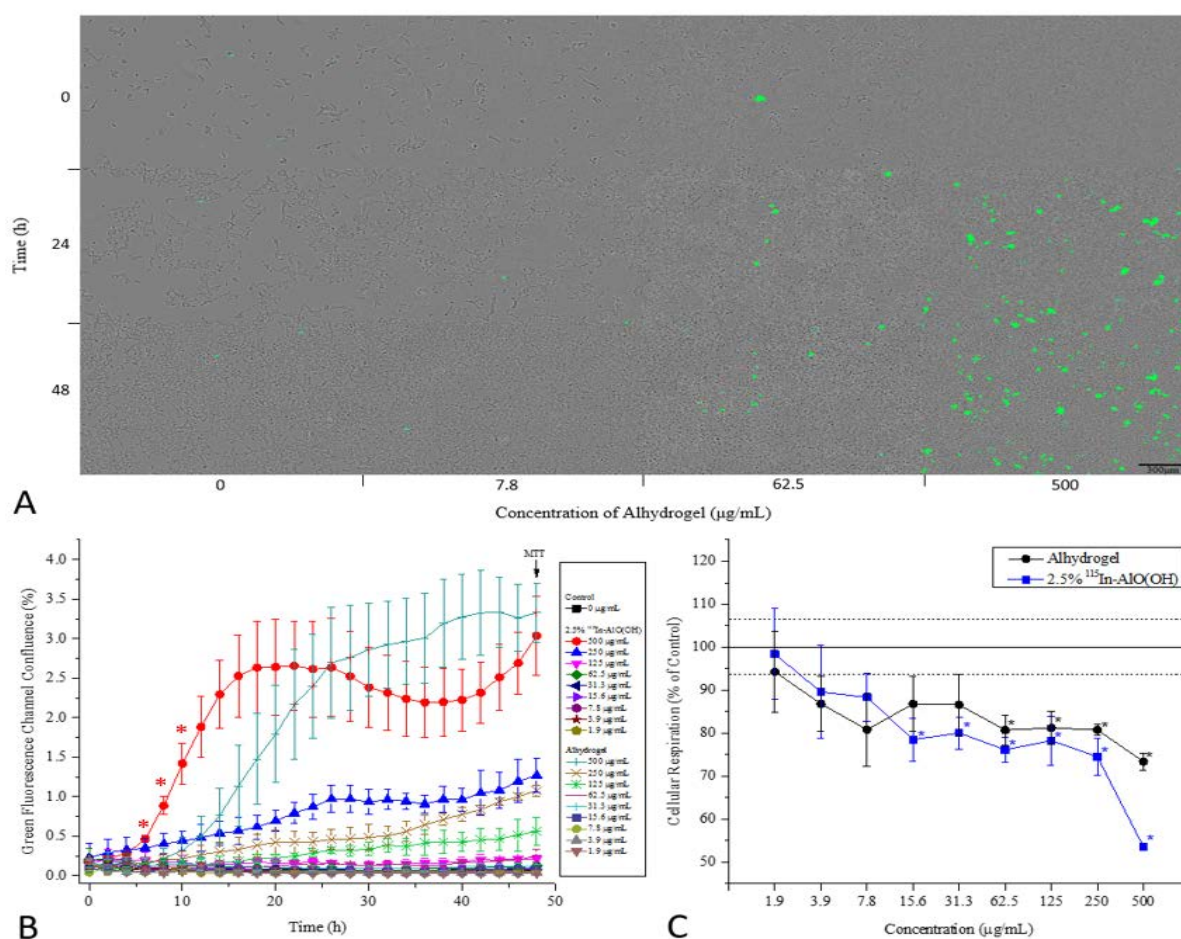


Figure 2- 14: Representative micrographs (A) and analysis of cell death over time (B) from the YOYO-1 toxicity assay. Both adjuvants caused statistically more cell death compared to untreated cells above 125  $\mu\text{g/mL}$ . Asterisks in panel B represent statistical differences between Alhydrogel and 2.5%  $^{115}\text{In-AIO(OH)}$  at a particular adjuvant concentration. MTT assay results for cellular respiration (C) after 48 hours of exposure to the adjuvants; an asterisks represent a statistical difference between the adjuvants and untreated cells.

2.3.9. Humoral and Cellular Immune Responses to  $^{111/115}\text{In-AIO(OH)}$  and Alhydrogel

Aluminum-based adjuvants promote humoral immunity and polarize  $\text{CD4}^+$  T-helper cells towards a Th2 phenotype (80). In mice, IgG1 and IgE are the antibody isotypes associated with a Th2-skewed immune response whereas IgG2c is associated with a Th1-polarized response (80). Figure 2-14 shows that  $^{111}\text{In-AIO(OH)}$  and 2.5%  $^{115}\text{In-AIO(OH)}$  increased total IgG and specifically promoted IgG1 over IgG2c against adsorbed OVA. These results suggest that the indium-doped adjuvants promotes a similar humoral response to published findings with Alhydrogel (80).

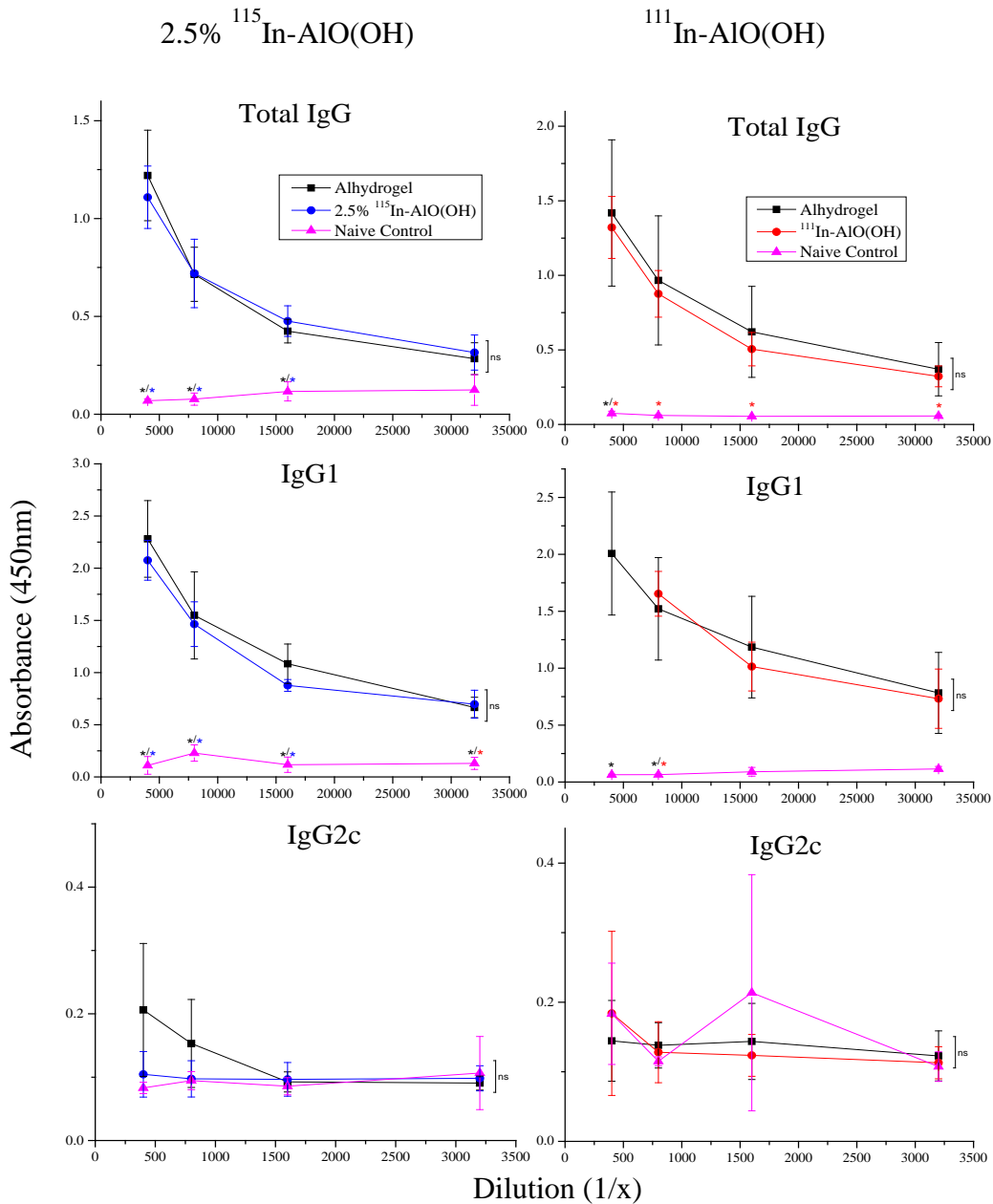


Figure 2- 15: Serum levels of anti-OVA total IgG, IgG1 and IgG2c in mice vaccinated with OVA adsorbed to either 2.5%  $^{115}\text{In-AIO(OH)}$  (left) or  $^{111}\text{In-AIO(OH)}$  (right). Each indium-doped adjuvant was compared to Alhydrogel and naïve control animals.

OVA-tetramer staining was used to assess the formation of cell-mediated immunity to OVA adsorbed to the indium-doped adjuvants and Alhydrogel. The top panels of Figure 2-15 illustrates the gating strategy used to determine the percentage of the CD8<sup>+</sup> T cells in the peripheral blood that are specific to the OVA antigen (74).

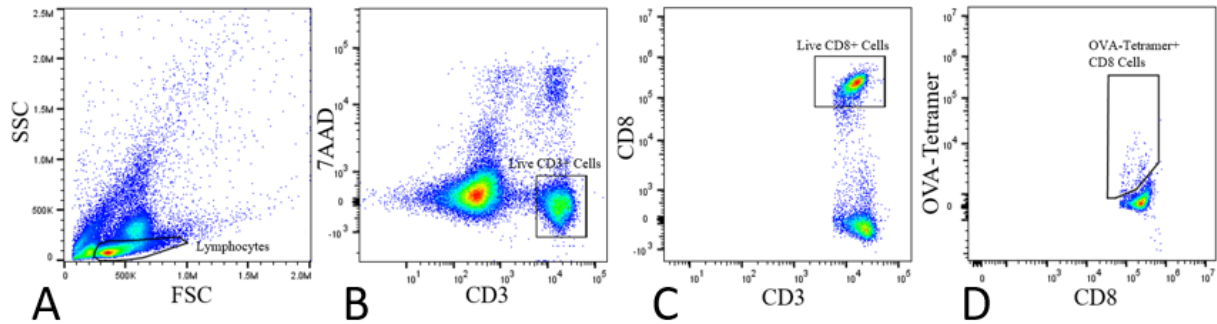


Figure 2- 16: Gating strategy for OVA-tetramer positive CD8<sup>+</sup> T-cells. After drawing a gate around the lymphocyte population (A), live CD3<sup>+</sup> T cells were selected as CD3<sup>hi</sup> 7AAD<sup>low</sup> events (B). CD8<sup>+</sup> T-cells were identified as CD3<sup>hi</sup> CD8<sup>hi</sup> events (C) and OVA-tetramer high events were selected from this population (D).

Alhydrogel, <sup>111</sup>In-AIO(OH) and 2.5% <sup>115</sup>In-AIO(OH) promoted a slight, but statistically significant increase in the number of OVA-tetramer<sup>+</sup> CD8<sup>+</sup> T cells compared to naïve animals (Figure 2-15E). There was no statistical difference between the doped and commercial adjuvants tested though.

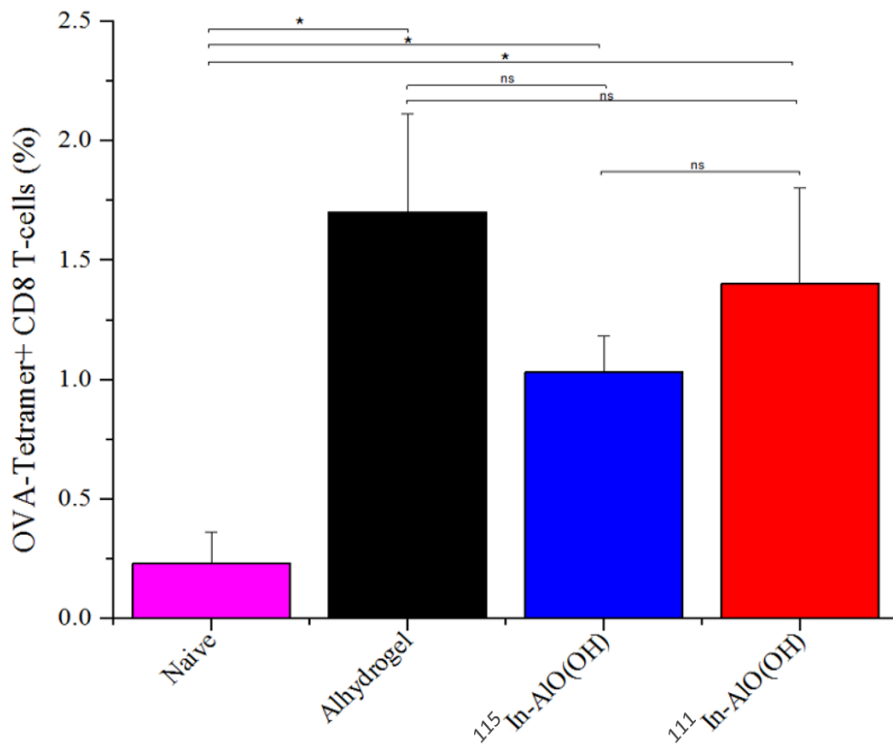


Figure 2- 17: Percentage of CD8<sup>+</sup> T-cells in peripheral blood that are positive for OVA-tetramer.

## 2.4. Discussion

ITLC and elemental mapping showed that the indium dopant was efficiently trapped and evenly dispersed within the AlO(OH) nanoparticles. Up to 5% of the aluminum atoms within the AlO(OH) matrix could be replaced by indium atoms without changing the adjuvant. An extensive array of physical and morphological assessments demonstrated that  $^{111/115}\text{In-AlO(OH)}$  closely match commercial Alhydrogel. The only physical difference observed between Alhydrogel and  $^{111/115}\text{In-AlO(OH)}$  was that the commercial adjuvant contained a small amount of  $\text{Al(OH)}_3$ . The transition from AlO(OH) to more crystalline  $\text{Al(OH)}_3$  is an energetically favorable process and would likely be observed if the doped-adjuvant was stored for a sufficient period of time. The batch of Alhydrogel analyzed was 18 months from the time of precipitation whereas most batches of  $^{111/115}\text{In-AlO(OH)}$  were analyzed and used within a few days of preparation.

Stability testing of  $^{111}\text{In-AlO(OH)}$  corroborates previous work by Seeber *et al.*, which showed that AlO(OH) dissolved poorly in physiological fluids (44). When Seeber and colleagues incubated Alhydrogel in a solution containing 100 times the physiological concentration of citric acid, a chelator that promotes adjuvant dissolution, only ~8% of the adjuvant dissolved after 5 days (44). A similar amount of  $^{111}\text{In-AlO(OH)}$  dissolved after 10-days in a high concentration of EDTA, another chelator that promotes dissolution (75, 76). The results of the stability test suggest that if the indium dopant is detected away from the site of injection, there is a high likelihood that it is in the form of a component nanoparticle.

The doped adjuvant had a similar toxicity profile to Alhydrogel, although 2.5%  $^{115}\text{In-AlO(OH)}$  may have been more acutely toxic. Aluminum-based adjuvants have been shown to induce cell death at the site of injection, leading to the release of genomic DNA and other DAMPs that in turn help to potentiate an immune response (26, 27). Eidi *et al.* previously used an MTT assay to assess the toxicity of Alhydrogel on NSC-34 neuron-like cells (53). Toxicity was observed at only 1  $\mu\text{g/mL}$  of Alhydrogel for the NSC-34 line compared to 62.5  $\mu\text{g/mL}$  with HEK293 cells used in this thesis (53). Future toxicity assessments should use more representative cell lines for the injection site (i.e., C2C12 myocytes or 3T3 fibroblasts) and cells of the innate immune system that are drawn to this location (i.e., RAW264.7 monocytes).

When used to vaccinate mice against the model antigen OVA,  $^{111/115}\text{In-AlO(OH)}$  promoted the formation of IgG1 over IgG2c antibodies suggesting that the adjuvant polarized naïve  $\text{CD4}^+$  Th cells towards a Th2 phenotype that is characteristic for Alhydrogel (80). The indium-doped adjuvants and Alhydrogel resulted in the clonal expansion of a small population of OVA-specific  $\text{CD8}^+$  T cells. Previous reports in the literature have shown that OVA adsorbed to Alhydrogel can be cross-presented by  $\text{CD8}^+$  dendritic cells to induce the activation and proliferation of OVA-specific  $\text{CD8}^+$  T cells (34, 81-83). However, these cells fail to differentiate into cytotoxic T cells (CTL), resulting in a weak cell-mediated response (34, 56, 81, 83). Only when Alhydrogel is incorporated into a mixed adjuvant system, like AS04 where the AlO(OH) surface is functionalized with a TLR4 ligand, is a robust cell-mediated immune response developed (56).

Overall,  $^{111}\text{In}$  and  $^{115}\text{In}$  were successfully incorporated into the  $\text{AlO}(\text{OH})$  crystal structure while maintaining the physical and functional properties of Alhydrogel. The doped-adjuvant can be used to better understand the commercial adjuvant's biodistribution using techniques like SPECT/CT (chapter 3) and mass cytometry (chapter 4).

## Chapter 3: Biodistribution of $^{111}\text{In-AIO(OH)}$

### 1.1. Introduction

The seminal study by Flarend *et al.* using  $\text{AlO(OH)}$  doped with the positron emitter  $^{26}\text{Al}$  helped to establish the safety profile of aluminum-based adjuvants by showing that serum aluminum levels are only marginally elevated post-injection and below toxic levels (50). Although this study was the first to explore  $\text{Alhydrogel}$ 's pharmacokinetics, it did not assess the amount of adjuvant at key immunological sites like the draining lymph node (50). This chapter uses  $^{111}\text{In-AIO(OH)}$  to confirm certain aspects and expand upon Flarend's work.

$^{111}\text{In}$  is a gamma-emitting isotope that is commercially produced for nuclear medicine applications (84). With a half-life of 2.8 days,  $^{111}\text{In-AIO(OH)}$  can be tracked over a period of  $\sim 2$  weeks (84). Compared to  $^{26}\text{Al-AIO(OH)}$  with a half-life of  $7.17 \times 10^5$  years,  $^{111}\text{In-AIO(OH)}$  is associated with fewer radiation safety issues (50, 84). To track  $^{111}\text{In-AIO(OH)}$  *in vivo*, single-photon emission computed tomography (SPECT) was used together with x-ray based computed tomography (CT) as an anatomical framework in this chapter (85). Compared to other imaging modalities (i.e., optical tomography, MR, etc...), SPECT/CT has amongst the highest sensitivity and is a fully quantitative technique; such a highly sensitive technique is required as only a small percentage of the administered adjuvant is expected to distribute from the site of injection (50, 84-88).

To further validate  $^{111}\text{In-AIO(OH)}$  as a useful tracer for  $\text{Alhydrogel}$ , the release rate of OVA antigen adsorbed to the adjuvant was assessed using SPECT/CT. For this purpose, OVA was modified with NOTA and radiolabeled with the gamma emitter  $^{67}\text{Ga}$ . The antigen was modified in this fashion due to the high *in vivo* stability of this chelation system and the similarity of this radioisotope's half-life (3.2 days) to  $^{111}\text{In}$  (75, 84, 89). Since  $^{67}\text{Ga}$  and  $^{111}\text{In}$  have never been imaged in a quantitative fashion together with SPECT, we developed new physics protocols to compensate for cross-talk between the isotopes. Cross-talk is the detection of photons originating from one radionuclide within the acquisition window of the other radioisotope (90). Figure 3-1 shows the spectrums of  $^{111}\text{In}$  and  $^{67}\text{Ga}$  for which the new reconstruction parameters were developed.

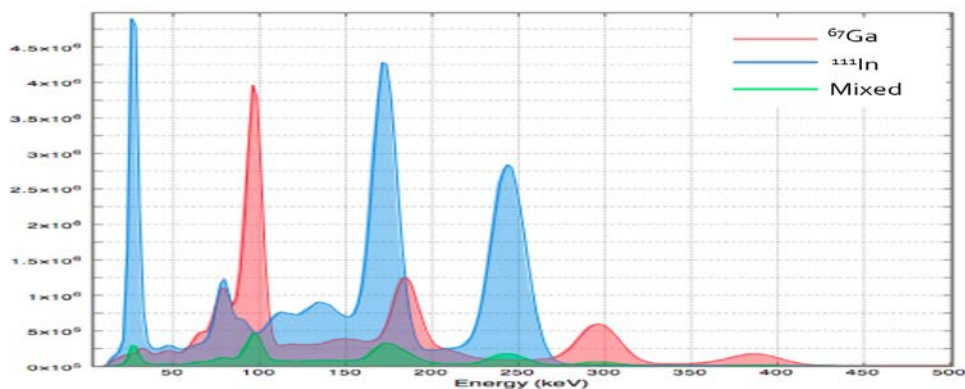


Figure 3- 1: Gamma spectra of  $^{67}\text{Ga}$  (red),  $^{111}\text{In}$  (blue) and mixed isotopes (green).

## 3.2. Materials and Methods

### 3.2.1. Synthesis and Radiolabeling of $^{67}\text{Ga}$ -NOTA-OVA

OVA protein at 20 mg/mL in sodium bicarbonate buffer (pH 8.5) was reacted overnight at 10°C with 2-S-(4-isothiocyanatobenzyl)-1,4,7-triazacyclononane-1,4,7-triacetic acid (p-SCN-Bn-NOTA; Macrocyclics B-605) at a stoichiometric ratio of 1:5 (91). The modified protein was isolated and buffer exchanged into 1xPBS using a 30 kDa MWCO micro-concentrator. To radiolabel the protein, 130 MBq of  $^{67}\text{GaCl}_3$  in 0.1N HCl (Nordion IPG-Ga-67) was added to 7.5 mg of NOTA-OVA at room temperature for 4 hours under light agitation (92). Excess activity was removed and the protein was buffer exchanged into saline using a 30 kDa MWCO micro-concentrator. The concentration of the radiolabeled antigen was determined using a fluorescamine assay, described previously, against a standard curve of NOTA-OVA.

### 3.2.2. Labeling Efficiency and Radiopurity Assessment of $^{67}\text{Ga}$ -NOTA-OVA

Thin layer chromatography (TLC) using a silica gel 60F<sub>254</sub> (Merck 1055540001) stationary phase and 0.1 M citric acid solution at pH 4 (Sigma 251275) mobile phase was used to assess the radiolabeling of NOTA-OVA (93). In this system,  $^{67}\text{Ga}$ -NOTA-OVA remains at  $R_f=0$  while free  $^{67}\text{Ga}$  forms a complex with the citric acid and migrates to  $R_f=1$  (93). TLCs were spotted with 1  $\mu\text{L}$  of  $^{67}\text{Ga}$ -NOTA-OVA before and after the removal of excess  $^{67}\text{Ga}$  to calculate the labeling efficiency and radiopurity, respectively. A photostimulable phosphor screen, Cyclone Phosphor Imager and OptiQuant software (Perkin Elmer) were used to analyze the TLC data, as described in chapter 1.

### 3.2.3. SDS and Native PAGE Analysis of $^{67}\text{Ga}$ -NOTA-OVA

A Mini-PROTEAN electrophoresis system (Bio-Rad) was used to cast 0.75mm thick native and SDS polyacrylamide gels. The resolving portion consisted of 10% 1:29 bis:acrylamide, 375 mM Tris at pH 8.8, 0.1% APS and 0.05% TEMED ( $\pm$  0.1% SDS) and was polymerize under a layer of isopropanol (94, 95). The stacking region consisted of 5% 1:29 bis:acrylamide, 125 mM Tris at pH 6.8, 0.1% APS and 0.05% TEMED ( $\pm$  0.1% SDS) (94, 95). All reagents for gel casting were obtained from Bio-Rad.

For SDS-PAGE, 10  $\mu\text{L}$  of modified or unmodified OVA solution (0.5-2mg/mL) was mixed with 2  $\mu\text{L}$  of 6x Laemelli sample buffer and heated at 95°C before being loaded onto the gel (95). For native PAGE analysis, 5  $\mu\text{L}$  of protein solution was mixed with an equal volume of 2x native sample buffer (Bio-Rad 1610738) and loaded directly onto the gel (94). The gels were run with constant current (15 mA) in a buffer contained 25 mM Tris and 192 mM glycine at pH 8.3 ( $\pm$  0.1% SDS) (Bio-Rad 1610771/2) until the indicator dye reached the bottom of the gel.

The gels were stained using a solution of 85 mM Coomassie brilliant blue dye (Sigma 27816) in 35mM HCl with the assistance of microwave irradiation (96). The gels were de-stained with 18 M $\Omega$  with the aid of heat (96). The gels were documented using an Odyssey CLx Imager (LiCor) measuring fluorescence in the 700 nm

channel. A photosimulable phosphor plate and Cyclone Phosphor Imager (Perkin Elmer) were used to assess the location of the radioactivity within the gel.

### 3.2.4. SPECT/CT Assessment of <sup>67</sup>Ga-NOTA-OVA Adsorbed to <sup>111</sup>In-AlO(OH) or Alhydrogel

C57BL/6 mice (n=4) between 6-8 weeks old were injected into the left posterior region on the dorsal surface with 200 µg (3.7 MBq) of <sup>67</sup>Ga-NOTA-OVA adsorbed to 0.7 mg (7.4 MBq) of <sup>111</sup>In-AlO(OH) in a total volume of 100 µL. The same group of animals received a contralateral injection containing 200 µg (3.7 MBq) of <sup>67</sup>Ga-NOTA-OVA adsorbed to 0.7 mg of Alhydrogel. A second group of mice (n=3) was administered on the dorsal surface 200 µg (3.7 MBq) of <sup>67</sup>Ga-NOTA-OVA as a free antigen control. The 2 groups of animals were serially scanned (whole body minus tail) in list-mode under isoflurane in a VECTor PET/SPECT/CT system (MILabs) outfitted with an extra-ultra-high sensitivity mouse collimator (MILabs) (97, 98). BioVet software (m2m Imaging) was used to monitor the vital signs of the animals during the scans and make appropriate adjustments to the anesthesia when necessary. The time and duration of each SPECT scan post-injection of the tracers are shown in Table 3-1. The duration of the SPECT scan was increased over time to generate better quality data/obtain more counts as the <sup>111</sup>In decayed. The CT scan was always 5 minutes in duration and followed the SPECT acquisition.

Time Post-Injection (hours)	SPECT Acquisition Duration (minutes)
0	30
5	30
24	30
120	60
240	90
360 (Terminal Scan)	120

Table 3- 1: SPECT scan times and durations.

CT data was reconstructed with a cone-beam filtered back-projection algorithm using NRecon software (Skyscan). The SPECT data was reconstructed from list-mode projection data using a pixel-based ordered subset expectation maximization (POSEM) algorithm with 6 iterations and 16 subsets with the voxel size defined as 0.4 mm<sup>3</sup> using U-SPECT Rec2.5li software (MILabs) (99). The photopeak widow to reconstruct <sup>67</sup>Ga was set at 96 ± 20 keV while <sup>111</sup>In was reconstructed at 243 ± 15 keV (unpublished data, Hafeli Lab). Scatter correction was performed using triple energy window methods with two 20% wide scatter windows adjacent to the reconstruction windows (100).

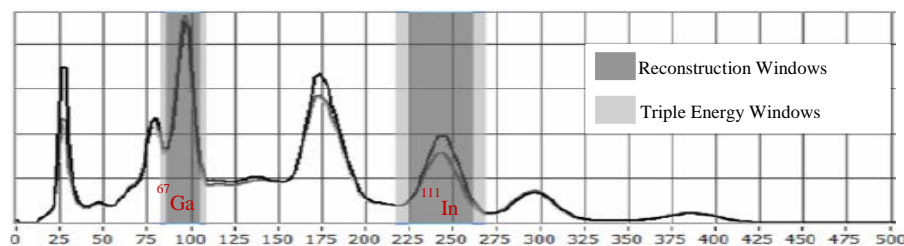


Figure 3- 2: Location of reconstruction and triple energy windows used to separate <sup>67</sup>Ga and <sup>111</sup>In signals in dual-isotope SPECT.

U-SPECT Rec2.5li software was also used to apply CT-based attenuation correction and isotope decay correction to all SPECT reconstructions and to automatically register the SPECT and CT images. AMIDE software (UCLA) was used to generate renderings of the data; a 3D-Gaussian filter was applied (0.5 mm FWHM) to reduce noise unless otherwise specified (101).

AMIDE software was also used to perform a volume of interest (VOI) analysis to assess the amount of  $^{111}\text{In-AIO(OH)}$  and  $^{67}\text{Ga-NOTA-OVA}$  remaining at the site of injection over time (101). Calibration factors ( $^{67}\text{Ga}$ : 1522 MBq/mL,  $^{111}\text{In}$ : 1244 MBq/mL) were applied to convert the arbitrary units from the VOI analysis into units of radioactivity (unpublished data, Hafeli Lab). The data from the VOI analysis was standardized to the time of administration and reported as a percentage of the injected activity versus time.

### 3.2.5. *Sacrifice-Based Biodistribution of $^{111}\text{In-AIO(OH)}$*

C57BL/6 mice (n=3) between 6-8 weeks old were injected into the posterior half of the dorsal surface with 100  $\mu\text{g}$  (~3.7 MBq) of OVA adsorbed to 0.7mg (7.4 MBq) of  $^{111}\text{In-AIO(OH)}$  in a total volume of 100  $\mu\text{L}$ . The animals were sacrificed 10-days post-administration to conduct a biodistribution study. Briefly, various organs and the site of injection were harvested, weighted and their activity determined using a Packard Cobra II gamma counter (92). Results were expressed as activity concentration (cpm/g), the percentage of the injected dose per organ (%ID/organ) and per gram of tissue (%ID/g) and as an organ-to-blood ratio (92).

### 3.2.6. *Data Analysis*

Data are presented as mean  $\pm$  standard deviation unless otherwise specified. GraphPad Prism 7 was used for statistical analysis using Student's t-test, linear regression or ANOVA followed by multiple comparisons testing (Dunnet's test).  $P < 0.05$  was considered statistically significant and was indicated by an asterisks (\*). Data was graphed using either GraphPad Prism 7 or OriginPro 9.

### 3.2.7. *Ethics Statement*

All animal experiments were carried out in accordance with the guidelines of the University of British Columbia's Animal Care Committee under the approved protocol A12-0172.

### 3.3.Results

#### 3.3.1. Preparation and Characterisation of $^{67}\text{Ga}$ -NOTA-OVA

TLC analysis showed that the labeling efficiency for  $^{67}\text{Ga}$ -NOTA-OVA, which remains at  $R_f=0$ , was  $84.5 \pm 4.3\%$  (Figure 3-3B). After purifying the radiolabeled antigen and removing free  $^{67}\text{Ga}$ , the radiopurity was calculated to be  $99.4 \pm 0.9\%$  (Figure 3-3C). The tracer was sufficiently pure for *in vivo* assessments.

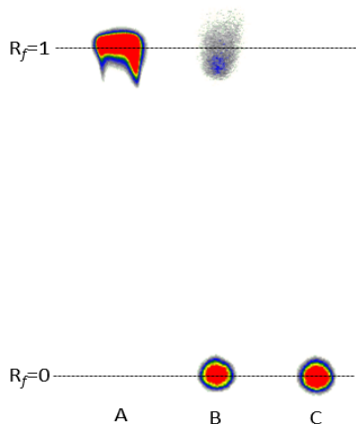


Figure 3- 3: Labeling efficiency (B) and radiopurity of  $^{67}\text{Ga}$ -NOTA-OVA (C) in relation to free  $\text{GaCl}_3$  (A).

SDS-PAGE analysis of NOTA-OVA and  $^{67}\text{Ga}$ -NOTA-OVA (Figure 3-4A) showed that the antigen had a similar molecular weight to the unmodified protein (44.3kDa) (102). No appreciable amount of degradation products were observed additionally. Native-PAGE analysis (Figure 3-4B) found that both NOTA-OVA and  $^{67}\text{Ga}$ -NOTA-OVA migrated further down the gel toward the cathode. This observation helps to confirm the conjugation of NOTA, as the added negative charge from the chelator reduced the isoelectric point of the antigen and improved its electrophoretic mobility. Native PAGE analysis showed no overt signs of aggregation in relation to the unmodified antigen. The location of the radioactivity matches the protein staining on the gel, confirming that the radiolabeling procedure was successful.

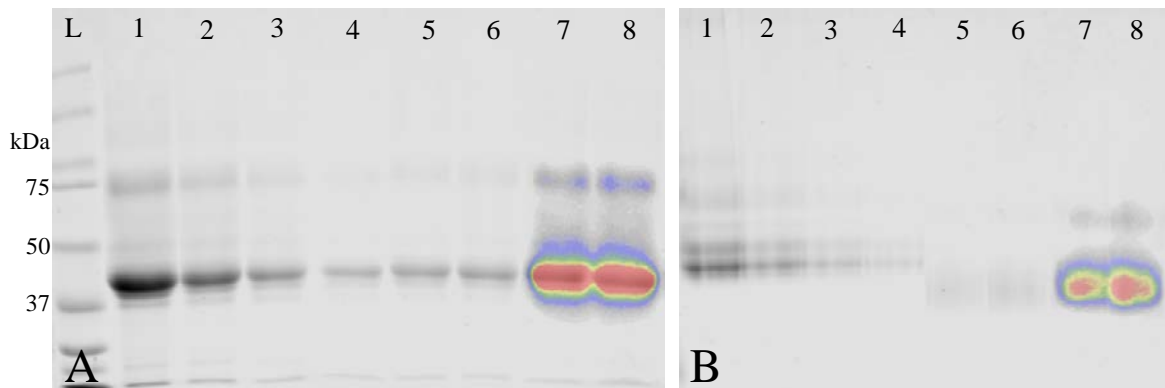


Figure 3- 4: 10% SDS PAGE (A) and native-PAGE (B) analysis of  $^{67}\text{Ga}$ -NOTA-OVA. The lanes are a molecular weight ladder (L), 2-0.25mg/mL calibration curve of unmodified OVA (1-4), OVA-NOTA (5-6) and  $^{67}\text{Ga}$ -NOTA-OVA (7-8). The Coomassie stain (gray scale) has been overlaid with a phosphorimage of the radioactivity within the gels (heat map).

### 3.3.2. Serial SPECT/CT Assessment of $^{111}\text{In-AIO(OH)}$ and $^{67}\text{Ga-NOTA-OVA}$ at the Injection Site

Using the SPECT reconstruction parameters described in section 3.2.4,  $^{111}\text{In}$  and  $^{67}\text{Ga}$  signals could be properly separated and independently quantified. Figure 3-5 helps to illustrate this point, since  $^{111}\text{In-AIO(OH)}$  can be distinguished from  $^{67}\text{Ga-NOTA-OVA}$  when injected into the same animal.

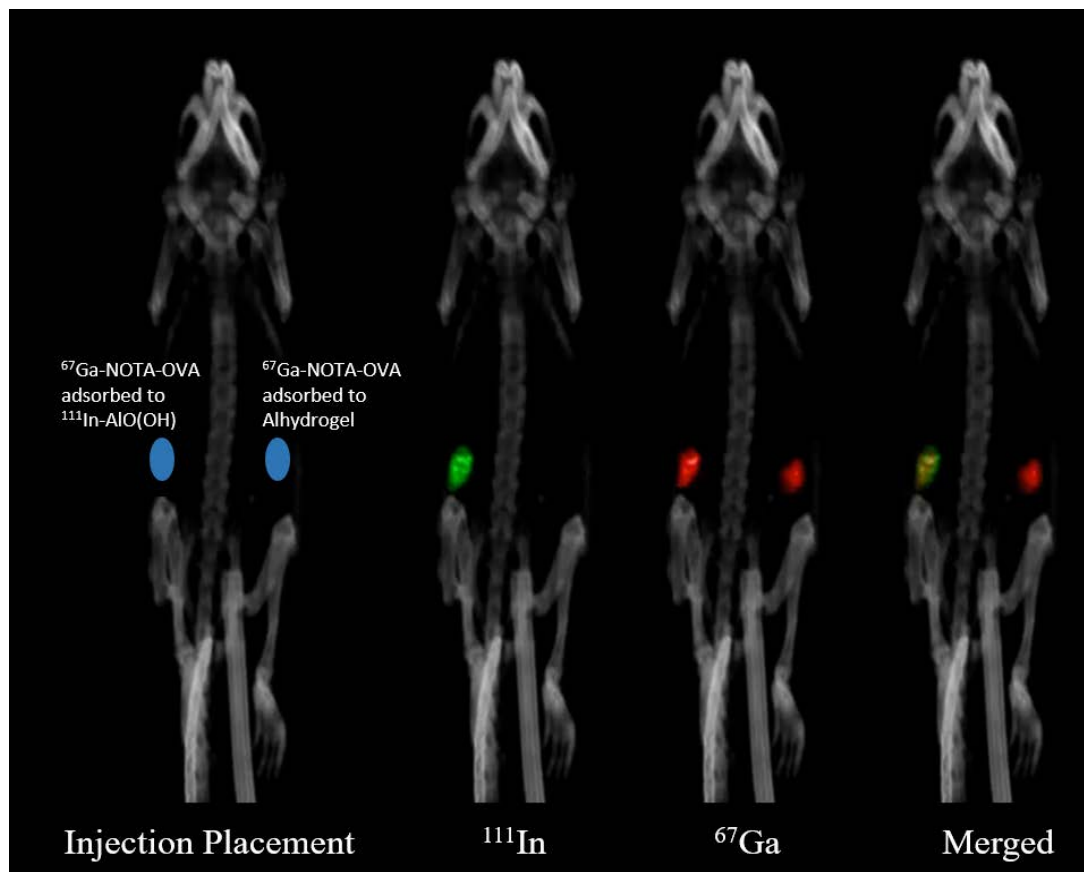


Figure 3- 5: Coronal view of a SPECT/CT scan taken immediately post-administration of the radiotracers. The leftmost panel illustrates that the mouse received an injection of  $^{67}\text{Ga-NOTA-OVA}$  adsorbed to  $^{111}\text{In-AIO(OH)}$  on the left flank and an injection of  $^{67}\text{Ga-NOTA-OVA}$  adsorbed to Alhydrogel on the right flank. The next 2 panels show the location of the  $^{111}\text{In}$  (green) and  $^{67}\text{Ga}$  (red) signal within the mouse. The rightmost panel is merged rendering of the  $^{111}\text{In}$  and  $^{67}\text{Ga}$  signals.

To help validate the  $^{111}\text{In-AIO(OH)}$  tracer, the kinetics of  $^{67}\text{Ga-NOTA-OVA}$  released from the doped adjuvant was compared to Alhydrogel *in vivo*. Figure 3-6A shows the location of the injection site VOIs used to perform the analysis. Both adjuvants retained  $^{67}\text{Ga-NOTA-OVA}$  for a longer duration at the site of injection when compared to the free antigen (Figure 3-7B). For example, at day 5 post-administration essentially no free antigen remained at the injection site compared to ~40% when adsorbed. This finding is in agreement with work by Noe *et al.*, who found that aluminum-based adjuvants delayed the drainage of  $^{111}\text{In-alpha-casein}$  from the region of administration (24). The release of  $^{67}\text{Ga-NOTA-OVA}$  from  $^{111}\text{In-AIO(OH)}$  was not statistically

different from Alhydrogel. Approximately 60% of the adsorbed  $^{67}\text{Ga}$ -NOTA-OVA was released from both adjuvants within the first 24 hours followed by a slower phase of release.

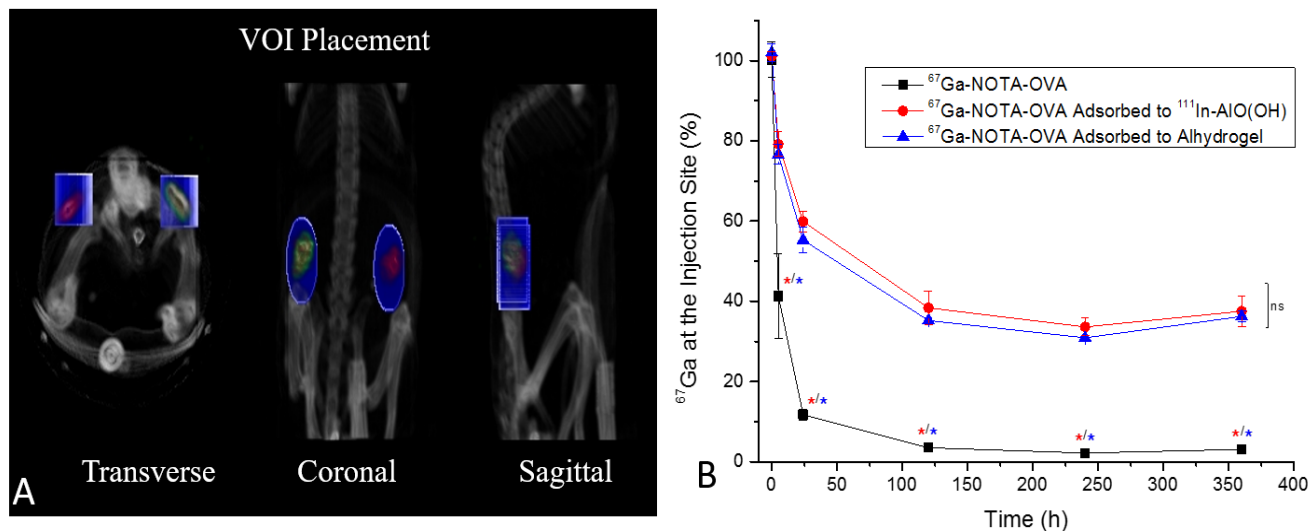


Figure 3- 6: Placement of the VOIs (blue regions) over the injection sites containing  $^{111}\text{In}$  (green) and or  $^{67}\text{Ga}$  (red) (A). Drainage of  $^{67}\text{Ga}$ -tagged antigen from the site of injection over time as free protein or when adsorbed to an aluminum-based adjuvant (B).

The VOI analysis of  $^{111}\text{In}$ -AIO(OH) showed that a small burst of  $^{111}\text{In}$  (~10%) was released from the site of injection within the first 24 hours post-administration followed by a slower phase (Figure 3-7). Approximately 20% less  $^{111}\text{In}$  was detected at the site of injection after 15 days. A linear regression through the data found that the slope of the line was significantly non-zero, adding confidence to the claim that the amount of radiotracer is decreasing from this location (Figure 3-7 Insert).

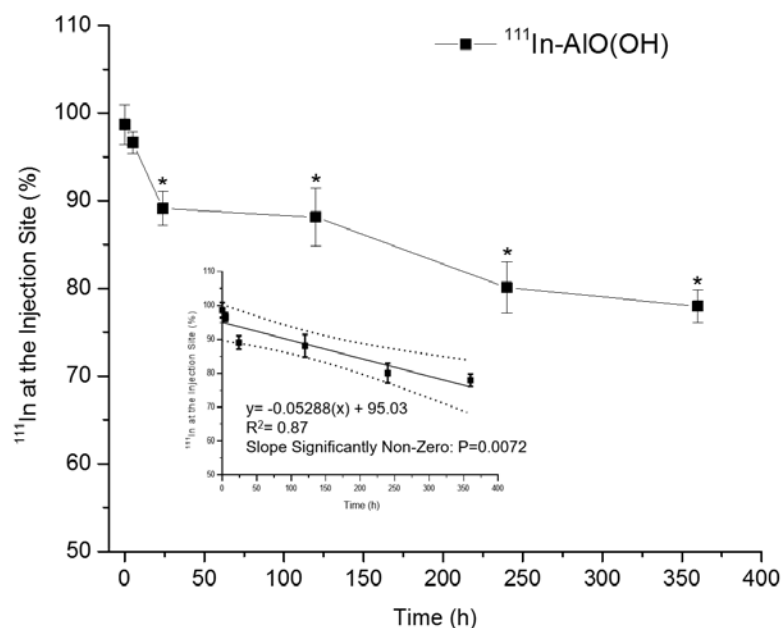


Figure 3- 7: VOI analysis of  $^{111}\text{In}$ -AIO(OH) from the site of injection. Asterisks designate a significant change at each time point in relation to the activity detected within the injection site VOI from the 0 hour post-injection scans. The graph insert shows a linear-regression through the data.

### 3.3.3. Sacrificed-Based Biodistribution of $^{111}\text{In-AIO}(\text{OH})$

Since the amount of  $^{111}\text{In}$  that distributed from the site of injection was rather low, quantification of the activity in the various organs was challenging using the SPECT/CT data. A group of animals was subsequently administered  $^{111}\text{In-AIO}(\text{OH})$  and sacrificed 10 days post-administration to determine the amount of activity in the organs with a gamma counter.

There was no statistical difference between the amount of activity measured at the injection site using SPECT/CT ( $88.1 \pm 3.3\%$ ) or a sacrifice-based biodistribution ( $87.0 \pm 2.1\%$ ) at day 10. This finding helps to validate the VOI analysis and the dual-isotope SPECT reconstruction parameters from section 3.3.2. The distribution of activity beyond the injection site is displayed in Figure 3.8.  $^{111}\text{In}$  was found predominantly in the inguinal draining lymph nodes, kidneys, liver, spleen, bone, bladder and muscle. Minimal amounts of activity were found within the blood, heart, lung, small intestines, pancreas, brain and excreted into the feces on day 10 post-injection. The distribution of  $^{111}\text{In}$  was similar to that observed by Hem's group using  $^{26}\text{Al-AIO}(\text{OH})$  (50)

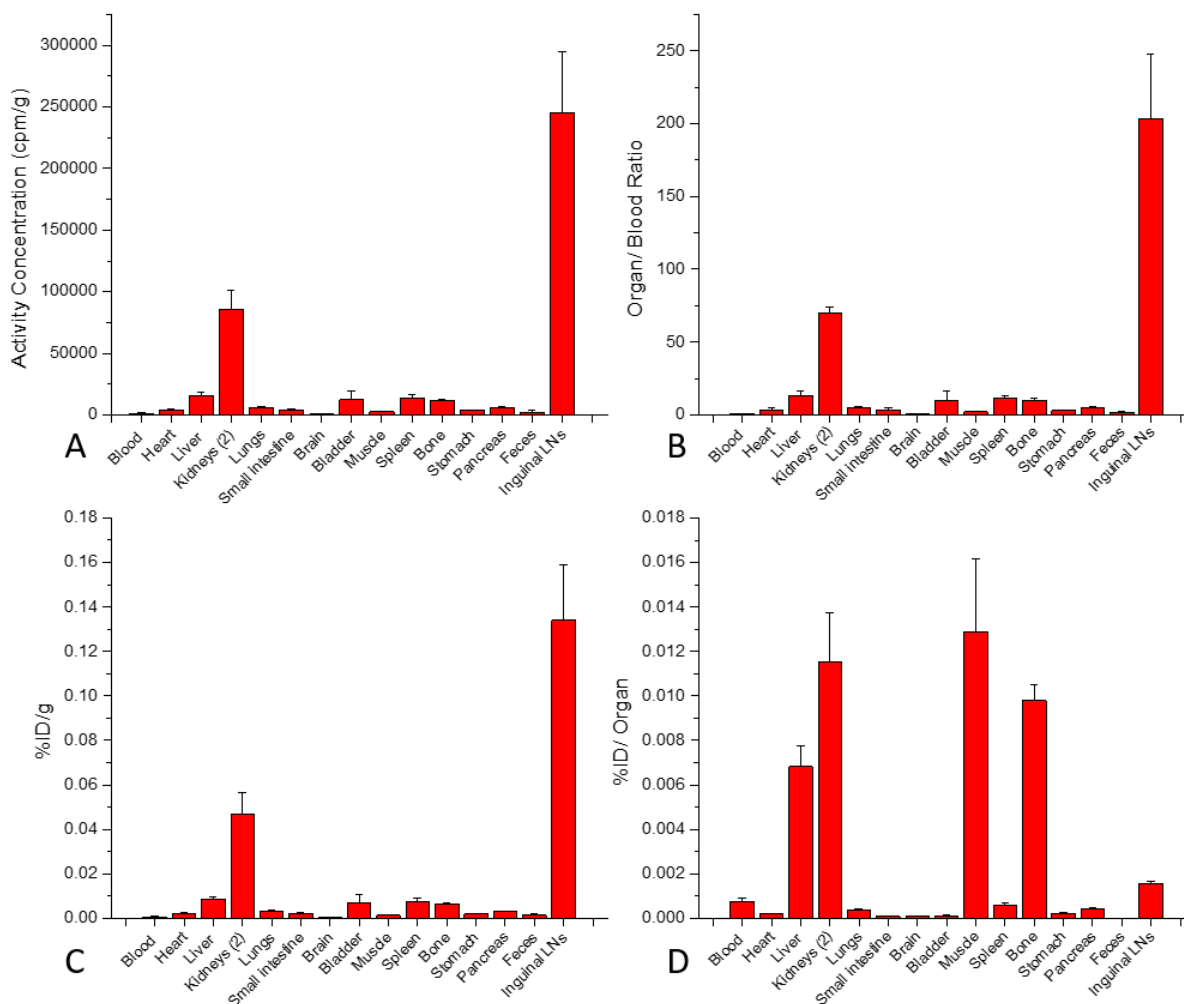


Figure 3- 8: Results of the biodistribution study presented as cpm/g (A), organ/blood ratio (B), %ID/g (C) and %ID/organ (D).

### 3.4. Discussion

This chapter presented the first dual-isotope SPECT scan using  $^{67}\text{Ga}$  and  $^{111}\text{In}$ . Reconstruction parameters were developed that effectively prevented isotope cross-talk, as illustrated in Figure 3-1. This technique could be applied to other imaging experiments or diagnostic procedures that require 2 gamma emitters with relatively long yet similar half-lives.

Compared to the free antigen,  $^{111}\text{In}$ -AIO(OH) and Alhydrogel formed a long-lasting depot of  $^{67}\text{Ga}$ -NOTA-OVA at the site of injection. Other investigations have also shown that aluminum-based adjuvants slow the drainage of adsorbed antigens from the injection site, which may be mechanistically important in the generation of an immune response (6, 20, 22, 24). There was no statistically significant difference between the release of  $^{67}\text{Ga}$ -NOTA-OVA adsorbed to  $^{111}\text{In}$ -AIO(OH) or Alhydrogel, which helps to further validate the indium-doped AIO(OH) strategy.  $^{67}\text{Ga}$ -NOTA-OVA was released from the doped and commercial adjuvant in a 2-phase manner: a burst phase where ~60% of the antigen drained from the site of injection over the first 24 hours followed by a slower phase of distribution. Noe *et al.* observed a similar release profile at the site of injection for  $^{111}\text{In}$ -alpha-casein adsorbed to Alhydrogel in mice (24). This dual-phase release is likely the result of partial antigen de-adsorption upon exposure to constituents in interstitial fluid (24, 57, 103). Results from the de-adsorption assay in section 2.3.7. of this thesis found that ~65% of the adsorbed OVA was released from the adjuvant's surface within 30 minutes of exposure to a biological fluid. Work out of Staneley Hem's group observed a similar degree of de-adsorption with OVA from Alhydrogel *in vitro* (57).

The SPECT/CT VOI analysis of  $^{111}\text{In}$ -AIO(OH) showed that ~20% of the administered  $^{111}\text{In}$  distributes from the site of injection by day 15. Flarend *et al.* estimated that ~17% of their  $^{26}\text{Al}$ -doped adjuvant had dissolved from the site of injection based on blood AUC data (50).  $^{111}\text{In}$ -AIO(OH) appeared to also distribute as a small initial burst (~10%) followed by a slower secondary phase. Flarend observed a similar phenomena, reporting that the amount of  $^{26}\text{Al}$  in the blood spiked over the first 48 hours post-administration followed by a low, steady level of  $^{26}\text{Al}$  in the circulation over the next 26 days (50). As shown in section 2.3.2. of this thesis and in work by Seeber *et al.*, AIO(OH) is poorly soluble in biological fluids with only ~1.5% of  $^{111}\text{In}$ -AIO(OH) dissolving after 10 days in FBS (44). Even highly favorable, non-physiological conditions (i.e., 0.1M EDTA) could only dissolve ~8% of  $^{111}\text{In}$ -AIO(OH) after 10 days (75, 76). These findings together question the assumption within the field that Alhydrogel particles remain at the site of injection and slowly dissolve over time (50, 51). The distribution of adjuvant nanoparticles may help to explain the pharmacokinetics of  $^{111}\text{In}$ -AIO(OH) and  $^{26}\text{Al}$ -AIO(OH), particularly the early burst phase. It is already known that Alhydrogel aggregates temporarily de-aggregate upon exposure to biological fluid as the adjuvant surface equilibrates with factors, such as phosphate ions and proteins, present in the new environment (47). De-aggregated AIO(OH) nanoparticles are an ideal size (~10 x 5.5 nm) to enter into afferent lymphatic vessels and distribute to distant tissues (48).

The biodistribution of  $^{26}\text{Al-AIO(OH)}$  and  $^{111}\text{In-AIO(OH)}$  both showed a high concentration of the radiotracer within the kidney, liver and spleen as well as a negligible amount of activity in the brain (50). The  $^{111}\text{In}$  tracer was also found at higher levels within sites not assessed by Flarend *et al.*, like the draining inguinal lymph nodes and bone. Unfortunately, the biodistribution profiles observed with  $^{26}\text{Al-AIO(OH)}$  and  $^{111}\text{In-AIO(OH)}$  can both be explained from the context of nanoparticle associated or soluble radionuclide. For example, free indium forms a complex with transferrin *in vivo* that traffics the radiometal to the liver (75). As part of the reticuloendothelial system, the liver also is highly efficient at clearing nanomaterials, such as  $^{111}\text{In-AIO(OH)}$ , from the blood (104). Kidney uptake may be due to the clearance of the solubilized radiometals or the filtration of adjuvant particles <5nm in diameter, which are below the size cut-off for the glomerulus (104). Bone marrow has been shown to take up both  $^{111}\text{In-transferrin}$  and nanomaterials efficiently (104, 105). The results obtained with  $^{111}\text{In-AIO(OH)}$  helped to identify which tissues to assess with techniques that can determine if the adjuvant is in nanoparticle form, such as mass cytometry (chapter 4) and STEM imaging (chapter 5).

One of the limitations with  $^{111}\text{In-AIO(OH)}$  is that the adjuvant could only be tracked for ~2 weeks before the radionuclide decayed to too great of an extent to be accurately quantified. Appendix 1 discusses options for the development of a longer-lasting traceable forms of Alhydrogel, such as MR-responsive Gd-AIO(OH).

## Chapter 4: Distribution of $^{115}\text{In-AIO(OH)}$ Particles in the Lymph Node

### 4.1. Introduction

White *et al.* and Giusti *et al.* have both reported structures that resemble preformed aluminum particles in the draining lymph node within 24 hours of administration (52, 54). Khan *et al.* found surrogate nanomaterials within the draining lymph node by day 1 post-injection that peaked by day 4 (45). Using nanodiamond-functionalized Alhydrogel, Eidi *et al.* observed  $2552 \pm 22$  fluorescent structures within thin sections of the draining lymph node on day 7 and  $308 \pm 22$  events on day 21 post-administration (53). Although there are limitations with the above studies, as outlined in chapter 2, they provide some preliminary evidence that Alhydrogel particles can distribute to the draining lymph node. Data from this thesis, namely the initial burst phase of  $^{111}\text{In}$  from the site of injection despite the poor solubility of  $^{111}\text{In-AIO(OH)}$ , supports the hypothesis that a portion of the adjuvant distributes in particulate form. The high concentration of  $^{111}\text{In}$  observed within the draining lymph node on day 10 post-administration of  $^{111}\text{In-AIO(OH)}$  further suggests that this site is appropriate to investigate for adjuvant in particle form.

A technique using mass cytometry by time of flight (CyTOF) and indium-doped AIO(OH) was developed in this chapter to identify aluminum-based adjuvants within the draining lymph node. CyTOF is a rather new technique that combines the cellular analysis principle of fluorescent-based flow cytometry with the selectivity and quantitative power of ICP-MS (106). CyTOF replaces the fluorescent markers used in flow cytometry with metal isotopes having a molecular weight of  $>80$  g/mol (106). For this project, the lumogallion stain for Alhydrogel was replaced with 2.5%  $^{115}\text{In-AIO(OH)}$ . Due to minimal spill over between isotopes, mass cytometry can analyze  $>50$  cellular parameters with little to no compensation (106). The indium doped adjuvant when coupled with mass cytometry overcomes one of the primary drawbacks with lumogallion, significant spectral overlap with other fluorophores that limits multi-parameter assessments (53, 58).

Researchers to date have only used the CyTOF technique for its original intended purpose of high dimensional immunophenotyping (107). This chapter uses mass cytometry for the first time for a different application, to evaluate the kinetics and cellular distribution of a heavy-metal tagged nanomaterials *in vivo*.

## 4.2. Materials and Methods

### 4.2.1. Animal Immunizations and Tissue Preparation

C57BL/6 mice between 6-8 weeks of age were injected into the posterior region of the dorsal surface with 100 µg of OVA adsorbed to 0.7 mg of 2.5% <sup>115</sup>In-AIO(OH) in a total volume of 100 µL. At set time points (1, 5, 10, 15, 40 and 70 days), 3 immunized mice and a naïve control were sacrificed by CO<sub>2</sub> asphyxiation under anesthesia with isoflurane. The inguinal lymph nodes were excised and pressed through a 70 µm cell strainer (Fisher 352350) to form a single-cell suspension and rinsed with CyFACS buffer (1% BSA in 1x PBS) (108). 1x10<sup>7</sup> cells from each sample were transferred to a 96-well plate for staining.

### 4.2.2. CyTOF Staining and Analysis

The collected cells were Fc blocked using tissue culture supernatant from a 2.4G2 hybridoma for 15 minutes on ice (74). The cells were then stained with the antibody cocktail described in Table 4-1 for 30 minutes at room temperature:

Antibody/ Probe	Clone	Metal Tag	Dilution	Vendor	Catalogue Number
CD45	30-F11	<sup>147</sup> Sm	1/100	Fluidigm	3147003B
CD3e	145-2C11	<sup>152</sup> Sm			3152004B
CD19	6D5	<sup>166</sup> Er			3166015B
CD11c	N418	<sup>162</sup> Dy			3162017B
CD11b	M1/70	<sup>148</sup> Nd			3148003B
Gr-1	RB6-8C5	<sup>141</sup> Pr			3141005B
NK1.1	PK136	<sup>170</sup> Er			3170002B
F4/80	BM8	<sup>159</sup> Tb			3159009B
CD86	GL1	<sup>172</sup> Yb			3172016B
MHCII	M5/114.15.2	<sup>174</sup> Yb			3174003B

Table 4- 1: CyTOF antibody panel.

After washing the cells with 150 µL of CyFACS buffer, they were re-suspended in 100 µL of 1xPBS and 100 µL of 5 µM cisplatin (Fluidigm 201064) was then added to the cells for 5 minutes at room temperature (109). The reaction was quenched with the addition of 100 µL of CyFACS buffer (109). After washing the cells with 200 µL of CyFACS buffer, they were re-suspended in 250 µL of 0.125 µM <sup>191/193</sup>Ir intercalator (Fluidigm 201192B) in fixation/permeation buffer (Fluidigm 201067) for 1 hour at room temperature (110). The cells were washed once with 300 µL of CyFACS buffer and re-suspended in 500 µL of CyFACS for transport to the CyTOF instrument on ice.

Within 1 hour of running the samples through the CyTOF, the cells were pelleted and re-suspended in 500 µL of 18 MΩ water to minimize cell loss due to osmotic lysis. Approximately 0.75x10<sup>6</sup> cells were then diluted to a volume of 600 µL with 18 MΩ water and 60 µL of 1x 4-metal calibration beads (Fluidigm 201078) was added to each sample. The cells were passed through a 40 µm strainer (Fisher 352340) before being injected

into a 500  $\mu\text{L}$  sample loop of a CyTOF 2 mass cytometer (Fluidigm) at a flow rate of 45  $\mu\text{L}/\text{min}$ . A minimum of 250,000 events were collected for each sample.

To account for minor changes in the sensitivity of the instrument between days, the data was normalized against the  $^{151/153}\text{Eu}$  calibration beads using software developed by the Nolan Lab at Stanford (111). The normalized data was analyzed using FlowJo V10 software (TreeStar).

#### 4.2.3. *Establishing a Gating Strategy for 2.5% $^{115}\text{In-AIO(OH)}$*

To determine how to properly gate for 2.5%  $^{115}\text{In-AIO(OH)}$  particles, 0.1  $\mu\text{L}$  of the adjuvant was stained as described above and injected alone into the mass cytometer. Although AIO(OH) is rather resistant to dissolution in biological fluids, controls were carried out to assess how 2.5%  $^{115}\text{In-AIO(OH)}$  and free  $^{115}\text{In}$  are taken up or bind to cells. This was assessed by incubating cells isolated from the inguinal lymph node of a naïve animal with 0.1  $\mu\text{L}$  of 2.5%  $^{115}\text{In-AIO(OH)}$  or an equivalent amount of free  $^{115}\text{In}$  (as  $^{115}\text{In-citrate}$ ) before staining and injection into the CyTOF. Data was normalized and analysed as described above.

#### 4.2.4. *Statistical Analysis*

Data are presented as mean  $\pm$  standard deviation unless otherwise specified. GraphPad Prism 7 was used for statistical analysis using Student's t-test.  $P < 0.05$  was considered statistically significant and was indicated by an asterisks (\*). Data was graphed using either GraphPad Prism 7 or OriginPro 9.

#### 4.2.5. *Ethics Statement*

All animal experiments were carried out in accordance with the guidelines of the University of British Columbia's Animal Care Committee under the approved protocol A14-0159.

### 4.3. Results

#### 4.3.1. Gating Strategy for 2.5% $^{115}\text{In}$ -AlO(OH) Particles

When 2.5%  $^{115}\text{In}$ -AlO(OH) was injected into the mass cytometer, the majority of the  $^{115}\text{In}$  events were within the 4-log dynamic range of the instrument (Figure 4-1A). 2.5%  $^{115}\text{In}$  is therefore an appropriate concentration of dopant for downstream *in vivo* assessments. The threshold for an  $^{115}\text{In}$ -positive event for all future analyses was set at  $>10^{1.1}$ .

The indium-doped particles stained in a unique way such that they can be easily distinguished from cellular events. First, 2.5%  $^{115}\text{In}$ -AlO(OH) was poorly stained by the  $^{191/193}\text{Ir}$  intercalator, a compound used to label DNA to identify cellular events and distinguish singlets from doublets (Figure 4-1B) (110). Cisplatin ( $^{195}\text{Pt}$ ) is used as a viability marker in mass cytometry since this chemotherapeutic preferentially enters cells with a compromised membrane and reacts with protein nucleophiles (109). Since 2.5%  $^{115}\text{In}$ -AlO(OH) readily adsorbs proteins, it is not surprising that the adjuvant stained high for  $^{195}\text{Pt}$  (Figure 4-1C). The BSA within the CyFACS buffer effectively blocked the adsorption of the metalated antibodies to the surface of the adjuvant. These antibodies are used to bind cell makers, such as CD45 and MHCII, to identify cell populations and assess the functional status of the cells (Figure 4-1D). Extracellular 2.5%  $^{115}\text{In}$ -AlO(OH) nanoparticles are therefore defined as  $^{115}\text{In}^{\text{hi}}$ ,  $^{191/193}\text{Ir}^{\text{lo}}$ ,  $^{195}\text{Pt}^{\text{hi}}$ , phenotypic marker $^{\text{lo}}$  events. Live cells on the other hand stain quite differently as  $^{191/193}\text{Ir}^{\text{hi}}$ ,  $^{195}\text{Pt}^{\text{lo}}$ , phenotypic marker $^{\text{hi}}$  events.

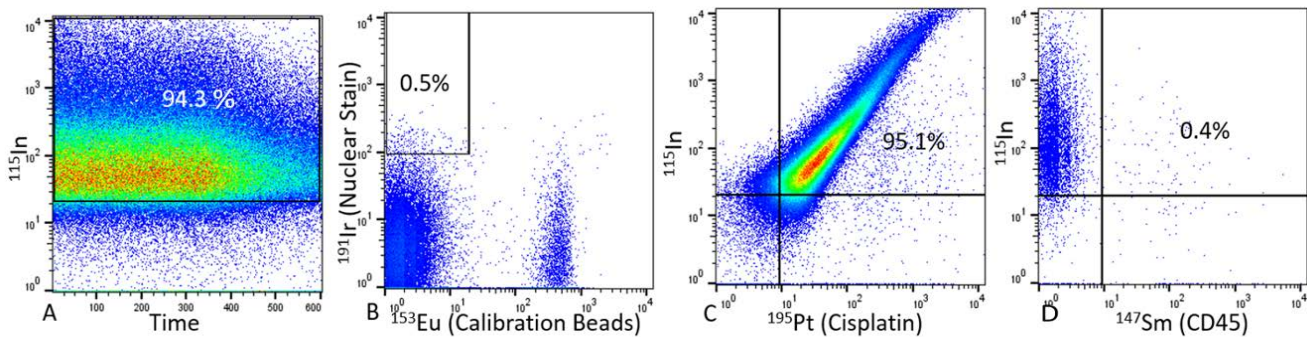


Figure 4- 1: CyTOF staining and gating strategy for non-cell associated 2.5%  $^{115}\text{In}$ -AlO(OH) adjuvant. With 2.5% of the aluminum atoms replaced with  $^{115}\text{In}$ , the adjuvant particles fell within the dynamic range of the mass cytometer (A). The adjuvant bound poorly to  $^{191}\text{Ir}$  nuclear stain (B), strongly to cisplatin (C) and poorly to metalated antibodies (D)

#### 4.3.2. Cells Treated with Free $^{115}\text{In}$ or 2.5% $^{115}\text{In}$ -AlO(OH) can be Distinguished

Cells isolated from the inguinal lymph node of a naïve mouse were incubated briefly with 2.5%  $^{115}\text{In}$ -AlO(OH) or free  $^{115}\text{In}$ , in the form of  $^{115}\text{In}$ -citrate, to assess how to gate for the metal dopant within a nanoparticle or solubilized state. As discussed in the above section, non-cellular 2.5%  $^{115}\text{In}$ -AlO(OH) can be identified as a distinct population (Figure 4-2A). Exposure of cells to soluble  $^{115}\text{In}$  found few events within the

2.5%  $^{115}\text{In-AIO(OH)}$  nanoparticle gate (Figure 4-2B). This observation adds confidence in the specificity of the gating strategy outlined in section 4.3.2 for cell unassociated nanoparticles.

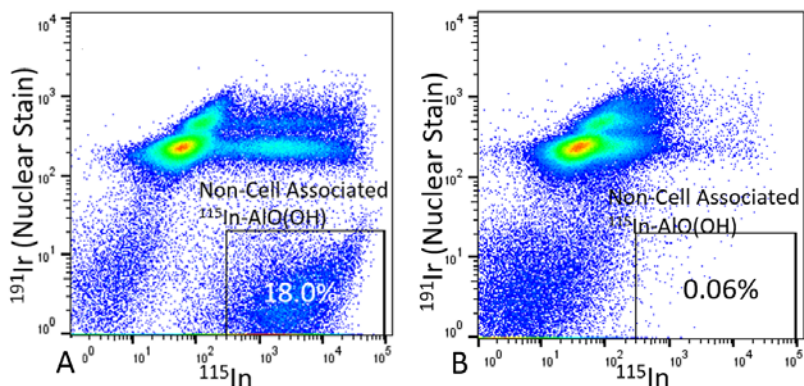


Figure 4- 2:  $^{191}\text{Ir}$  nuclear stain versus  $^{115}\text{In}$  in living cells incubated with 2.5%  $^{115}\text{In-AIO(OH)}$  (A) or  $^{115}\text{In-citrate}$  (B).

Cellular events ( $^{191/193}\text{Ir}^{\text{hi}}$ ) positive for  $^{115}\text{In}$  were observed in the both the samples treated with 2.5%  $^{115}\text{In-AIO(OH)}$  and  $^{115}\text{In-citrate}$ . Without an equivalent to side scatter in flow cytometers, CyTOF cannot distinguish whether the adjuvant particles are extracellularly associated or internalized into a cell (112). Free  $^{115}\text{In}$  has been shown to form complexes with various proteins, such as transferrin and albumin, which helps to explain how the free metal labels cells (113). Subsequently,  $^{191/193}\text{Ir}^{\text{hi}}$   $^{115}\text{In}^{\text{hi}}$  events represent cells with either extracellularly bound indium-doped AIO(OH) nanoparticles, internalized nanoparticles or protein-bound  $^{115}\text{In}$  released from adjuvant that has dissolved.

#### 4.3.3. Levels of $^{115}\text{In}$ within the Inguinal Lymph Node of Naïve Mice

Since  $^{115}\text{In}$  is a rather rare element, it is not surprising that naïve mice do not have many  $^{115}\text{In}$ -positive events within the draining lymph node. On average, control mice had  $0.0056 \pm 0.0008$  % total indium events in the draining lymph node and no  $^{115}\text{In}$ -positive cellular events were observed.  $^{115}\text{In}$ -positive events found in the lymph node of mice treated with 2.5%  $^{115}\text{In-AIO(OH)}$  can therefore be attributed to the adjuvant itself.

#### 4.3.4. Kinetics of $^{115}\text{In-AIO(OH)}$ within the Draining Lymph Node

Figure 4-4A illustrates the kinetics of total  $^{115}\text{In}$ -positive events and non-cell associated  $^{115}\text{In-AIO(OH)}$  nanoparticles within the draining lymph node;  $^{115}\text{In}$  was elevated significantly elevated when naïve animals at all time points, with the exception of day 5. Representative plots for day 15 post-injection showed that 4.2% of the total events in the lymph node are  $^{115}\text{In}$ -positive (Figure 4-4B). Nearly 2% of the events within the lymph node cell unassociated 2.5%  $^{115}\text{In-AIO(OH)}$  nanoparticles (Figure 4-4C). Examination of the nanoparticle population

confirmed that these events were stained with cisplatin and poorly labeled with phenotypic markers (Figure 4-4D and E).

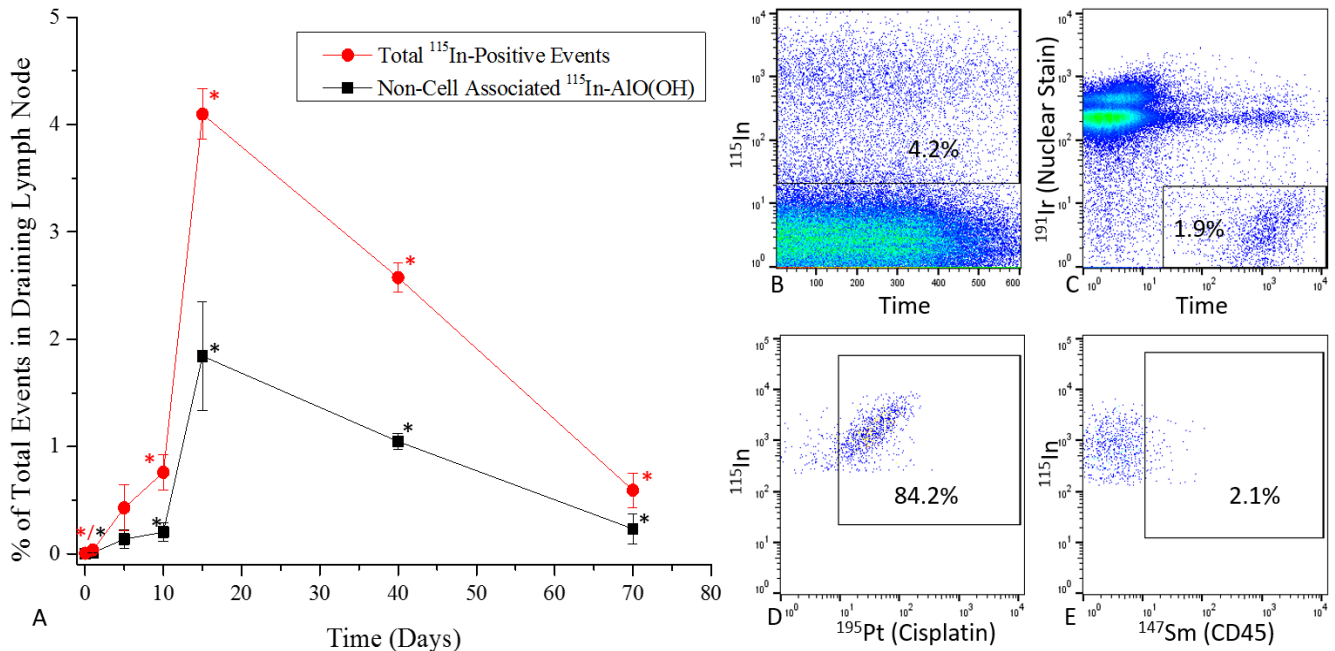


Figure 4-3: Kinetics of total <sup>115</sup>In-positive events and non-cell associated <sup>115</sup>In-AIO(OH) nanoparticles within the draining lymph node (A). Representative plots showing the gating for total <sup>115</sup>In-positive events (B) and cell-free <sup>115</sup>In-AIO(OH) nanoparticles (C). The cell-free particles were cisplatin positive (D) and phenotypic marker negative (E).

<sup>115</sup>In-positive events appeared within the draining lymph node within 1 day, peak at 15 days and slowly clear from that point onward. Cell unassociated 2.5% <sup>115</sup>In-AIO(OH) nanoparticles represent on average  $33.9 \pm 10.1$  % of the total <sup>111</sup>In events within the lymph node. The fact that the AIO(OH) dissolves poorly *in vivo* and the presence of a significant population within the cell-free nanoparticle gate suggests that a portion of the <sup>115</sup>In-positive cellular events are likely adjuvant nanoparticles.

#### 4.3.5. Cellular Distribution of <sup>115</sup>In-AIO(OH) within the Draining Lymph Node

Table 4-2 lists the phenotypic markers used to define various cellular populations within the draining lymph node (15, 114, 115). Figure 4-5 outlines the gating strategy used to assess the fraction of each cell population that were positive for the <sup>115</sup>In tracer.

Cell Population	Phenotypic Markers
T cells	CD45+, CD3+, CD19-
B cells	CD45+, CD19+, CD3-
Natural Killer (NK)	CD45+, CD3-, CD19-, NK1.1+
Dendritic cells (DC)	CD45+, CD3-, CD19-, NK1.1-, CD11c+, CD11b+/-
Macrophages	CD45+, CD3-, CD19-, NK1.1-, F480+, CD11b+/-
Granulocytes	CD45+, CD3-, CD19-, NK1.1-, CD11b+, Gr1+

Table 4- 2: Definition of cell populations for the CyTOF analysis.

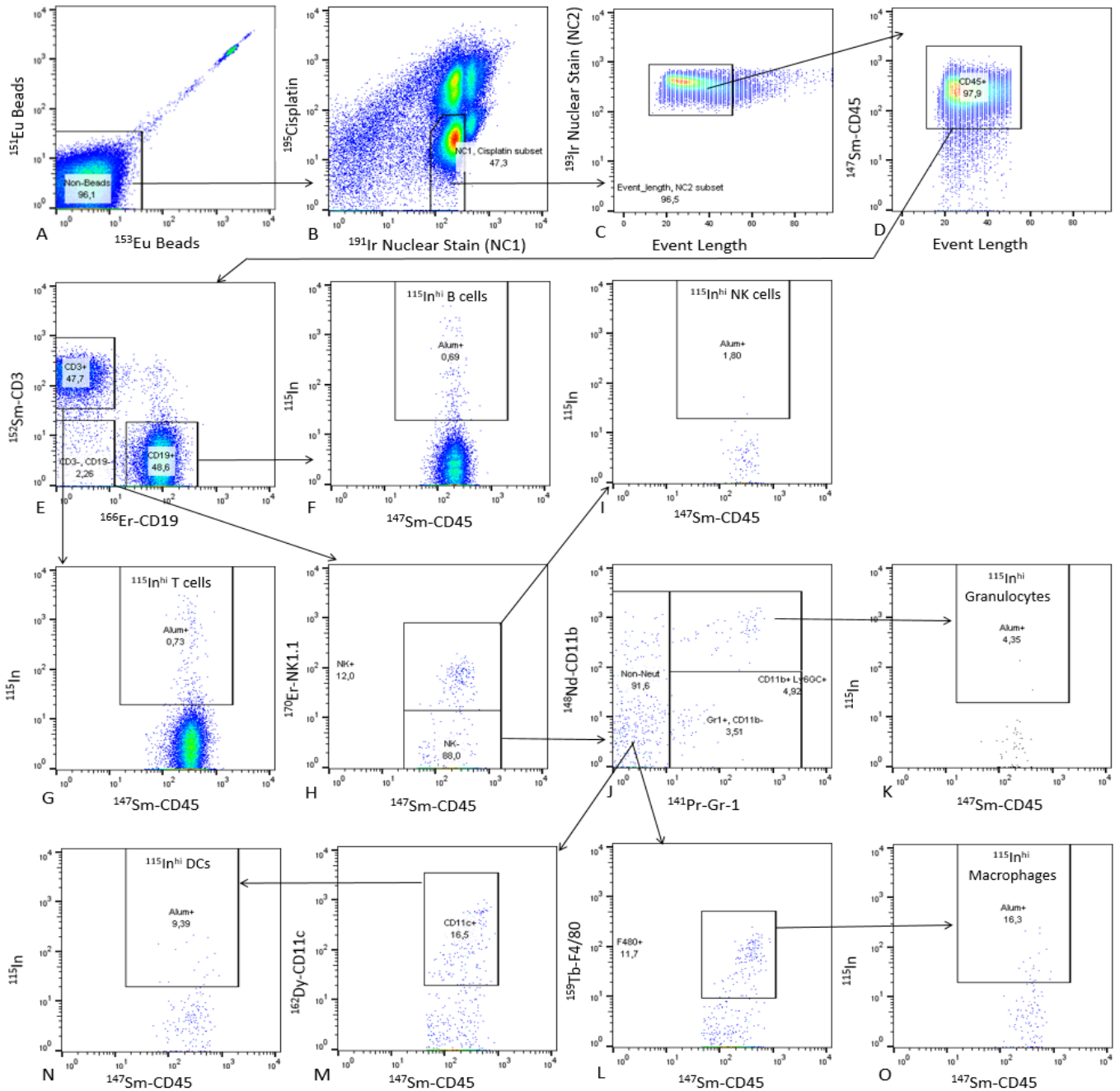


Figure 4- 4: Gating strategy to assess the phenotype of  $^{115}\text{In}$ -positive cellular events. Non-calibration beads were initially selected (A) followed by live singlets (B and C).  $\text{CD}45^+$  events representing pan-leukocytes (D) were divided into  $\text{CD}3^+$ ,  $\text{CD}19^+$  and  $\text{CD}3^-/\text{CD}19^-$  populations (E).  $^{115}\text{In}$ -positive B cells (F) and T cells (G) were then selected. NK cells were identified from the  $\text{CD}3^-/\text{CD}19^-$  population (H) its  $^{115}\text{In}$ -positive subset (I). Non-NK cells were divided based on their expression of  $\text{CD}11\text{b}$  and Gr-1 (J) and  $^{115}\text{In}$ -positive granulocytes were identified (K). Non-granulocytes with were divided into macrophages (L) and dendritic cells (M);  $^{115}\text{In}$ -high regions were selected from these populations (N and O).

Figures 4-6A and B show that there was a statistically significant increase in the number of B cells, dendritic cells, macrophages and total cell count within the draining lymph nodes 10 days post-administration of 2.5%  $^{115}\text{In-AIO}(\text{OH})$ . Previous reports have observed a similar changes in animals administered an aluminum-based adjuvant (52).

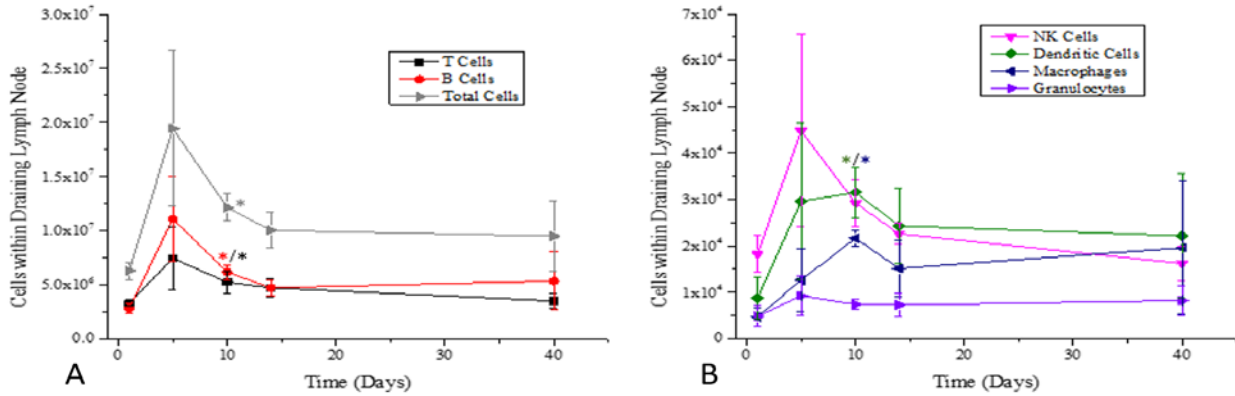


Figure 4- 5: Changes in the number of total cells, T cells and B cells (A) along with NK cells, DCs, macrophages and granulocytes (B) in the draining lymph node over time. An asterisks indicates a significant change in the size of the cell population in relation to naïve mice not treated with 2.5%  $^{115}\text{In-AIO}(\text{OH})$ .

Furthermore, a statistically significant increase in the percentage of macrophages and dendritic cells for  $^{115}\text{In}$  was observed on days 5, 10 and 15 post-injection (Figure 4-6). A population of  $^{115}\text{In}$ -positive B cells was identified on days 1, 5, 10 and 15 post-injection. Although there were more  $^{115}\text{In}$ -positive B cells dendritic cells and macrophages, the proportion of B cells positive for the dopant was small due to the higher number of B cells within the lymph node. The increased proportion of  $^{115}\text{In}$  within the B cells, dendritic cells and macrophages suggests that these APCs may be actively internalizing or sequestering the adjuvant.

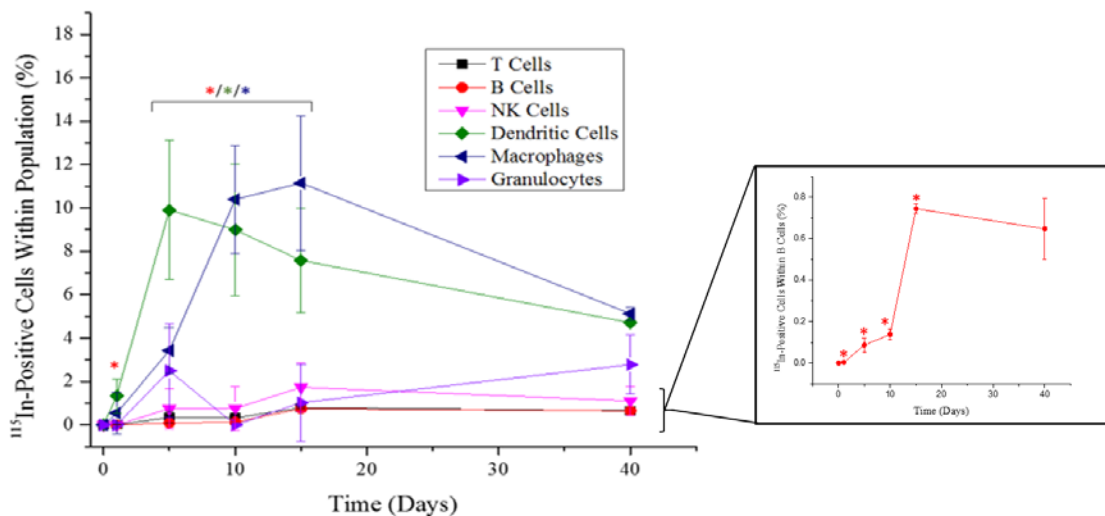


Figure 4- 6: Changes in the proportion of a cell population over time that are  $^{115}\text{In}$ -positive. The boxed insert helps to visualize the sequestration of the  $^{115}\text{In}$  dopant within the B cell population. An asterisks indicates a significant increase compared to control mice not exposed to 2.5%  $^{115}\text{In-AIO}(\text{OH})$ .

Dendritic cells within the lymph node that stained  $^{115}\text{In}$ -positive on day 1 post-injection showed upregulation of maturation markers (MHCII and CD86) compared to  $^{115}\text{In}$ -negative dendritic cells (Figure 4-7). There was a non-significant trend towards higher expression of MHCII/ CD86 in  $^{115}\text{In}$ -positive dendritic cells on the other assessed days.

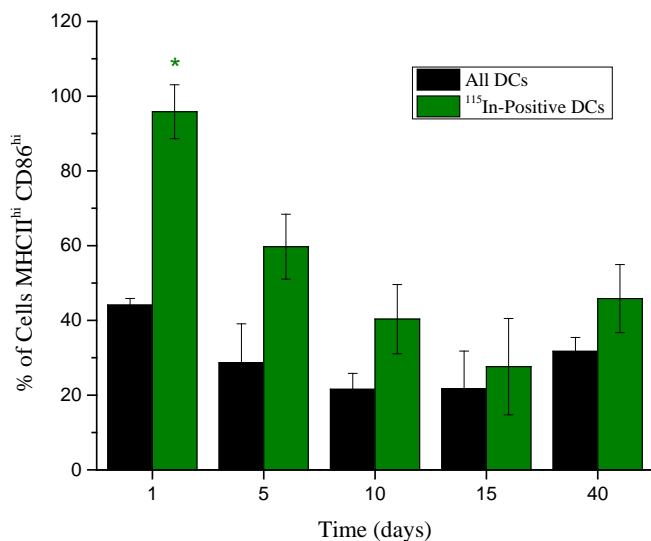


Figure 4- 7: Upregulation of maturation markers in  $^{115}\text{In}$ -positive dendritic cells.

## 4.4 Discussion

Although nanomaterials have been used in mass cytometry before (i.e., NaHoF<sub>4</sub> nanoparticles), they were only used to increase the amount of metal per antibody to more efficiently detect surface markers that are expressed at low levels (116). These nanoparticle-labeled antibodies are akin to using a brighter fluorophore in conventional flow cytometry. CyTOF has not been used for any other purpose beyond immunophenotyping to date (107). A novel application of mass cytometry was developed in this chapter to assess the kinetics and cellular distribution of 2.5% <sup>115</sup>In-AIO(OH). This technique has widespread applications within the nanomedicine field since any nanomaterials containing heavy metals, such as gold or silver nanoparticles, can be directly tracked *in vivo* in a high-dimensional single-cell manner.

Mass cytometry was used in this chapter to show that nanoparticles of indium-doped AIO(OH) distribute from the site of injection to the draining lymph node. <sup>115</sup>In-positive events were detected as early as 1 day post-administration and peaked at day 15. Using 500 nm fluorescent latex beads as a surrogate for Alhydrogel, Khan *et al.* found that the beads were observed in the draining lymph node within 1 day, but reached peak levels only at day 4 post-injection (45). Differences in the size, zeta potential, morphology and so forth between <sup>115</sup>In-AIO(OH) and the surrogate material provide an explanation for the above discrepancy. As discussed in chapter 2, indium-doped AIO(OH) very closely matches the properties of Alhydrogel and is a more representative tracer for the commercial adjuvant than latex beads.

Approximately 30% of the observed <sup>115</sup>In events within the lymph node at each time point were identified as <sup>115</sup>In-AIO(OH) nanoparticles not associated with a cell (<sup>115</sup>In<sup>hi</sup>, <sup>191/193</sup>Ir<sup>lo</sup>, <sup>195</sup>Pt<sup>hi</sup>, phenotypic marker<sup>lo</sup> events). The presence of these particles corroborates the 1955 report by White *et al.* that observed extracellular granular masses within the sinus of the draining lymph node 1 day post-injection (52). Khan *et al.* however, only observed the surrogate tracer within cells in the draining lymph node (45). At 500 nm in diameter, the surrogate material used in Khan's study were too large to enter the afferent lymphatic vessels and must be transported by an APC into the lymphatic system (48). The component nanoparticles of aluminum-based adjuvants are smaller enough (~10 x 5.5 nm) to efficiently enter the lymphatic vessels on their own from the site of injection (48).

There are currently 2 theories in the literature to explain how antigen adsorbed to an aluminum-based adjuvant enters the draining lymph node. First, de-adsorbed antigen can freely enter the lymph and be captured by resident dendritic cells and follicular B cells in the lymph node (117-119). Alternatively, adsorbed antigens can be phagocytosed at the site of injection and transported by APCs to the lymph node (15, 120). Since the adjuvant is coated with antigen, the cell unassociated particles may help to carry antigen to the lymph node and establish an additional depot at this site (38). A secondary antigen depot may help to clarify some of the controversy around the requirement of an injection site depot to generate an immune response to an aluminum-adsorbed vaccine (6, 25). Additional studies are required to assess this new theory.

The remainder of the  $^{115}\text{In}$  events observed in the lymph node with CyTOF were associated with cellular events. Unfortunately, mass cytometry cannot differentiate between extracellularly bound indium-doped AlO(OH) nanoparticles, internalized nanoparticles or cell-bound  $^{115}\text{In}$  released from dissolved adjuvant particles. However, the presence of a large population of cell unassociated adjuvant particles and the poor solubility of AlO(OH) suggests that a proportion of the  $^{115}\text{In}$ -positive cellular events are nanoparticles (44).

A statistically significant increase in the proportion of dendritic cells and macrophages positive for  $^{115}\text{In}$  was observed on days 5, 10 and 15 post-injection. Previous work in vitro has shown that APCs can internalize aluminum-based adjuvants (15, 39). Although the depletion of macrophages had a minimal impact on the immune response to an aluminum-adsorbed vaccine, depletion of monocytes and dendritic cells abrogated the response (29, 34).  $^{115}\text{In}$ -positive dendritic cells had increased expression of maturation markers (MHCII and CD86) on day 1 post injection. Work by Sokolovska *et al.* confirms that murine dendritic cells activate/mature in the presence of aluminum-based adjuvants (30). Monocyte-derived migratory dendritic cells from the injection site have been shown to orchestrate the adaptive immune response of aluminum-adsorbed vaccines, not residence dendritic cells in the lymph node (16, 117). It is currently unknown from the CyTOF analysis if the  $^{115}\text{In}$ -positive dendritic cells migrated to the lymph node or are resident cells in the lymph node. Khan *et al.* found that the surrogate materials in the lymph node were sequestered within macrophages and monocyte-derived dendritic cells 4 days post-administration (45). White *et al.* observed aluminum adjuvant-like granular masses in macrophages at day 1 post-injection (52). The immunological effects of aluminum precipitates within these populations in the draining lymph node remains to be explored.

A population of  $^{115}\text{In}$ -positive B cells was identified on days 1, 5, 10 and 15 post-injection. Nanoparticles <200 nm coated with adjuvant in the lymph node have been previously shown to be particularly effective at stimulating humoral immune responses since the unprocessed antigen can be recognized and efficiently phagocytosed by antigen-specific B cells (48). When administered intraperitoneally, aluminum-based adjuvants were found to be taken up by resident B-cells (15). It is unknown if only antigen specific B cells phagocytose aluminum-based adjuvants and the general immunological consequences of the adjuvant within this cell type.

## Chapter 5: STEM-Based Assessment of Alhydrogel's Biodistribution

### 5.1. Introduction

Alhydrogel is poorly soluble in physiological fluids and has been shown to persist at the site of injection for upwards of 12 years (43, 44). Electron micrographs of the injection site of Alhydrogel-adsorbed vaccines in patients with MMF have shown that the adjuvant particles are phagocytosed by macrophages and maintain their needle-like morphology within these cells (43). To further validate 2.5%  $^{115}\text{In-AIO(OH)}$  as a tool to study Alhydrogel, STEM imaging was used to assess the morphology of the adjuvant within the injection site nodule after 70 days. Atomic mapping was also used to assess the long-term persistence and concentration of the indium dopant *in vivo*.

Data from the previous CyTOF analysis suggested that nanoparticles of 2.5%  $^{115}\text{In-AIO(OH)}$  reached peak levels in the draining lymph node by day 15 post-injection before slowly clearing from the tissue. STEM imaging was used in this chapter to confirm the presence of Alhydrogel particles within the inguinal lymph nodes. A later time point, 70 days, was assessed seeing how other investigators have already observed structures that resemble aluminum adjuvant particles at this site within a day of administration (52, 54).

The translocation of AIO(OH) particles to the liver is supported by the biodistribution data from surrogate nanomaterials, nanodiamonds functionalized Alhydrogel,  $^{111}\text{In-AIO(OH)}$  and  $^{26}\text{Al-AIO(OH)}$  (45, 50, 53). The distribution of Alhydrogel to the liver is further supported by the results of a recent phase IIa clinical trial of a therapeutic hepatitis B vaccine (121). Patients in the control group of this trial received 6 intramuscular injection of an aluminum-based adjuvant with no adsorbed antigen (121). Surprisingly, this group had a reduced viral load and developed antibodies against the hepatitis B e antigen (HBeAg) to a similar extent as the treatment group (121). Wang *et al.* replicated the trial in mice and observed that repeated injections of Alhydrogel alone resulted in a high number of spotty necrotic foci in the liver, the site of infection for the hepatitis B virus (122). Although the cause of these observations is currently unknown, the presence of Alhydrogel particles in the liver may provide some clarity since the adjuvant is well known to cause necrosis at the site of injection (15, 26, 27). The accumulation of AIO(OH) nanoparticles in the liver would not be surprising, given that this organ is part of the reticuloendothelial system and is efficient at sequestering nanomaterials (104). STEM imaging combined with atomic mapping was used to search for Alhydrogel particles in the liver after 70 days post-administration in this chapter.

## **5.2. Materials and Methods**

### **5.2.1. Animal Immunizations and Tissue Fixation**

C57BL/6 mice (n=2/ group) between 6-8 weeks old were injected into the posterior region of the dorsal surface with 100 µg of OVA adsorbed to 0.7 mg of 2.5% <sup>115</sup>In-AlO(OH) or Alhydrogel in a total volume of 100 µL. After 70 days, the animals were sacrificed via CO<sub>2</sub> asphyxiation while under anesthesia with isoflurane. The site of injection/ nodule was removed in all animals as well as the draining inguinal lymph nodes and liver in those administered Alhydrogel. A 2-3 mm<sup>3</sup> block of each tissue was fixed for 1 hour in a solution of 2.5% glutaraldehyde (Polyscience BLI1909) and 2.5% paraformaldehyde (Polysciences 18814) in 0.1M sodium cacodylate buffer at pH 7.4 (Ted Pella 18851) (123, 124). The samples were then placed into fresh fixative for an additional 24 hours at 4°C (123, 124).

### **5.2.2. Tissue Embedding and Preparation for STEM Imaging**

The fixed tissue was rinsed thrice with 0.1 M sodium cacodylate buffer at pH 7.4 and post-fixed in buffer 1% OsO<sub>4</sub> (Polysciences 0972B) for 2 hours at 4°C (123, 124). The samples were rinsed thrice with 18 MΩ water and then taken through a graded dehydration with ethanol (123, 124). Post-dehydration, the samples were infiltrated with Spurr resin (Ted Pella 18300-4221) using a Pelco 3441 laboratory microwave under vacuum; the first infiltration was in 50% resin using acetone as the diluent followed by three 100% resin steps (125, 126). The resin was then polymerized over a period of 72 hours at 65°C (125, 126). The blocks were sectioned 200 nm thick on a Leica Ultracut 7 ultramicrotome before mounting onto formvar and carbon backed 200 mesh copper grids (Ted Pella 01810).

### **5.2.3. STEM Imaging and Data Analysis**

The mounted sections were systematically searched under HAADF TEM mode with the Technai Osiris microscope described in chapter 2. When a region of higher atomic number with a similar morphology to AlO(OH) nanoparticles was identified, it was atomically mapped under STEM mode. A minimum of 3 slices/ tissue type/ animal were assessed. The EDX data was analyzed and corrected for Bremsstrahlung radiation using Esprit 1.9 software (Bruker). Representative pictures are shown below.

### **5.2.4. Ethics Statement**

All animal experiments were carried out in accordance with the guidelines of the University of British Columbia's Animal Care Committee under the approved protocol A14-0159.

### 5.3. Results

#### 5.3.1. Persistence, Morphology and Cellular Infiltration of Alhydrogel and 2.5% $^{115}\text{In-AIO(OH)}$ at the Site of Injection

70-days post-administration, a considerable amount of adjuvant could still be found at the site of injection within an inflammatory nodule (Figure 5-1). These nodules form within 4 hours of injection in a fibrinogen/fibrin-dependent manner (127). The long-term persistence of Alhydrogel nodules helps to explain why the adjuvant is administered into deep tissue layers, such as the muscle, to minimize adverse events like pruritus (128, 129).

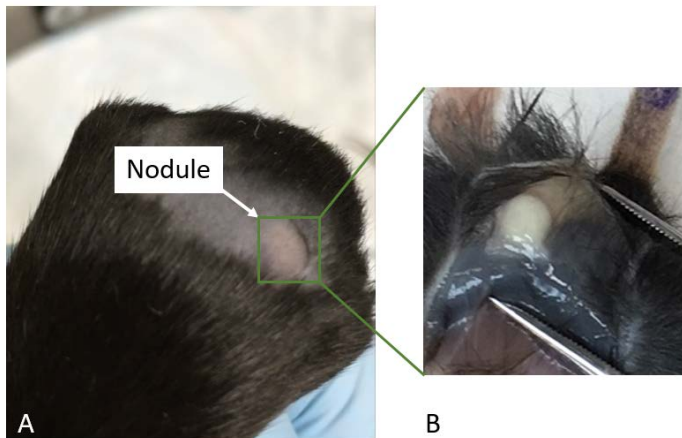


Figure 5- 1: Injection site nodule from the surface of the skin (A) and after retracting the skin (B) 70 days post-administration.

Both 2.5%  $^{115}\text{In-AIO(OH)}$  and Alhydrogel maintained their characteristic needle-like morphology after a prolonged period *in vivo* (Figures 5-1 and 5-2). Elemental mapping of the 2.5%  $^{115}\text{In-AIO(OH)}$  injection site showed that the heavy metal dopant was still associated with the adjuvant. The amount of indium detected was equivalent to  $2.16 \pm 0.28\%$  of the aluminum atoms, a non-statistical difference from before administration (Figure 5-2).

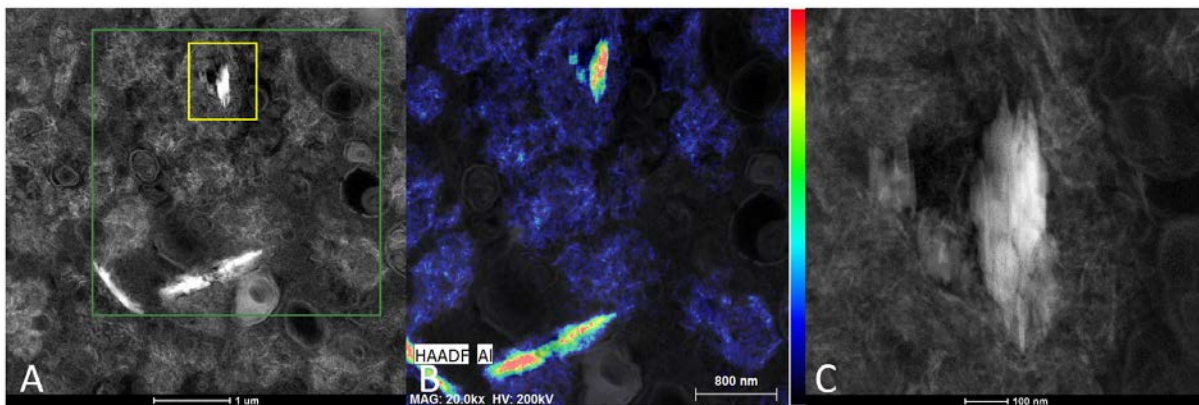


Figure 5- 2: Alhydrogel at the site of injection (A). Atomic mapping for aluminum (B) in the region outlined by the green box in panel A. Higher magnification view of the region in the yellow box in panel A showing that the needle-like morphology of Alhydrogel was maintained after 70 days *in vivo* (C).

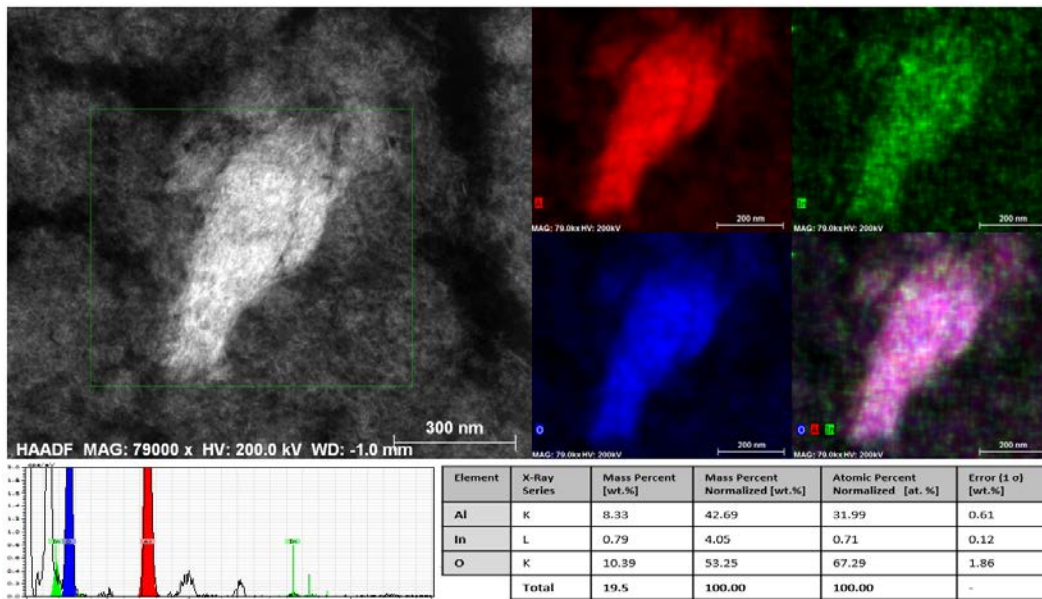


Figure 5- 3: Morphology and elemental mapping of 2.5% <sup>115</sup>In-AIO(OH) at the site of injection 70 days post-administration. The top panel shows a reference HAADF image and the distribution of aluminum (red), indium (green) and oxygen (blue). The bottom panel shows the EDX spectrum (left) and results from the quantification of the EDX data (right).

Cells could be found dispersed throughout the aluminum-based adjuvant within the injection site nodule. The exact phenotype of the cell infiltrate could not be determined with the data collected. Figure 5-3 is a representative image from the Alhydrogel injection site 70-days post-administration. The presence of cells was confirmed via elemental mapping for osmium, which stains the DNA within nuclei (123, 124). Other investigators have previously shown that aluminum-based adjuvants attract various cell types, such as monocytes and B cells, to the site of injection (15, 16, 52).

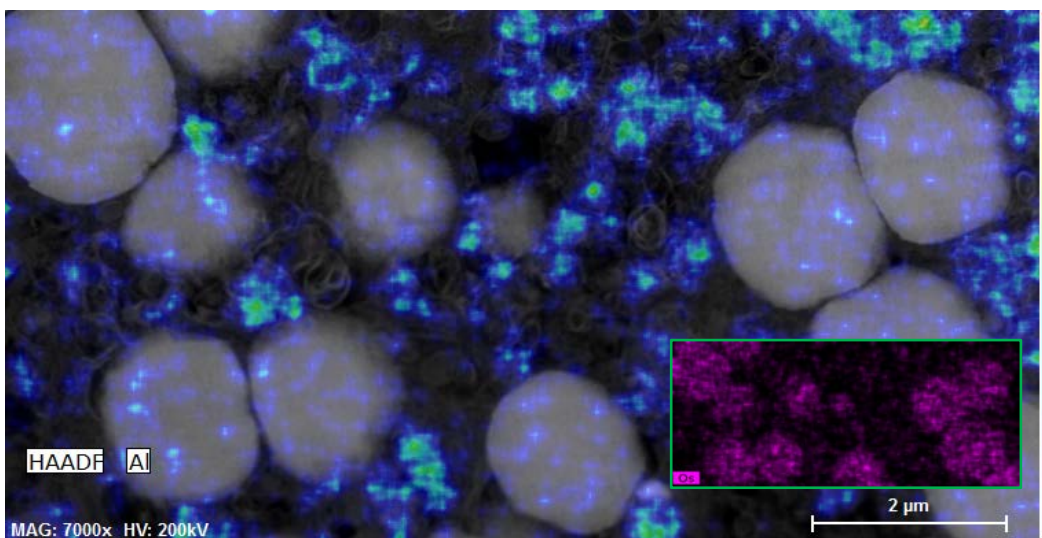


Figure 5- 4: Cellular infiltrate within the Alhydrogel injection site. Aluminum is displayed as a heat map while the insert shows the distribution of osmium in purple.

### 5.3.2. *Alhydrogel Particles within the Draining Lymph Node 70 Days Post-Injection*

Figure 5-4 shows an representative image of an aluminum aggregate within the dLN of a mouse administered Alhydrogel 70 days earlier into the subcutaneous fat. This finding helps to validate the observations from the CyTOF assessment in chapter 4.

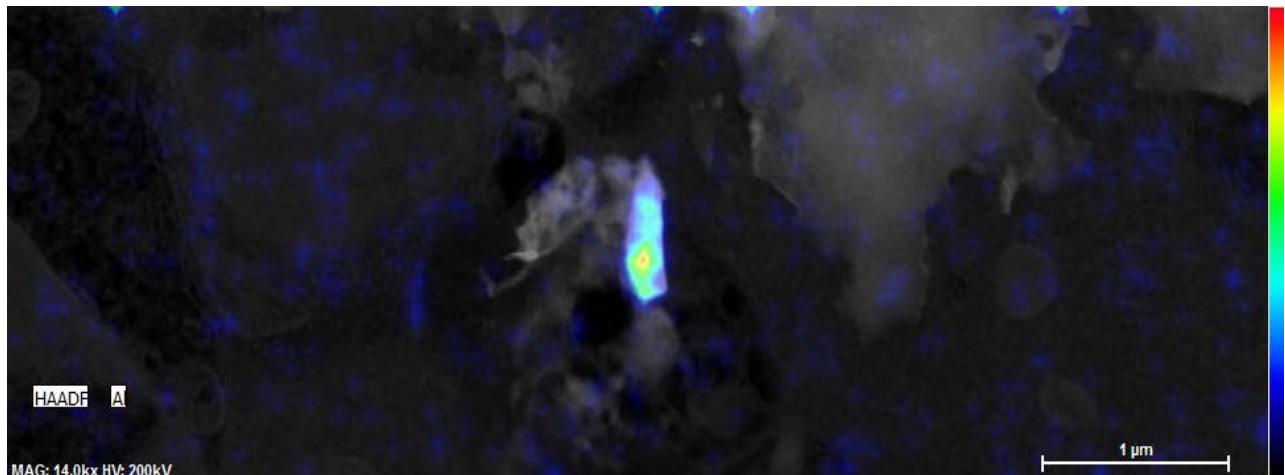


Figure 5- 5: An representative aggregate of Alhydrogel within the draining lymph node. The distribution of aluminum is presented as a heat map.

### 5.3.3. *Alhydrogel Particles within the Liver After 70 Days Post-Injection*

Nanoparticles of Alhydrogel with a distinct needle-like morphology were identified in the liver 70 days post-administration of the adjuvant. The adjuvant nanoparticles appear to be intracellular, although the type of cell and its subcellular location were difficult to determine. The liver is part of the reticuloendothelial system and contains a large number of Kupffer cells, a specialized type of macrophage, that are highly efficient at clearing nanomaterials from the systemic circulation (104).

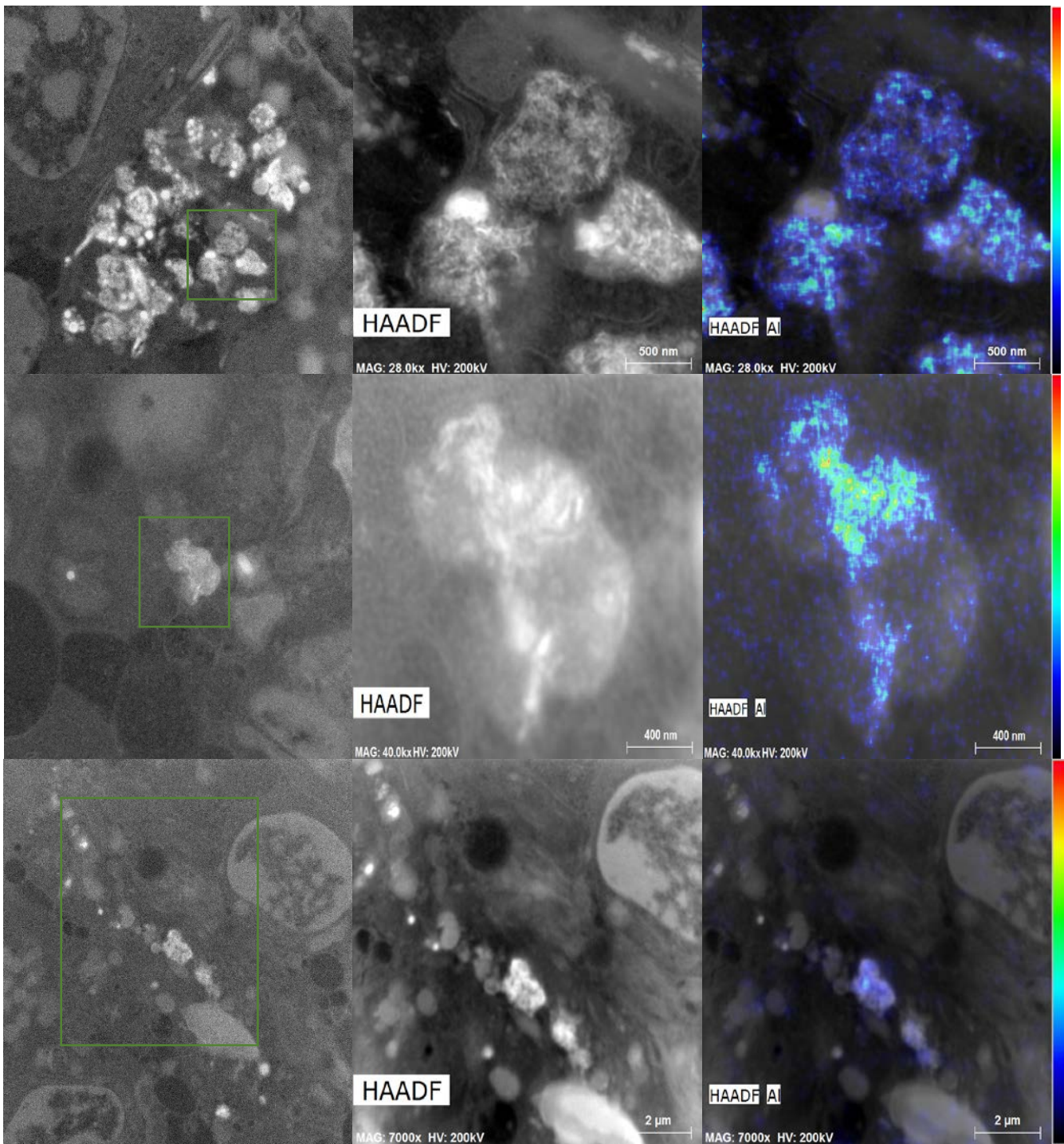


Figure 5- 6: Alhydrogel nanoparticles within 3 different sites of the liver from 2 different animals. The distribution of aluminum as a heat map is shown in the rightmost panels

## 5.4. Discussion

Results from this chapter help to further validate indium-doped AlO(OH) as a traceable form of Alhydrogel. Both 2.5%  $^{115}\text{In}$ -AlO(OH) and the commercial adjuvant were found to maintain their needle-like morphology after an extensive duration *in vivo*. This finding is corroborated by the persistence of Alhydrogel nanoparticles at the site of injection in MMF patients (43). The concentration of  $^{115}\text{In}$  within the adjuvant at the injection site was not statistically different from before administration, demonstrating the long-term stability of the doped particles. 2.5%  $^{115}\text{In}$ -AlO(OH) overcomes the stability issues associated with other tracer designs, such as electrostatically adsorbed nanodiamonds to Alhydrogel's surface (53). The stability of the doped tracer and the direct observation of Alhydrogel particles in the lymph node at day 70 support the notion that most of  $^{115}\text{In}$ -positive events observed with CyTOF analysis are 2.5%  $^{115}\text{In}$ -AlO(OH) nanoparticles (chapter 4).

This chapter presented the first observation of an aluminum-based adjuvant distributing from the site of injection to the liver. The adjuvant nanoparticles maintained their distinct morphology in the liver and appeared to be intracellular. Additional assessments are required to determine the exact subcellular location and phenotype of the adjuvant positive cells. Since the liver clears nanomaterials from the systemic circulation, the Alhydrogel particles must have entered the blood (104). Although the details have yet to be elucidated, one can hypothesize that the particles entered via the lymphatic system since extracellular  $^{115}\text{In}$ -AlO(OH) nanoparticles are found in the draining lymph node and ablation of the nodes reduced the distribution of surrogate materials into the blood (45). The presence of AlO(OH) particle in the liver combined with the poor solubility of AlO(OH) under physiological conditions suggests that the initial burst phase of  $^{111}\text{In}$ -AlO(OH) and  $^{26}\text{Al}$ -AlO(OH) is due at least in part to the distribution of the adjuvant in particulate form. Although the presence of Alhydrogel particles within the liver may help to explain the necrotic foci observed by Wang *et al.*, more detailed assessments are required before making such a claim (122).

## Chapter 6: Conclusion and Future Work

### 6.1. Conclusion

The primary objective of this thesis was to improve the understanding of the biodistribution of aluminum-based adjuvants like Alhydrogel. Although the adjuvant has been used for nearly a century clinically, its biodistribution has been sparsely studied. This is not surprising, considering that even regulatory agencies do not require pharmacokinetic data for adjuvants (130).

In order to study the biodistribution of Alhydrogel in detail, a novel tracing strategy was developed where indium isotopes were incorporated into the AlO(OH) matrix using a highly controlled co-precipitation technique. Both the gamma emitter  $^{111}\text{In}$  and non-radioactive  $^{115}\text{In}$  were efficiently encapsulated into the adjuvant. A number of physical and functional assays were used to confirm that the adjuvant closely matched Alhydrogel. Specifically, the indium-doped adjuvant matched Alhydrogel with regards to its FTIR and DSC spectrum, protein adsorptivity and de-adsorptivity, size and morphology of the component nanoparticles, stability in biological media, size and zeta potential. The  $^{111/115}\text{In}$ -AlO(OH) tracer generated a similar humoral and cellular immune response when compared to Alhydrogel (34, 80-83). The rate release for adsorbed antigens (i.e.,  $^{67}\text{Ga}$ -NOTA-OVA) between the indium-doped adjuvant and Alhydrogel from the site of injection was identical. In-AlO(OH) was found to be persistent at the site of injection and maintain its needle-like morphology as has been observed for Alhydrogel in animal models and humans (21, 23, 43). Only minor differences were observed between the doped and commercial adjuvant, namely the presence of a small amount of  $\text{Al}(\text{OH})_3$  in Alhydrogel and a minor increase in the cytotoxicity of  $^{115}\text{In}$ -AlO(OH). Compared to the other tracers used to date, indium-doped AlO(OH) is the most stable and representative tracer of Alhydrogel (45, 52).

The biodistribution data of both  $^{111}\text{In}$ -AlO(OH) and  $^{26}\text{Al}$ -AlO(OH) found that a small burst of activity was released from the injection site shortly after administration followed by a slower phase of distribution (50). This pharmacokinetic profile is poorly explained by the dissolution of the tracer from the injection site given the poor solubility of AlO(OH) in biological media (44, 50, 51). A novel application of CyTOF and STEM imaging was used to show that the radioactive signal in the liver and draining lymph node was at least partially due to the presence of adjuvant nanoparticles. Within the draining lymph node, the adjuvant particles reached peak levels at day 15 and were sequestered into populations of APCs; adjuvant-positive dendritic cells also showed signs of maturation. The distribution of Alhydrogel nanoparticles supports the hypothesis of antigen depots forming in tissues beyond the site of administration (38).

This study provided the most detailed assessment to date of the biodistribution of Alhydrogel. The observation of adjuvant particles beyond the site of injection departs from the long term belief in the vaccinology community that aluminum-based adjuvants remain at the site of injection and slowly dissolve over time. This

finding opens a Pandora's box of questions as the immunological and toxicological effects of the adjuvant now have to be studied at these new sites.

## 6.2. Future Work

The biodistribution data from  $^{111}\text{In}$ -AlO(OH) in chapter 3 found radioactivity in tissues such as the draining lymph node, spleen, liver, kidney and bone. Work in this thesis found that the  $^{111}\text{In}$  signal was at least in part attributed to the adjuvant in nanoparticle form within the draining lymph node and liver. The other organ systems with  $^{111}\text{In}$  uptake need to be assessed with techniques like CyTOF and STEM imaging to determine if signal is due to the radionuclide in soluble form or nanoparticles of the adjuvant. Techniques such as ImmunoGold can be used to obtain data about the subcellular location of the adjuvant nanoparticles with electron microscopy (131). To better understand Alhydrogel's toxicity, MTT and related assays should be carried out on the predominant cell types found where the nanoparticles of the adjuvant distribute. Additional work is required to assess if rare side effects, such as ASIA, are due to the direct toxicity of the particles or the long-term pro-inflammatory effects of bio-persistent nanomaterials at distant sites (42, 45, 46).

To better understand the immunological consequences of the adjuvant, the CyTOF panel used in the thesis can be readily expanded (106). Additional phenotypic markers will allow the different cell populations to be more specifically defined and answer key questions. For example, are the  $^{115}\text{In}$ -positive dendritic cells with upregulated maturation markers in the lymph node resident cells or a migratory cell from the site of injection?

To assess if a secondary antigen depot is formed in the lymph node, as theorized in this thesis, a variety of techniques are required. ImmunoGold staining, electron microscopy and atomic mapping can be used together to determine if the extracellular Alhydrogel in the lymph node is coated with antigen (131). By labeling the antigen with a heavy metal, CyTOF can be used to assess the cellular distribution of the antigen in relation to the adjuvant. Finally,  $^{67}\text{Ga}$ -NOTA-OVA, described in chapter 3, can be used to quantify the amount of antigen within the draining lymph node when administered as a soluble antigen or adsorbed to an aluminum precipitate.

Long-lived inflammatory nodules at the site of injection form rapidly following administration to help entrap the adjuvant (127). Interestingly, when pre-formed aluminum precipitates are administered into fibrinogen-deficient mice, a nodule does not form and cell-mediated immunity is enhanced to the adsorbed antigen (127). Next-generation aluminum-based adjuvants that minimize aggregation of the component nanoparticles have also shown enhanced cellular immunity (132-135). The techniques established in this thesis can be used to assess the distribution of Alhydrogel particles in a fibrinogen knockout model and next-generation aluminum-based adjuvants to determine if the pharmacokinetics of the particles correlates with enhanced cellular immunity. It would also be interesting to assess if the application of ultrasound to the injection site, which is

known to disrupt Alhydrogel aggregates in vitro, can enhance the distribution of the adjuvant and alter the type of immune response generated (14).

This thesis focused on the distribution of Alhydrogel from the subcutaneous space. In clinical practice, the adjuvant is commonly also administered intramuscularly and it would be interesting to assess if the site of injection impacts the distribution of the adjuvant (3, 8, 9). Finally, this thesis concentrated solely on the biodistribution of crystalline AlO(OH); techniques developed here should be applied to study the movement of the amorphous aluminum-based adjuvants, such as aluminum hydroxyphosphate (12).

## References

1. Ramon G. Sur l'augmentation anormale de l'antitoxine chez les chevaux producteurs de sérum antidiphthérique. *Bull Soc Centr Med Vet.* 1925;101:227-34.
2. Ramon G. Procédé pour accroître la production des antitoxines. *Ann Inst Pasteur.* 1926;40:1-10.
3. Plotkin SA, Orenstein WA, Offit PA. *Vaccines: Expert Consult.* 6: Elsevier Health Sciences; 2012. p. 1-63.
4. Glenny AT, Pope CG, Waddington H, Wallace U. Immunological notes. XVII–XXIV. *The Journal of Pathology and Bacteriology.* 1926;29(1):31-40.
5. Shirodkar S, Hutchinson RL, Perry DL, White JL, Hem SL. Aluminum Compounds Used as Adjuvants in Vaccines. *Pharmaceutical research.* 1990;7(12):1282-8.
6. Holt LB. *Developments in Diphtheria Prophylaxis: Heinemann; 1950 1950.*
7. Maschmann E, Küster E, Fischer W. Über die Fähigkeit des Tonerde-Präparates B, Diphtherie-Toxin zu adsorbieren. *Berichte der deutschen chemischen Gesellschaft (A and B Series).* 1931;64(8):2174-8.
8. Marrack P, McKee AS, Munks MW. Towards an understanding of the adjuvant action of aluminium. *Nat Rev Immunol.* 2009;9(4):287-93.
9. Reed SG, Orr MT, Fox CB. Key roles of adjuvants in modern vaccines. *Nat Med.* 2013;19(12):1597-608.
10. Tagliabue A, Rappuoli R. Vaccine adjuvants: the dream becomes real. *Hum Vaccin.* 2008;4(5):347-9.
11. FDA Approves New Vaccine for Prevention of Cervical Cancer: FDA; 2009 [cited July 19, 2016]. Available from: <http://www.fda.gov/NewsEvents/Newsroom/PressAnnouncements/ucm187048.htm>.
12. Hem SL, Hogenesch H. Relationship between physical and chemical properties of aluminum-containing adjuvants and immunopotentiality. *Expert review of vaccines.* 2007;6(5):685-98.
13. Stewart-Tull DES. Recommendations for the Assessment of Adjuvants (Immunopotentiators). In: Gregoriadis G, Allison A, Poste G, editors. *Immunological Adjuvants and Vaccines.* NATO ASI Series. 179: Springer US; 1989. p. 213-26.
14. Harris JR, Soliakov A, Lewis RJ, Depoix F, Watkinson A, Lakey JH. Alhydrogel(R) adjuvant, ultrasonic dispersion and protein binding: a TEM and analytical study. *Micron.* 2012;43(2-3):192-200.
15. Kool M, Soullie T, van Nimwegen M, Willart MA, Muskens F, Jung S, et al. Alum adjuvant boosts adaptive immunity by inducing uric acid and activating inflammatory dendritic cells. *J Exp Med.* 2008;205(4):869-82.
16. Lu F, Hogenesch H. Kinetics of the inflammatory response following intramuscular injection of aluminum adjuvant. *Vaccine.* 2013;31(37):3979-86.
17. Ghimire TR, Benson RA, Garside P, Brewer JM. Alum increases antigen uptake, reduces antigen degradation and sustains antigen presentation by DCs in vitro. *Immunol Lett.* 2012;147(1-2):55-62.

18. Morefield GL, Sokolovska A, Jiang D, HogenEsch H, Robinson JP, Hem SL. Role of aluminum-containing adjuvants in antigen internalization by dendritic cells in vitro. *Vaccine*. 2005;23(13):1588-95.
19. Bachmann MF, Jennings GT. Vaccine delivery: a matter of size, geometry, kinetics and molecular patterns. *Nature reviews Immunology*. 2010;10(11):787-96.
20. Glennly AT, Buttle GAH, Stevens MF. Rate of disappearance of diphtheria toxoid injected into rabbits and guinea - pigs: Toxoid precipitated with alum. *The Journal of Pathology and Bacteriology*. 1931;34(2):267-75.
21. Verdier F, Burnett R, Michelet-Habchi C, Moretto P, Fievet-Groyne F, Sauzeat E. Aluminium assay and evaluation of the local reaction at several time points after intramuscular administration of aluminium containing vaccines in the Cynomolgus monkey. *Vaccine*. 2005;23(11):1359-67.
22. Harrison WT. Some Observations on the Use of Alum Precipitated Diphtheria Toxoid. *American Journal of Public Health and the Nations Health*. 1935;25(3):298-300.
23. Kashiwagi Y, Maeda M, Kawashima H, Nakayama T. Inflammatory responses following intramuscular and subcutaneous immunization with aluminum-adjuvanted or non-adjuvanted vaccines. *Vaccine*. 2014;32(27):3393-401.
24. Noe SM, Green MA, HogenEsch H, Hem SL. Mechanism of immunopotentiality by aluminum-containing adjuvants elucidated by the relationship between antigen retention at the inoculation site and the immune response. *Vaccine*. 2010;28(20):3588-94.
25. Hutchison S, Benson RA, Gibson VB, Pollock AH, Garside P, Brewer JM. Antigen depot is not required for alum adjuvant activity. *FASEB journal : official publication of the Federation of American Societies for Experimental Biology*. 2012;26(3):1272-9.
26. Marichal T, Ohata K, Bedoret D, Mesnil C, Sabatel C, Kobiyama K, et al. DNA released from dying host cells mediates aluminum adjuvant activity. *Nat Med*. 2011;17(8):996-1002.
27. Goto N, Kato H, Maeyama J-i, Shibano M, Saito T, Yamaguchi J, et al. Local tissue irritating effects and adjuvant activities of calcium phosphate and aluminium hydroxide with different physical properties. *Vaccine*. 1997;15(12-13):1364-71.
28. Abderrazak A, Syrovets T, Couchie D, El Hadri K, Friguet B, Simmet T, et al. NLRP3 inflammasome: From a danger signal sensor to a regulatory node of oxidative stress and inflammatory diseases. *Redox Biology*. 2015;4:296-307.
29. Kool M, Pétrilli V, De Smedt T, Rolaz A, Hammad H, van Nimwegen M, et al. Cutting Edge: Alum Adjuvant Stimulates Inflammatory Dendritic Cells through Activation of the NALP3 Inflammasome. *The Journal of Immunology*. 2008;181(6):3755-9.
30. Sokolovska A, Hem SL, HogenEsch H. Activation of dendritic cells and induction of CD4(+) T cell differentiation by aluminum-containing adjuvants. *Vaccine*. 2007;25(23):4575-85.

31. Eisenbarth SC, Colegio OR, O'Connor W, Sutterwala FS, Flavell RA. Crucial role for the Nalp3 inflammasome in the immunostimulatory properties of aluminium adjuvants. *Nature*. 2008;453(7198):1122-6.
32. Li H, Willingham SB, Ting JPY, Re F. Cutting Edge: Inflammasome activation by Alum and Alum's adjuvant effect are mediated by NLRP3. *Journal of immunology (Baltimore, Md : 1950)*. 2008;181(1):17-21.
33. Franchi L, Nunez G. The Nlrp3 inflammasome is critical for aluminium hydroxide-mediated IL-1beta secretion but dispensable for adjuvant activity. *European journal of immunology*. 2008;38(8):2085-9.
34. McKee AS, Munks MW, MacLeod MK, Fleenor CJ, Van Rooijen N, Kappler JW, et al. Alum induces innate immune responses through macrophage and mast cell sensors, but these sensors are not required for alum to act as an adjuvant for specific immunity. *J Immunol*. 2009;183(7):4403-14.
35. Flach TL, Ng G, Hari A, Desrosiers MD, Zhang P, Ward SM, et al. Alum interaction with dendritic cell membrane lipids is essential for its adjuvanticity. *Nat Med*. 2011;17(4):479-87.
36. Kuroda E, Ishii KJ, Uematsu S, Ohata K, Coban C, Akira S, et al. Silica crystals and aluminum salts regulate the production of prostaglandin in macrophages via NALP3 inflammasome-independent mechanisms. *Immunity*. 2011;34(4):514-26.
37. Mori A, Oleszycka E, Sharp FA, Coleman M, Ozasa Y, Singh M, et al. The vaccine adjuvant alum inhibits IL-12 by promoting PI3 kinase signaling while chitosan does not inhibit IL-12 and enhances Th1 and Th17 responses. *European journal of immunology*. 2012;42(10):2709-19.
38. Oleszycka E, Lavelle EC. Immunomodulatory properties of the vaccine adjuvant alum. *Current opinion in immunology*. 2014;28:1-5.
39. Mold M, Eriksson H, Siesjö P, Darabi A, Shardlow E, Exley C. Unequivocal identification of intracellular aluminium adjuvant in a monocytic THP-1 cell line. *Scientific reports*. 2014;4.
40. Eickhoff TC, Myers M. Workshop summary. Aluminum in vaccines. *Vaccine*. 2002;20 Suppl 3:S1-4.
41. Eldred BE, Dean AJ, McGuire TM, Nash AL. Vaccine components and constituents: responding to consumer concerns. *The Medical journal of Australia*. 2006;184(4):170-5.
42. Vera-Lastra O, Medina G, Cruz-Dominguez Mdel P, Jara LJ, Shoenfeld Y. Autoimmune/inflammatory syndrome induced by adjuvants (Shoenfeld's syndrome): clinical and immunological spectrum. *Expert Rev Clin Immunol*. 2013;9(4):361-73.
43. Gherardi RK, Coquet M, Cherin P, Belec L, Moretto P, Dreyfus PA, et al. Macrophagic myofasciitis lesions assess long-term persistence of vaccine-derived aluminium hydroxide in muscle. *Brain*. 2001;124(Pt 9):1821-31.
44. Seeber SJ, White JL, Hem SL. Solubilization of aluminum-containing adjuvants by constituents of interstitial fluid. *Journal of parenteral science and technology : a publication of the Parenteral Drug Association*. 1991;45(3):156-9.

45. Khan Z, Combadiere C, Authier FJ, Itier V, Lux F, Exley C, et al. Slow CCL2-dependent translocation of biopersistent particles from muscle to brain. *BMC medicine*. 2013;11:99.
46. Gherardi RK, Eidi H, Crépeaux G, Authier Fç J, Cadusseau J. Biopersistence and Brain Translocation of Aluminum Adjuvants of Vaccines. *Front Neurol*. 2015;6.
47. Morefield GL, HogenEsch H, Robinson JP, Hem SL. Distribution of adsorbed antigen in mono-valent and combination vaccines. *Vaccine*. 2004;22(15-16):1973-84.
48. Bachmann MF, Jennings GT. Vaccine delivery: a matter of size, geometry, kinetics and molecular patterns. *Nature reviews Immunology*. 2010;10(11):787-96.
49. Oyewumi MO, Kumar A, Cui ZR. Nano-microparticles as immune adjuvants: correlating particle sizes and the resultant immune responses. *Expert review of vaccines*. 2010;9(9):1095-107.
50. Flarend RE, Hem SL, White JL, Elmore D, Suckow MA, Rudy AC, et al. In vivo absorption of aluminium-containing vaccine adjuvants using <sup>26</sup>Al. *Vaccine*. 1997;15(12-13):1314-8.
51. Hem SL. Elimination of aluminum adjuvants. *Vaccine*. 2002;20, Supplement 3:S40-S3.
52. White RG, Coons AH, Connolly JM. Studies on antibody production. III. The alum granuloma. *J Exp Med*. 1955;102(1):73-82.
53. Eidi H, David MO, Crepeaux G, Henry L, Joshi V, Berger MH, et al. Fluorescent nanodiamonds as a relevant tag for the assessment of alum adjuvant particle biodisposition. *BMC medicine*. 2015;13:144.
54. Giusti F, Seubert A, Cantisani R, Tortoli M, D'Oro U, Ferlenghi I, et al. Ultrastructural Visualization of Vaccine Adjuvant Uptake In Vitro and In Vivo. *Microscopy and Microanalysis*. 2015;21(04):791-5.
55. O'Hagan DT, De Gregorio E. The path to a successful vaccine adjuvant--'the long and winding road'. *Drug Discov Today*. 2009;14(11-12):541-51.
56. MacLeod MKL, McKee AS, David A, Wang J, Mason R, Kappler JW, et al. Vaccine adjuvants aluminum and monophosphoryl lipid A provide distinct signals to generate protective cytotoxic memory CD8 T cells. *Proceedings of the National Academy of Sciences of the United States of America*. 2011;108(19):7914-9.
57. Morefield GL, Jiang D, Romero-Mendez IZ, Geahlen RL, HogenEsch H, Hem SL. Effect of phosphorylation of ovalbumin on adsorption by aluminum-containing adjuvants and elution upon exposure to interstitial fluid. *Vaccine*. 2005;23(12):1502-6.
58. Mile I, Svensson A, Darabi A, Mold M, Siesjo P, Eriksson H. Al adjuvants can be tracked in viable cells by lumogallion staining. *Journal of immunological methods*. 2015;422:87-94.
59. Browne BA, McColl JG, Driscoll CT. Aluminum Speciation Using Morin: I. Morin and Its Complexes with Aluminum. *Journal of Environmental Quality*. 1990;19(1):65-72.
60. Vanhecke D, Rodriguez-Lorenzo L, Clift MJ, Blank F, Petri-Fink A, Rothen-Rutishauser B. Quantification of nanoparticles at the single-cell level: an overview about state-of-the-art techniques and their limitations. *Nanomedicine (Lond)*. 2014;9(12):1885-900.

61. Xu Z, Yu J, Low J, Jaroniec M. Microemulsion-assisted synthesis of mesoporous aluminum oxyhydroxide nanoflakes for efficient removal of gaseous formaldehyde. *ACS applied materials & interfaces*. 2014;6(3):2111-7.
62. Yau KP, Schulze DG, Johnston CT, Hem SL. Aluminum hydroxide adjuvant produced under constant reactant concentration. *J Pharm Sci*. 2006;95(8):1822-33.
63. Brom M, Joosten L, Oyen WJG, Gotthardt M, Boerman OC. Improved labelling of DTPA- and DOTA-conjugated peptides and antibodies with (111)In in HEPES and MES buffer. *EJNMMI research*. 2012;2:4-.
64. Udenfriend S, Stein S, Bohlen P, Dairman W, Leimgruber W, Weigele M. Fluorescamine: a reagent for assay of amino acids, peptides, proteins, and primary amines in the picomole range. *Science*. 1972;178(4063):871-2.
65. Kaufmann AM, Goldman SDB, Krise JP. A fluorescence resonance energy transfer-based approach for investigating late endosome–lysosome retrograde fusion events. *Anal Biochem*. 2009;386(1):91-7.
66. Xia M, Huang R, Witt KL, Southall N, Fostel J, Cho MH, et al. Compound Cytotoxicity Profiling Using Quantitative High-Throughput Screening. *Environmental Health Perspectives*. 2008;116(3):284-91.
67. HEK-293 (ATCC CRL-1573): ATCC; 2016 [cited July 12, 2016]. Available from: <https://www.atcc.org/products/all/CRL-1573.aspx>.
68. van Meerloo J, Kaspers GJ, Cloos J. Cell sensitivity assays: the MTT assay. *Methods in molecular biology*. 2011;731:237-45.
69. Hafeli UO, Riffle JS, Harris-Shekhawat L, Carmichael-Baranauskas A, Mark F, Dailey JP, et al. Cell uptake and in vitro toxicity of magnetic nanoparticles suitable for drug delivery. *Molecular pharmaceutics*. 2009;6(5):1417-28.
70. Schorn W, Grosse-Hagenbrock D, Oelkers B, Sundermeyer J. Formazanido complexes of heavier group 13 elements aluminium, gallium, and indium. *Dalton transactions (Cambridge, England : 2003)*. 2016;45(3):1201-7.
71. Rye HS, Yue S, Wemmer DE, Quesada MA, Haugland RP, Mathies RA, et al. Stable fluorescent complexes of double-stranded DNA with bis-intercalating asymmetric cyanine dyes: properties and applications. *Nucleic Acids Res*. 1992;20(11):2803-12.
72. Beug ST, Tang VA, LaCasse EC, Cheung HH, Beauregard CE, Brun J, et al. Smac mimetics and innate immune stimuli synergize to promote tumor death. *Nat Biotech*. 2014;32(2):182-90.
73. Najar HM, Dutz JP. Topical TLR9 agonists induce more efficient cross-presentation of injected protein antigen than parenteral TLR9 agonists do. *European journal of immunology*. 2007;37(8):2242-56.
74. Cheng WK, Wee K, Kollmann TR, Dutz JP. Topical CpG Adjuvantation of a Protein-Based Vaccine Induces Protective Immunity to *Listeria monocytogenes*. *Clinical and vaccine immunology : CVI*. 2014;21(3):329-39.

75. Wadas TJ, Wong EH, Weisman GR, Anderson CJ. Coordinating Radiometals of Copper, Gallium, Indium, Yttrium, and Zirconium for PET and SPECT Imaging of Disease. *Chemical reviews*. 2010;110(5):2858-902.
76. Critically Selected Stability Constants of Metal Complexes. In: Technology NIOsA, editor.
77. Xu X, Liu Y, Li Z, Lv Z, Song J, He M, et al. Thermal study of boehmite nanofibers with controlled particle size. *J Therm Anal Calorim*. 2014;115(2):1111-7.
78. Zhu B, Fang B, Li X. Dehydration reactions and kinetic parameters of gibbsite. *Ceramics International*. 2010;36(8):2493-8.
79. Brenntag Biosector. Product Specifications for Alhydrogel 1.3% [cited April 15, 2016]. Available from: [http://www.brenntag.com/media/documents/denmark/specification\\_alhydrogel\\_13\\_bbs\\_ed\\_03.pdf](http://www.brenntag.com/media/documents/denmark/specification_alhydrogel_13_bbs_ed_03.pdf).
80. HogenEsch H. Mechanism of Immunopotentiality and Safety of Aluminum Adjuvants. *Frontiers in Immunology*. 2012;3:406.
81. Newman MJ, Wu JY, Gardner BH, Munroe KJ, Leombruno D, Recchia J, et al. Saponin adjuvant induction of ovalbumin-specific CD8<sup>+</sup> cytotoxic T lymphocyte responses. *J Immunol*. 1992;148(8):2357-62.
82. MacLeod MKL, McKee AS, David A, Wang J, Mason R, Kappler JW, et al. Vaccine adjuvants aluminum and monophosphoryl lipid A provide distinct signals to generate protective cytotoxic memory CD8 T cells. *Proceedings of the National Academy of Sciences of the United States of America*. 2011;108(19):7914-9.
83. Serre K, Mohr E, Gaspal F, Lane PJ, Bird R, Cunningham AF, et al. IL-4 directs both CD4 and CD8 T cells to produce Th2 cytokines in vitro, but only CD4 T cells produce these cytokines in response to alum-precipitated protein in vivo. *Molecular immunology*. 2010;47(10):1914-22.
84. Nordion. Indium-111 Radiochemical Indium Chloride Solution [cited July 12, 2016]. Available from: [http://www.nordion.com/wp-content/uploads/2014/10/MI\\_Indium-111\\_Canada.pdf](http://www.nordion.com/wp-content/uploads/2014/10/MI_Indium-111_Canada.pdf).
85. Cherry SR, Sorenson JA, Phelps ME. *Physics in Nuclear Medicine*: Elsevier Health Sciences; 2012.
86. Rahmim A, Zaidi H. PET versus SPECT: strengths, limitations and challenges. *Nucl Med Commun*. 2008;29(3):193-207.
87. de Kemp RA, Epstein FH, Catana C, Tsui BMW, Ritman EL. Small-Animal Molecular Imaging Methods. *Journal of Nuclear Medicine*. 2010;51(Supplement 1):18S-32S.
88. Kagadis GC, Loudos G, Katsanos K, Langer SG, Nikiforidis GC. In vivo small animal imaging: current status and future prospects. *Medical physics*. 2010;37(12):6421-42.
89. Nordion. Gallium-67 Radiochemical Gallium Chloride Solution [cited July 12, 2016]. Available from: [http://www.nordion.com/wp-content/uploads/2014/10/MI\\_Gallium-67\\_Canada.pdf](http://www.nordion.com/wp-content/uploads/2014/10/MI_Gallium-67_Canada.pdf).
90. Shcherbinin S, Chamoiseau S, Celler A. Quantitative image reconstruction for dual-isotope parathyroid SPECT/CT: phantom experiments and sample patient studies. *Phys Med Biol*. 2012;57(15):4755-69.

91. Cooper MS, Ma MT, Sunassee K, Shaw KP, Williams JD, Paul RL, et al. Comparison of (64)Cu-complexing bifunctional chelators for radioimmunoconjugation: labeling efficiency, specific activity, and in vitro/in vivo stability. *Bioconjugate chemistry*. 2012;23(5):1029-39.
92. Saatchi K, Gelder N, Gershkovich P, Sivak O, Wasan KM, Kainthan RK, et al. Long-circulating non-toxic blood pool imaging agent based on hyperbranched polyglycerols. *International journal of pharmaceutics*. 2012;422(1–2):418-27.
93. Vis R, Lavalaye J, van de Garde EMW. GMP-compliant (68)Ga radiolabelling in a conventional small-scale radiopharmacy: a feasible approach for routine clinical use. *EJNMMI research*. 2015;5:27.
94. Arndt C, Koristka S, Bartsch H, Bachmann M. Native Polyacrylamide Gels. In: Kurien TB, Scofield HR, editors. *Protein Electrophoresis: Methods and Protocols*. Totowa, NJ: Humana Press; 2012. p. 49-53.
95. Blancher C, Jones A. SDS -PAGE and Western Blotting Techniques. In: Brooks SA, Schumacher U, editors. *Metastasis Research Protocols: Volume I: Analysis of Cells and Tissues*. Totowa, NJ: Humana Press; 2001. p. 145-62.
96. Lawrence A-M, Besir H. Staining of Proteins in Gels with Coomassie G-250 without Organic Solvent and Acetic Acid. *Journal of visualized experiments : JoVE*. 2009(30):1350.
97. Goorden MC, van der Have F, Kreuger R, Ramakers RM, Vastenhouw B, Burbach JPH, et al. VECTor: A Preclinical Imaging System for Simultaneous Submillimeter SPECT and PET. *Journal of Nuclear Medicine*. 2013;54(2):306-12.
98. Ivashchenko O, van der Have F, Goorden MC, Ramakers RM, Beekman FJ. Ultra-High-Sensitivity Submillimeter Mouse SPECT. *Journal of Nuclear Medicine*. 2015;56(3):470-5.
99. Branderhorst W, Vastenhouw B, Beekman FJ. Pixel-based subsets for rapid multi-pinhole SPECT reconstruction. *Phys Med Biol*. 2010;55(7):2023-34.
100. Ogawa K, Harata Y, Ichihara T, Kubo A, Hashimoto S. A practical method for position-dependent Compton-scatter correction in single photon emission CT. *IEEE transactions on medical imaging*. 1991;10(3):408-12.
101. Loening AM, Gambhir SS. AMIDE: a free software tool for multimodality medical image analysis. *Molecular imaging*. 2003;2(3):131-7.
102. Tai T, Yamashita K, Ito S, Kobata A. Structures of the carbohydrate moiety of ovalbumin glycopeptide III and the difference in specificity of endo-beta-N-acetylglucosaminidases CII and H. *The Journal of biological chemistry*. 1977;252(19):6687-94.
103. Chang M, Shi Y, Nail SL, HogenEsch H, Adams SB, White JL, et al. Degree of antigen adsorption in the vaccine or interstitial fluid and its effect on the antibody response in rabbits. *Vaccine*. 2001;19(20-22):2884-9.
104. Petros RA, DeSimone JM. Strategies in the design of nanoparticles for therapeutic applications. *Nat Rev Drug Discov*. 2010;9(8):615-27.

105. Nakai T, Okuyama C, Kubota T, Kobayashi K, Tsubokura T, Ushijima Y, et al. Pattern of <sup>111</sup>In-chloride bone marrow scintigraphy in myelodysplastic syndrome; comparison with clinical characteristics. *Ann Nucl Med.* 2004;18(8):675-80.
106. Bendall SC, Nolan GP, Roederer M, Chattopadhyay PK. A deep profiler's guide to cytometry. *Trends in immunology.* 2012;33(7):323-32.
107. Fluidigm. Mass Cytometry Publications 2016 [cited July 2, 2016]. Available from: <https://www.fluidigm.com/binaries/content/documents/fluidigm/marketing/mass-cytometry-selected-publications/mass-cytometry-selected-publications/fluidigm%3Afile>.
108. Fernandez R, Maecker H. Cytokine-Stimulated Phosphoflow of Whole Blood Using CyTOF Mass Cytometry. *Bio-protocol.* 2015;5(11):e1495.
109. Fienberg HG, Simonds EF, Fantl WJ, Nolan GP, Bodenmiller B. A platinum-based covalent viability reagent for single-cell mass cytometry. *Cytometry Part A : the journal of the International Society for Analytical Cytology.* 2012;81(6):467-75.
110. Ornatsky OI, Lou X, Nitz M, Sheldrick WS, Baranov VI, Bandura DR, et al. Study of Cell Antigens and Intracellular DNA by Identification of Element-Containing Labels and Metallointercalators Using Inductively Coupled Plasma Mass Spectrometry. *Analytical Chemistry.* 2008;80(7):2539-47.
111. Finck R, Simonds EF, Jager A, Krishnaswamy S, Sachs K, Fantl W, et al. Normalization of mass cytometry data with bead standards. *Cytometry Part A.* 2013;83A(5):483-94.
112. Suzuki H, Toyooka T, Ibuki Y. Simple and Easy Method to Evaluate Uptake Potential of Nanoparticles in Mammalian Cells Using a Flow Cytometric Light Scatter Analysis. *Environmental Science & Technology.* 2007;41(8):3018-24.
113. Hultkvist U, Westergren G, Hansson UB, Lewan L. Effects of pH on the stability of the indium-113m blood protein complex and the selective binding of indium-113m to transferrin. *Research in experimental medicine Zeitschrift fur die gesamte experimentelle Medizin einschliesslich experimenteller Chirurgie.* 1987;187(2):131-7.
114. Zhang X, Goncalves R, Mosser DM. The Isolation and Characterization of Murine Macrophages. *Current protocols in immunology / edited by John E Coligan [et al].* 2008;CHAPTER:Unit-14.1.
115. Gabilovich DI, Ostrand-Rosenberg S, Bronte V. Coordinated regulation of myeloid cells by tumours. *Nature reviews Immunology.* 2012;12(4):253-68.
116. Lin W. A High-Sensitivity Lanthanide Nanoparticle Reporter. 2014;30(11):3142-53.
117. Itano AA, McSorley SJ, Reinhardt RL, Ehst BD, Ingulli E, Rudensky AY, et al. Distinct dendritic cell populations sequentially present antigen to CD4 T cells and stimulate different aspects of cell-mediated immunity. *Immunity.* 2003;19(1):47-57.
118. Pape KA, Catron DM, Itano AA, Jenkins MK. The humoral immune response is initiated in lymph nodes by B cells that acquire soluble antigen directly in the follicles. *Immunity.* 2007;26(4):491-502.

119. Sixt M, Kanazawa N, Selg M, Samson T, Roos G, Reinhardt DP, et al. The conduit system transports soluble antigens from the afferent lymph to resident dendritic cells in the T cell area of the lymph node. *Immunity*. 2005;22(1):19-29.
120. van Vugt E, Kamperdijk EW, Beelen RH. Migration patterns of rat peritoneal macrophages and dendritic cells. *Transplantation proceedings*. 1993;25(5):2808-10.
121. Xu DZ, Zhao K, Guo LM, Li LJ, Xie Q, Ren H, et al. A randomized controlled phase IIb trial of antigen-antibody immunogenic complex therapeutic vaccine in chronic hepatitis B patients. *PloS one*. 2008;3(7):e2565.
122. Wang XY, Yao X, Wan YM, Wang B, Xu JQ, Wen YM. Responses to multiple injections with alum alone compared to injections with alum adsorbed to proteins in mice. *Immunol Lett*. 2013;149(1-2):88-92.
123. Graham L, Orenstein JM. Processing tissue and cells for transmission electron microscopy in diagnostic pathology and research. *Nat Protocols*. 2007;2(10):2439-50.
124. Bozzola JJ. Conventional specimen preparation techniques for transmission electron microscopy of cultured cells. *Methods in molecular biology*. 2007;369:1-18.
125. Giberson RT, Austin RL, Charlesworth J, Adamson G, Herrera GA. Microwave and digital imaging technology reduce turnaround times for diagnostic electron microscopy. *Ultrastructural pathology*. 2003;27(3):187-96.
126. Soplop NH, Patel R, Kramer SG. Preparation of embryos for Electron Microscopy of the Drosophila embryonic heart tube. 2009(34):e1630.
127. Munks MW, McKee AS, Macleod MK, Powell RL, Degen JL, Reisdorph NA, et al. Aluminum adjuvants elicit fibrin-dependent extracellular traps in vivo. *Blood*. 2010;116(24):5191-9.
128. Ozden MG, Kefeli M, Aydin F, Senturk N, Canturk T, Turanli AY. Persistent subcutaneous nodules after immunotherapy injections for allergic asthma. *J Cutan Pathol*. 2009;36(7):812-4.
129. Exley C. Aluminium adjuvants and adverse events in sub-cutaneous allergy immunotherapy. *Allergy, Asthma, and Clinical Immunology : Official Journal of the Canadian Society of Allergy and Clinical Immunology*. 2014;10(1):4.
130. Tomljenovic L, Shaw CA. Aluminum vaccine adjuvants: are they safe? *Current medicinal chemistry*. 2011;18(17):2630-7.
131. Mayhew TM, Mühlfeld C, Vanhecke D, Ochs M. A review of recent methods for efficiently quantifying immunogold and other nanoparticles using TEM sections through cells, tissues and organs. *Annals of Anatomy - Anatomischer Anzeiger*. 2009;191(2):153-70.
132. Sun B, Ji Z, Liao Y-P, Wang M, Wang X, Dong J, et al. Engineering an Effective Immune Adjuvant by Designed Control of Shape and Crystallinity of Aluminum Oxyhydroxide Nanoparticles. *ACS nano*. 2013;7(12):10834-49.

133. Wang X, Li X, Sogo Y, Ito A. Simple synthesis route of mesoporous AlOOH nanofibers to enhance immune responses. *Rsc Adv.* 2013;3(22):8164-7.
134. Li X, Aldayel AM, Cui Z. Aluminum hydroxide nanoparticles show a stronger vaccine adjuvant activity than traditional aluminum hydroxide microparticles. *Journal of controlled release : official journal of the Controlled Release Society.* 2014;173:148-57.
135. Li H, Li Y, Jiao J, Hu HM. Alpha-alumina nanoparticles induce efficient autophagy-dependent cross-presentation and potent antitumour response. *Nat Nanotechnol.* 2011;6(10):645-50.
136. Lipton ML. Image Contrast: T1, T2, T2\*, and Proton Density. *Totally Accessible MRI: A User's Guide to Principles, Technology, and Applications.* New York, NY: Springer New York; 2008. p. 38-46.
137. Lee B-I, Lee KS, Lee JH, Lee IS, Byeon S-H. Synthesis of colloidal aqueous suspensions of a layered gadolinium hydroxide: a potential MRI contrast agent. *Dalton Transactions.* 2009(14):2490-5.
138. Sanchez P, Valero E, Galvez N, Dominguez-Vera JM, Marinone M, Poletti G, et al. MRI relaxation properties of water-soluble apoferritin-encapsulated gadolinium oxide-hydroxide nanoparticles. *Dalton transactions (Cambridge, England : 2003).* 2009(5):800-4.
139. Bridot J-L, Faure A-C, Laurent S, Rivière C, Billotey C, Hiba B, et al. Hybrid Gadolinium Oxide Nanoparticles: Multimodal Contrast Agents for in Vivo Imaging. *Journal of the American Chemical Society.* 2007;129(16):5076-84.

## Appendix 1: Development of a MR-Traceable Form of AlO(OH)

One of the limitations with  $^{111}\text{In}$ -AlO(OH) is that the adjuvant can only be tracked for 15 days before the radioactive dopant has decayed to too great of an extent to obtain accurate results (84). Given the data presented in this thesis, it would be valuable to have an AlO(OH) adjuvant that could be reliably traced for a much longer period of time. One option would be to dope the crystal structure with a longer lived radioisotope, like  $^{51}\text{Cr}$  (27.8 day half life), which allows the adjuvant to be quantitatively tracked for  $\sim 140$  days. However, most labs do not have access to high-level radiation facilities and nuclear imaging equipment to use such tracers. A non-radioactive adjuvant that can be tracked for a long period of time might be useful to other groups that wish to examine the biodistribution of aluminum-based adjuvants.

Gadolinium (Gd) is a paramagnetic element that shortens both longitudinal ( $T_1$ ) and transverse ( $T_2$ ) relaxation times in magnetic resonance (MR) imaging (136). Given recent articles about Gd-doped nanoparticles and layered double hydroxides as contrast agents, experiments were undertaken to explore the potential of Gd-AlO(OH) as a MR-traceable form of Alhydrogel (137-139).

$\text{GdCl}_3 \cdot 6\text{H}_2\text{O}$  was co-precipitated with  $\text{AlCl}_3 \cdot 6\text{H}_2\text{O}$  as described in chapter 2 of this thesis. PXRD and FTIR data show that Gd-AlO(OH) closely matches commercial Alhydrogel (Figure A-1). The crystal structure appears to become more amorphous as the [Gd] is increased.

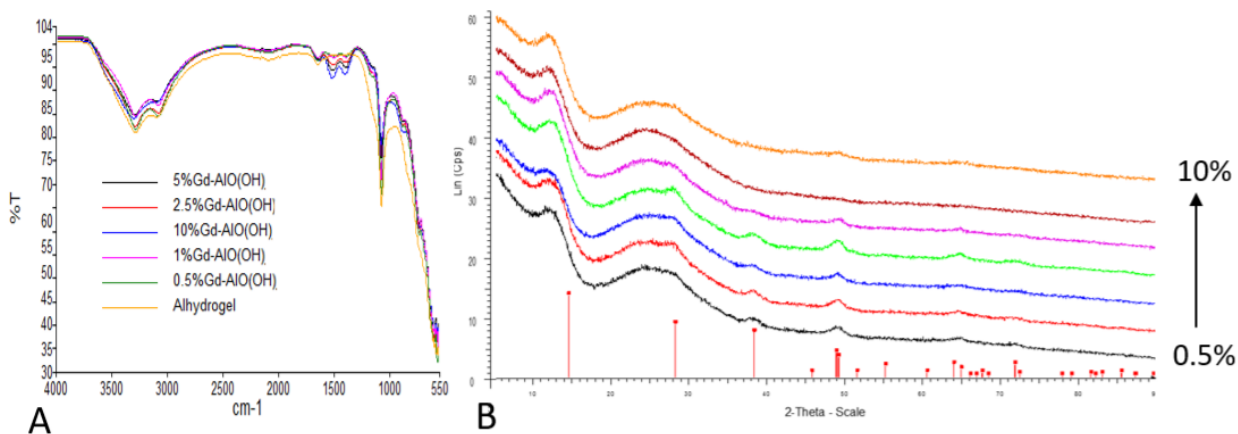


Figure A- 1: FTIR (A) and PXRD (B) of 0.5-10% Gd-AlO(OH).

In order to evaluate the effectiveness of Gd-AIO(OH) as a MR contrast agent, the relaxation properties of the adjuvant were examined using a Biospec 7.0 T pre-clinical scanner (Bruker). Figure A-2 shows that 0.45 %w/v solution of 0.5-2.5% Gd-AIO(OH) (equivalent 380, 760 and 1900 $\mu$ M Gd) provided MR contrast. The relativity values for the MR responsive adjuvants are listed in Table A-1. . Gd-AIO(OH) maybe useful to assess the amount of adjuvant remaining at the site of injection over a longer timeframe that was achievable with <sup>111</sup>In-AIO(OH).

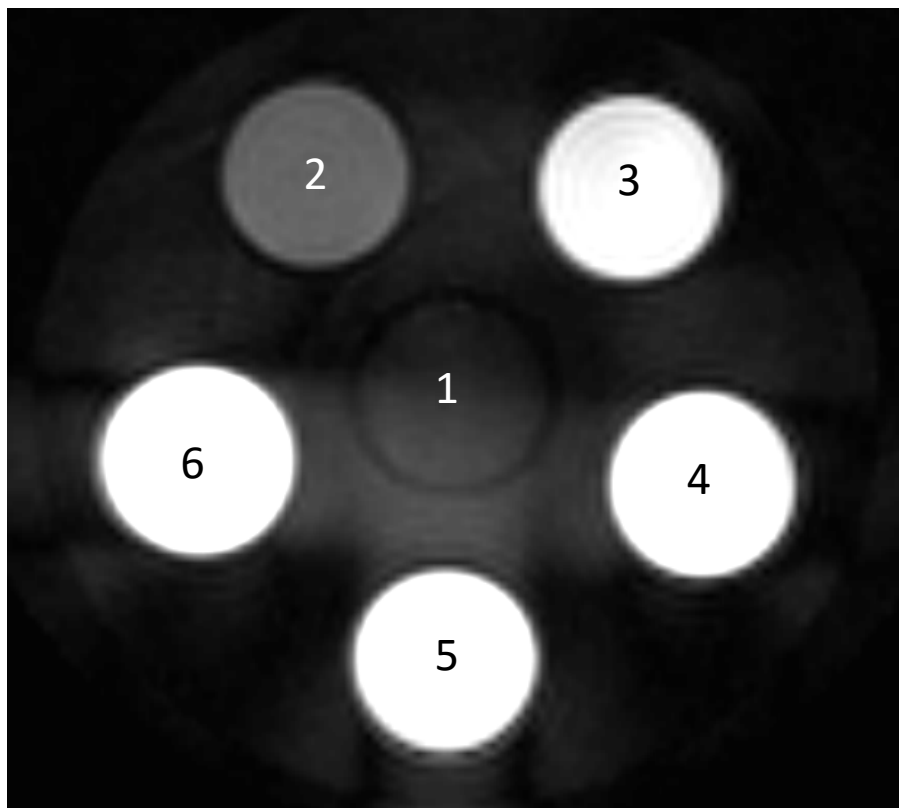


Figure A- 2: MR phantom scan of Alhydrogel (1), 1000 $\mu$ M Gadovist (2), 0.5% Gd-DTPA (Gadovist; 2), 0.5% Gd-AIO(OH) (3), 1% Gd-AIO(OH) (4-5) and 2.5% Gd-AIO(OH) (6).

Adjuvant ([Gd])	T1	T2*	R1	R2*
0.5% Gd-AIO(OH) (380 $\mu$ M)	127.49	8.08	0.0078	0.12
1% Gd-AIO(OH) (760 $\mu$ M)	62.91	2.05	0.015	0.48
2.5% Gd-AIO(OH) (1900 $\mu$ M)	49.89	0.78	0.020	1.3

Table A- 1: Relaxivity values for Gd-AIO(OH) in a 7T MRI.

Figure A-3 shows a phantom scan of 1% Gd-AlO(OH) serially diluted by a factor of 10 from 0.45 w/v% (760 $\mu$ M Gd). No appreciable contrast was observed after a 1/100 dilution of the adjuvant. Gd-AlO(OH) may not be a sensitive enough tracer to assess the distribution of Alhydrogel to sites beyond the injection site.

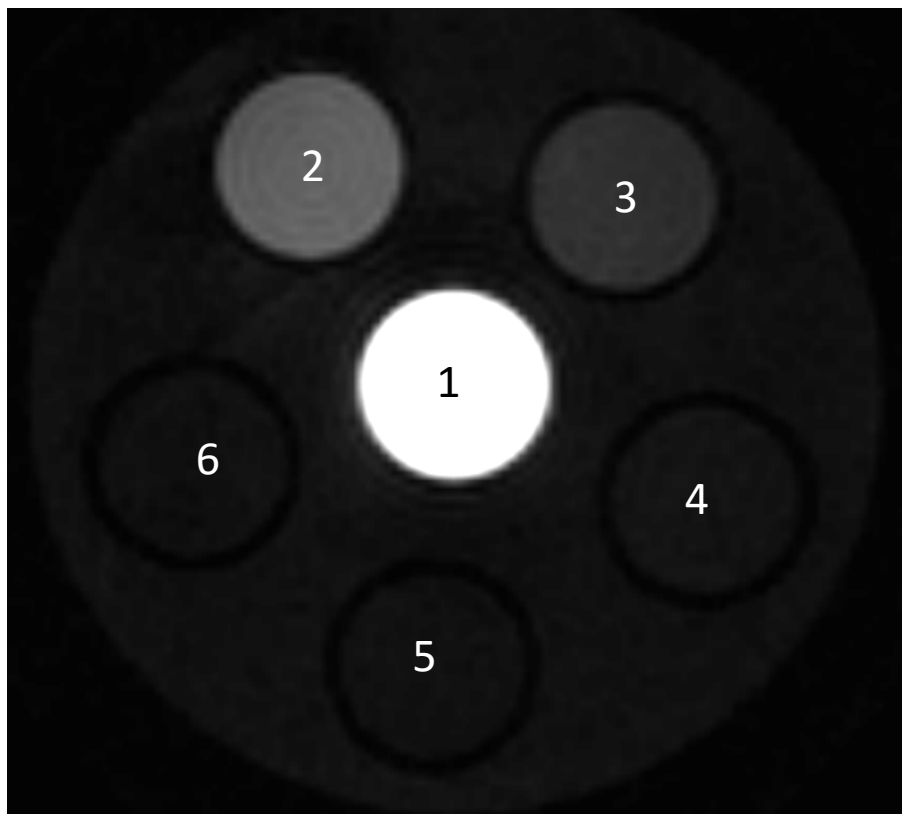


Figure A- 3: MR phantom of 1% Gd-AlO(OH) adjuvant at 0.45% w/v (760 $\mu$ M Gd) (1). The adjuvant was diluted 1/10 serially (3-6). 1000 $\mu$ M Gadovist control (2).